LLE Review

Quarterly Report

UR ✷
LLE ✷

About the Cover:

In OMEGA's target bay, engineers Wade Bittle (left) and Byra Ferkovich (right) perform operational tests on the OMEGA Multichannel Streak Camera. The LLE-designed camera provides an accurate method of simultaneously analyzing the timing and temporal pulse shape of multiple OMEGA beams. The camera is shown in its mounting configuration on an F-ASP ("F" alignment sensor package) structure, where it samples the beams. A key feature of the electronics within the camera is the modular design. The keypad and display of the microprocessor-based controller module are visible in the foreground. A sweep deflection module is located on the bench in front of Mr. Ferkovich.

For questions or comments, contact Stephen D. Jacobs, *Editor*, Laboratory for Laser Energetics, 250 East River Road, Rochester, NY 14623-1299, (716) 275-4837.

Worldwide-Web Home Page: http://www.lle.rochester.edu/

LLE Review

Quarterly Report

UR ※
LLE

Contents

In Brief

This volume of the LLE Review, covering the period October–December 1997, includes an article on a new electrical waveform generator based on aperture-coupled striplines. As described by Mark Skeldon, the waveform generator is capable of producing shaped electrical waveforms with 50- to 100-ps structure over a 1- to 5-ns envelope at voltage levels suitable for OMEGA pulse-shaping applications. The design is a significant simplification over existing technology and offers many performance enhancements. Other highlights of research presented in this issue are

- Development of the sweep deflection circuitry for the OMEGA multichannel streak camera, aided by a computer simulation model, is presented by Wade Biddle and David Lonobile. Good agreement between the model predictions and measurements shows that using the model is an efficient means for conducting initial design, performance optimization, and correction of performance deficiencies.

- A nuclear diagnostic for measuring the areal density of ICF targets is discussed by Radha Bahukutumbi and Stan Skupsky. This diagnostic is obtained by the addition of ^{3}He to the fuel and is based on the energy loss of the 14.7-MeV D-^{3}He proton in the target. This diagnostic will extend LLE's ability to measure areal density to the high-density regime expected for cryogenic DD targets on OMEGA.

- Riccardo Betti *et al*. describe a simple procedure to determine the Froude number *Fr*, the effective power index for thermal conduction ν, and the ablation front thickness L_0 of laser-accelerated ablation fronts. These parameters are determined by fitting the density and pressure profiles obtained from one-dimensional numerical simulations with the analytic isobaric profiles. These quantities are then used to calculate the growth rate of the ablative Rayleigh–Taylor instability using the theory developed by V. N. Goncharov *et al*., Phys. Plasmas **3**, 4665 (1996).

- The indirect-drive approach to inertial confinement fusion involves laser beams that overlap as they enter the hohlraum. Because a power transfer between the beams adversely affects the implosion symmetry, it is important to understand the mechanisms that make such a power transfer possible. In a previous article [LLE Review **66**, 73 (1996)] Colin McKinstrie described a two-dimensional analysis of the power transfer between beams with top-hat intensity profiles in a homogeneous plasma. In this article, the power transfer between crossed laser beams made possible by an ion-acoustic wave is extended to include three dimensions and arbitrary intensity profiles.

- In an effort to identify an inexpensive shielding material to protect valuable laser optics from various forms of debris, Semyon Papernov screened perfluorinated polymer pellicles from various vendors. The optical-performance results of these tests (reported here) yielded the highest 351-nm-laser-damage thresholds ever recorded at LLE for 0.6-ns pulses.

- Subsurface damage induced by microgrinding of glass is an important feature of the resulting surface that must be removed in any subsequent finishing operation. John Lambropoulos *et al*. show how the depth of subsurface damage can be estimated from the measured surface roughness, how it can be correlated to the near-surface mechanical properties of the glass, and how ground-surface quality depends on the type of grinding process employed.

- Polishing abrasives that have been bound in a solid matrix can offer several potential advantages over loose-abrasive processes for finishing of optics. Birgit Gillman establishes the various criteria for a successful bound-abrasive polisher and reports results for six compositions used on a CNC generating machine to polish optical glass.

- Despite angle dependence and polarization selectivity, the color of cholesteric liquid crystal (CLC) polysiloxane films can be quantified by standard colorimetry. A new fractured form of the film called "flakes" makes it possible to use the Center of Gravity Color Mixing Principle to predict the chromaticity of CLC color mixtures. Eileen Korenic *et al*. show how a complete color gamut can be produced by layering CLC films, mixing CLC's physico-chemically, and mixing CLC flakes.

Stephen D. Jacobs
Editor

A High-Bandwidth Electrical-Waveform Generator Based on Aperture-Coupled Striplines for OMEGA Pulse-Shaping Applications

Pulsed-laser systems emit optical pulses having a temporal pulse shape characteristic of the particular type of laser design. Advances in technology have produced laser-pulse-shaping systems where the laser temporal profile can be specified in advance and controlled to a high degree of accuracy.[1–3] A pulse-shaping system has been in operation on OMEGA for several years. Temporally shaped optical pulses can be produced by applying shaped electrical waveforms to a dual-channel integrated-optics modulator.[1–3] These shaped electrical waveforms are sent to the optical modulator synchronized with the passage through the modulator of an optical pulse from a single-longitudinal-mode (SLM) laser.[4] The optical pulse exiting the modulator is then shaped in accordance with the voltage-dependent transfer function of the modulator. Hence, the electrical-waveform generator is an important component in any optical-pulse-shaping system incorporating optical modulators. This article discusses a greatly simplified pulse-shaping system based on an aperture-coupled-stripline (ACSL) electrical-waveform generator under development for OMEGA, and compares its many advantages over the existing OMEGA pulse-shaping system.

The Present OMEGA Pulse-Shaping System

The OMEGA pulse-shaping system uses an electrical-waveform generator based on an electrical reflection from a variable-impedance microstrip line (VIMSL).[3] Electrical-waveform generators based on stripline technology offer the highest temporal resolution over other systems due to their high-bandwidth capabilities, stripline-fabrication procedures, and achievable tolerances. The present OMEGA pulse-shaping system (outlined in Fig. 73.1) consists of many components. A cw mode-locked (CWML) laser is used to seed a regenerative amplifier (regen). The temporal width of the optical pulse injected into this regen is stretched in time with an intracavity etalon.[5] The output of the regenerative amplifier is amplified, and its leading edge is steepened with a stimulated Brillouin scattering (SBS) reflection from CCL_4.[6] This SBS pulse is amplified and sent to a fiber distribution system to illuminate photoconductive (PC) switches. Illumination of the PC switches activates the electrical-waveform generator, which produces the temporally shaped electrical waveforms that are sent to the optical modulator.[3,7] The subsequently shaped optical pulse from the modulator is sent to the OMEGA
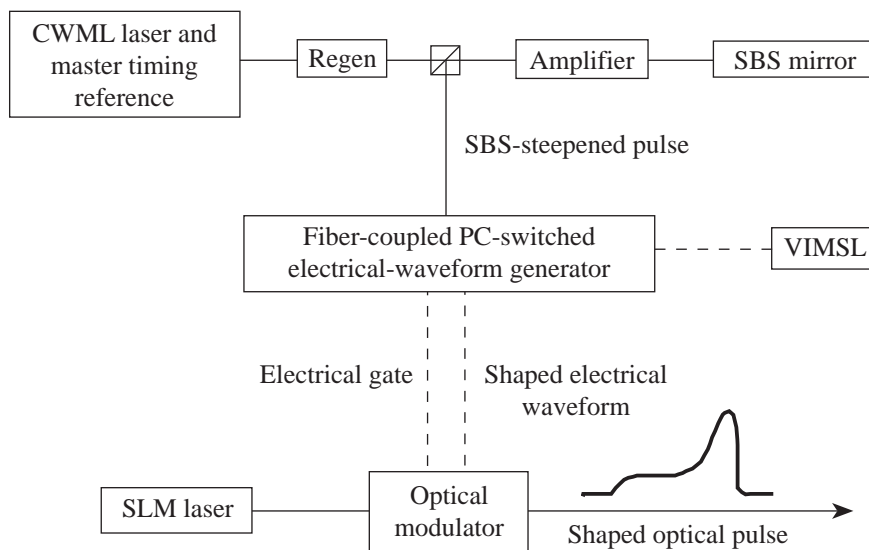

E8890

amplifiers with timing referenced with respect to the activation of the PC switches by the SBS pulse.

The VIMSL in OMEGA's electrical-waveform generator is a two-port electrical device.[3,7] A square electrical pulse is sent into one port of the device and propagates to the second terminated port. A shaped electrical waveform, generated by reflections along the length of the VIMSL, exits from the VIMSL through the input port and is sent to the optical modulator. This electrical-waveform generator has some anomalies that must be mitigated to achieve a high contrast (i.e., the ratio of the maximum pulse amplitude to the prepulse noise). The square electrical waveform sent to the VIMSL has a voltage stair step that is attributable to the finite "off" impedance and nonzero "on" impedance of the PC switches. The effects of this dc step are substantially minimized by applying a temporal delay to the shaped electrical waveform. In addition, there is a capacitively coupled voltage spike on the voltage waveform applied to the modulator that is attributable to the capacitance of the PC switch in the off state. To eliminate this prepulse and improve the contrast of the shaped optical pulses, a square electrical gate pulse is applied to the second channel of the modulator.

The ACSL Pulse-Shaping System

A pulse-shaping system with an electrical-waveform generator based on an ACSL has been developed. A layout of this ACSL pulse-shaping system is shown in Fig. 73.2. A square electrical waveform from a commercially available pulse generator is sent to an ACSL. The ACSL generates a shaped electrical waveform that is sent directly to the optical modulator for pulse shaping.

The design of the electrical-waveform generator is based on a four-layer, four-port ACSL and is modeled as a four-port electrical directional coupler. An exploded view of a practical device with four layers of material having dielectric constant ε_r is shown in Fig. 73.3. The important region of the ACSL for pulse shaping is the coupling region shown in cross section in Fig. 73.4. In operation, a square electrical waveform is launched into port 1 and propagates along electrode 1 to the terminated port 2 of the ACSL. As the square electrical waveform propagates along electrode 1 in the coupling region, the electrical signal is coupled through an aperture to electrode 2 in the backward direction and exits at port 4. By properly varying the width of the coupling aperture (*s* in Fig. 73.4) along the length of the ACSL, any desired temporally shaped electrical waveform can be generated at port 4 and sent to optical modulators for pulse shaping.

The ACSL system is characterized by an input and output impedance. The characteristic impedance Z_0 of the system is chosen to be 50 Ω to match the input impedance of the modulator channels. Ports 2 and 3 of the ACSL are terminated with this characteristic impedance to prevent reflections at these ports. The transition section of the ACSL is designed to accommodate the electrical connectors (stripline end launchers) required to transmit electrical signals from the standard coaxial electrical cables used as input and output to the ACSL to the coupling region of the ACSL (illustrated by the cross-sectional geometry in Fig 73.4). In the transition region (and in the coupling region when the aperture width is zero), the system can be thought of as two separate uncoupled and noninteracting ordinary striplines. To achieve a 50-Ω stripline in this section, the width of the electrode *w* is determined from well-known relations[8] involving the material parameters and the geometry of the ACSL.

To design and produce shaped voltage waveforms at port 4 of an ACSL, the electrical coupling coefficient from electrode 1 to electrode 2 (i.e., the ratio of the output-pulse voltage at port 4 to the input-pulse voltage at port 1) as a function of
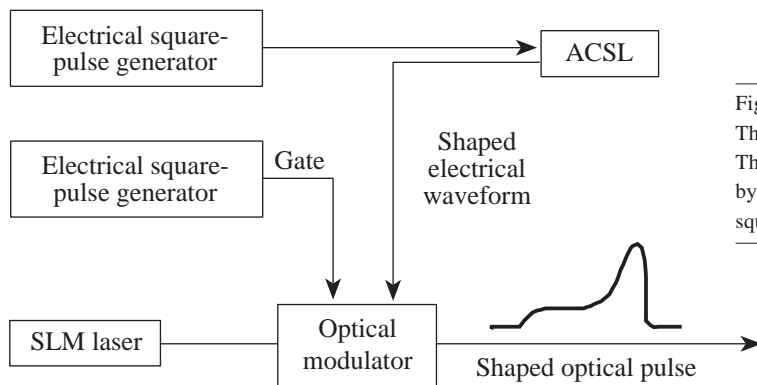

Figure 73.2
The aperture-coupled-stripline (ACSL) optical-pulse-shaping system. The output from an electrical square-pulse generator is temporally shaped by an ACSL and used to drive an optical modulator. A separate electrical square-pulse generator is used to gate the second channel of the modulator.

E8891

E8416
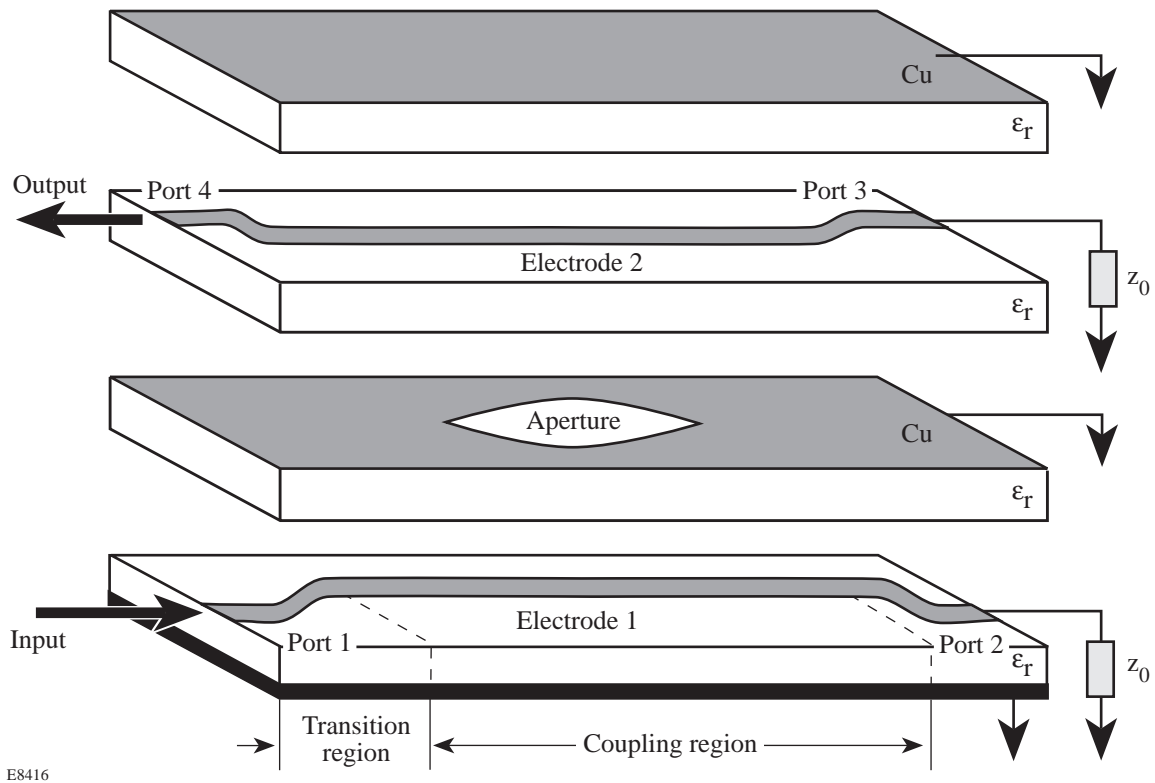
Figure 73.3
Exploded view of a practical four-layer, four-port ACSL. A square electrical waveform is launched into port 1 and propagates along electrode 1 to the terminated port 2. The electrical signal is coupled through an aperture to electrode 2 in the backward direction and a shaped electrical waveform exits at port 4.

aperture width *s* must be known. It is difficult to calculate this explicitly; however, simple experiments have been performed to measure this dependence. The data from these measurements are used in our model for designing ACSL devices.

E8892
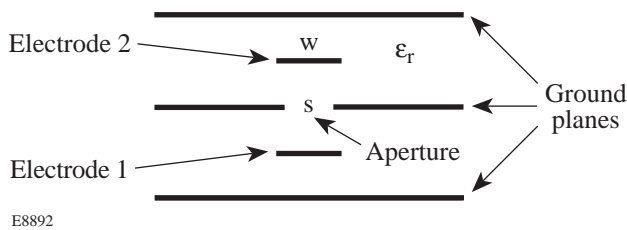
Figure 73.4
Cross-sectional view of an ACSL in the coupling region of Fig. 73.3. The electrode width *w* is chosen to provide a 50-Ω impedance structure. The amount of electrical coupling from electrode 1 to electrode 2 depends on the aperture width *s*.

Several ACSL devices have been fabricated and tested to determine the dependence of the electrical coupling coefficient on the aperture width *s*. A typical structure consists of four layers of RT/duroid[®9] 5880 microwave laminate material ($\varepsilon_r = 2.2$) sandwiched together as illustrated in Fig. 73.3. The two outer layers are 0.125 in. thick with 1 oz/ft^2 of copper on their outer surfaces. The stripline electrode width (*w* in Fig. 73.4) on the opposite side of these layers is 0.075 in. (experimentally verified to provide a 50-Ω impedance) and is machined with a precision programmable milling machine. (Note that electrode 2 in Fig. 73.3 is shown on an intermediate layer. This is for illustration purposes only. This electrode in our device is machined on the bottom of the layer above it, making the two outer layers completely identical.) The two center layers are 0.031 in. thick. One center layer has no copper on either surface and is used as a dielectric spacer. The other center layer has 1 oz/ft^2 of copper on one side only, with copper removed to form the appropriate coupling aperture. The

structure is easily disassembled to replace the aperture layer to produce different shaped electrical waveforms. Several other ACSL geometries with different layer thickness and electrode widths were tested, but as will be shown below, the above geometry produces a sufficiently high electrical coupling co-efficient for our pulse-shaping application.

Three apertures having a width *s* that varies along the length of the line with the functional form of a simple Gaussian are used in the above structure to determine the dependence of the electrical coupling coefficient on the aperture width *s*. The maximum aperture widths of the three Gaussians are 5, 10, and 20 mm. Voltage measurements are made with a high-band-width (20-GHz)[10] sampling oscilloscope equipped with an electrical square-pulse generator for time domain reflectome-ter (TDR) measurements. The pulse from the TDR channel is sent into port 1 of the ACSL, and the output from port 4 is measured with a separate, high-bandwidth (20-GHz) channel of the oscilloscope. The time axis of the measured voltage waveforms is mapped to position along the ACSL using the electrical propagation velocity in the RT/duroid® material. From our measurements on the three Gaussian apertures, the electrical coupling coefficient versus aperture width is ob-tained and shown in Fig. 73.5. The data in Fig. 73.5 are used in our model to design ACSL devices that produce specific voltage waveforms for the optical-pulse-shaping system.
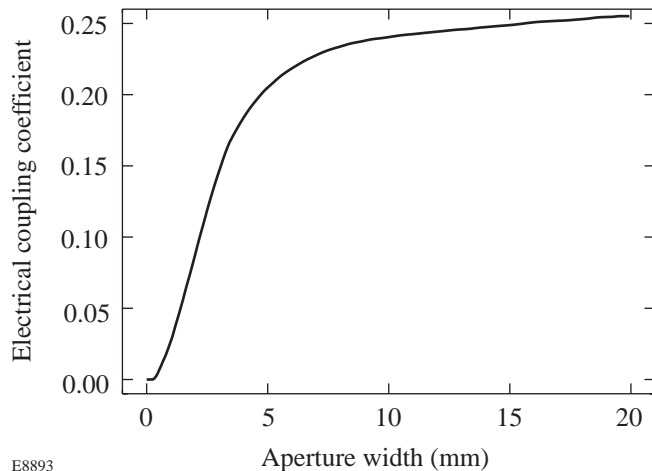
E8893

Figure 73.5
The electrical coupling coefficient, defined as the ratio of the output voltage at port 4 to the input voltage at port 1 in Fig. 73.3, plotted as a function of aperture width for an ACSL with the geometry discussed in the text.

The output voltage measured at port 4 of an ACSL with 5-mm-Gaussian aperture is plotted with a solid line in Fig. 73.6 (normalized to the voltage of the input square pulse

applied to port 1) along with the prediction of our model plotted with a dashed line. For high coupling coefficients, depletion of the input square-pulse voltage as it propagates along electrode 1 cannot be neglected and is included in our model.
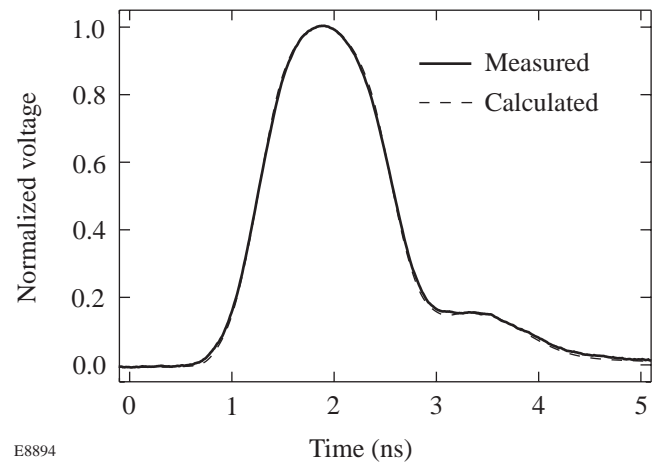
E8894

Figure 73.6
The measured output voltage waveform (solid line) from an ACSL having a Gaussian aperture along the length of the coupling region with a 5-mm maximum aperture width. The calculated output voltage from this structure (dashed line) is also shown.

Temporally shaped optical pulses have been produced using the pulse-shaping system shown in Fig. 73.2 with the ACSL geometry described above. A commercially available square-pulse generator[11] that provides a 35-V square pulse with 100-ps rise time is used as input to the ACSL. The half-wave voltage of the optical modulators used for pulse shaping is approximately 8 V. Hence, the coupling coefficients of 0.25 (shown in Fig. 73.5) obtainable with the ACSL structure described above are adequate for this application. To verify our ACSL model, the output voltage at port 4 of an ACSL designed to produce a specific optical pulse shape is sent to an optical modulator. The measured shaped optical pulse from the modu-lator is plotted with a solid line in Fig. 73.7; the optical pulse shape that is desired from this system is plotted with a dashed line. This figure illustrates the excellent performance and predictability of the ACSL pulse-shaping system.

Pulse-Shaping-Systems Comparison
By comparing the pulse-shaping systems shown in Figs. 73.1 and 73.2, it can be seen that the ACSL system eliminates the need for the CWML laser, the regen with SBS pulse steepener and amplifier, the fiber distribution system, and the PC switches. The key operational advantage of the ACSL pulse-shaping system that allows this simplification is
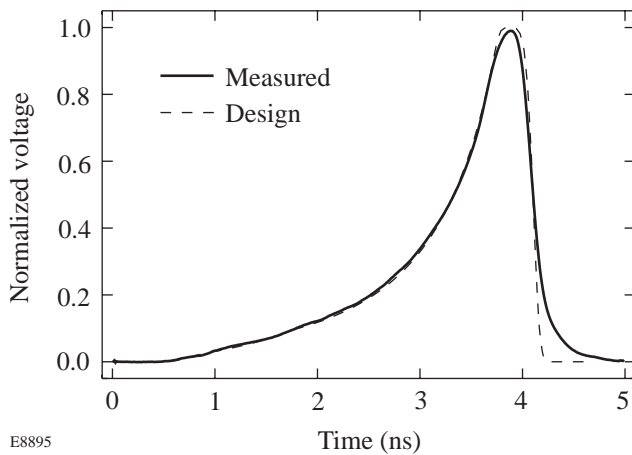
Figure 73.7
The measured temporally shaped optical pulse from an ACSL pulse-shaping system (solid line). The desired optical pulse shape (dashed line) from this system is also shown.

that the shaped electrical waveform from the ACSL exits from a different port than that used to input the square electrical pulse. Consequently, any suitable electrical square-pulse generator can be used to generate shaped electrical waveforms. In addition to this enormous simplification, there is no source of prepulse noise (capacitive voltage spike or dc offset voltage) since coupling cannot occur before application of the square electrical pulse to the ACSL. The system can also be accurately timed to the OMEGA master timing reference (38-MHz rf or 76-MHz CWML-laser optical pulses). The rms timing jitter between the 76-MHz CWML-laser optical pulses and the generation of the shaped electrical waveforms is measured to be less than 10 ps.

Conclusions

An optical-pulse-shaping system based on an ACSL has been designed and tested. This system produces temporally shaped optical pulses with high bandwidth suitable for OMEGA pulse-shaping applications. The design is a significant simplification over existing technology with improved performance capabilities.

REFERENCES

1. R. B. Wilcox, U.S. Patent No. 4,667,161 (19 May 1987).

2. R. B. Wilcox *et al.*, in *Laser Coherence Control: Technology and Applications*, edited by H. T. Powell and T. J. Kessler (SPIE, Bellingham, WA, 1993), Vol. 1870, pp. 53–63.

3. A. Okishev, M. D. Skeldon, S. A. Letzring, W. R. Donaldson, A. Babushkin, and W. Seka, in *Superintense Laser Fields*, edited by A. A. Andreev and V. M. Gordienko (SPIE, Bellingham, WA, 1996), Vol. 2770, pp. 10–17.

4. A. V. Okishev and W. Seka, IEEE J. Sel. Top. Quantum Electron. **3**, 59 (1997).

5. M. D. Skeldon and S. T. Bui, J. Opt. Soc. Am. B **10**, 677 (1993).

6. M. D. Skeldon, A. Okishev, A. Babushkin, and W. Seka, in *First Annual International Conference on Solid State Lasers for Application to Inertial Confinement Fusion*, edited by M. André and H. T. Powell (SPIE, Bellingham, WA, 1995), Vol. 2633, pp. 422–429.

7. M. D. Skeldon, A. Okishev, S. A. Letzring, W. R. Donaldson, K. Green, W. Seka, and L. Fuller, in *Optically Activated Switching IV*, edited by W. R. Donaldson (SPIE, Bellingham, WA, 1994), Vol. 2343, pp. 94–98.

8. B. C. Wadell, *Transmission Line Design Handbook* (Artech House, Boston, 1991).

9. RT/duroid®, Rogers Corporation, Microwave Division, Chandler, AZ 85226.

10. 20-GHz sampling oscilloscope, Model No. HP54120B/54124A, Hewlett Packard, Santa Clara, CA 95052-8059.

11. Pulse generator, Model No. 4500E, Picosecond Pulse Labs, Boulder, CO 80306.

Sweep Deflection Circuit Development Using Computer-Aided Circuit Design for the OMEGA Multichannel Streak Camera

A streak camera is an electro-optic instrument capable of resolving high-speed, low-repetition-rate, pulsed laser phenomena. The basis of the instrument is a streak tube. The image of the light to be analyzed is focused onto a photocathode at the input end of the streak tube. The photocathode emits electrons in response to the intensity of the light. The electrons, focused into a beam, are accelerated and deflected to a luminescent screen at the other end of the tube. This electron beam, impinging upon the screen, produces an intensified image of the light being analyzed. This image is then optically coupled to a CCD (charge-coupled device) imager, which digitizes the information for storage. To study the temporal variation of pulsed light a streak mode of operation is utilized whereby the electron beam is swept across the phosphor at a predetermined rate to provide the dimension of time along the axis of the swept image. To sweep the electron beam a pair of electrostatic deflection plates are provided in the streak tube (see Fig. 73.8). The position of the beam is linearly related to the voltage potential on the deflection plates. A linear voltage ramp is applied to the deflection plates to produce a linear sweep with respect to time. The sweep deflection circuit described produces the voltage ramp needed for the temporal study of the beams within the OMEGA system.

The multichannel streak camera is being developed at LLE to measure multiple-beam power balance and timing following the 3ω frequency-conversion crystals on OMEGA. The camera design is built around a commercial streak tube.[1] The primary design goal is to be able to perform a temporal display of ten OMEGA beams simultaneously along with two fiducial timing beams. With six of these cameras all 60 OMEGA beams can be analyzed simultaneously. Other goals include remote automated operation, fiber-optic light interface to the photocathode, and a highly reliable modular design. The modular design is required to facilitate serviceability and minimize down time in the event of circuit failure. Circuit malfunctions can be quickly diagnosed to the module level and a functioning module can then be interchanged without significant recali-bration of the instrument. The sweep module and streak camera frame are shown in Fig. 73.9.

Functionally the streak camera sweep module circuitry must synchronously output a bipolar, high-voltage ramp with a duration of 6 ns. The magnitude of the total end-to-end differential sweep voltage, as seen between the two deflection plates, is approximately 2000 V. This translates to a sweep of the electron beam across 40 mm of the streak tube display. Because errors in the linearity of the output ramp voltage translate directly to measurement errors in time resolution of the instrument, it is important to minimize deviations in the slope of the differential ramp voltage.
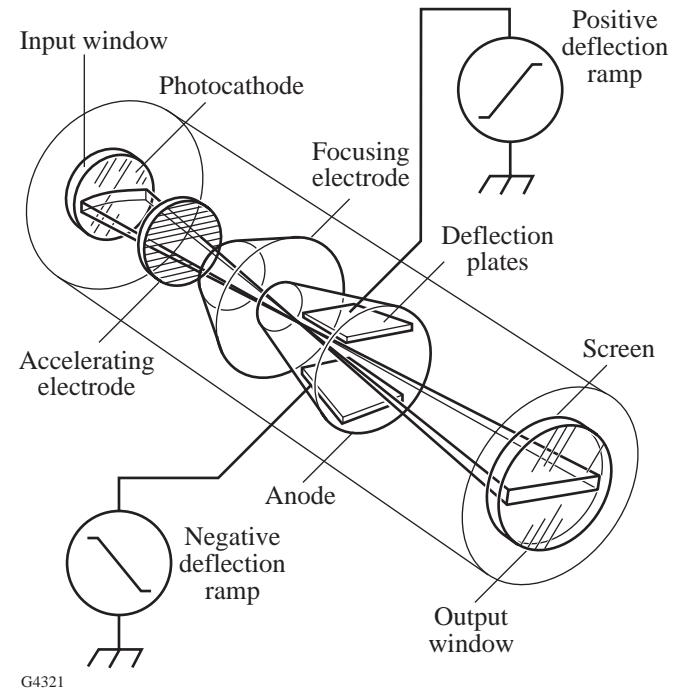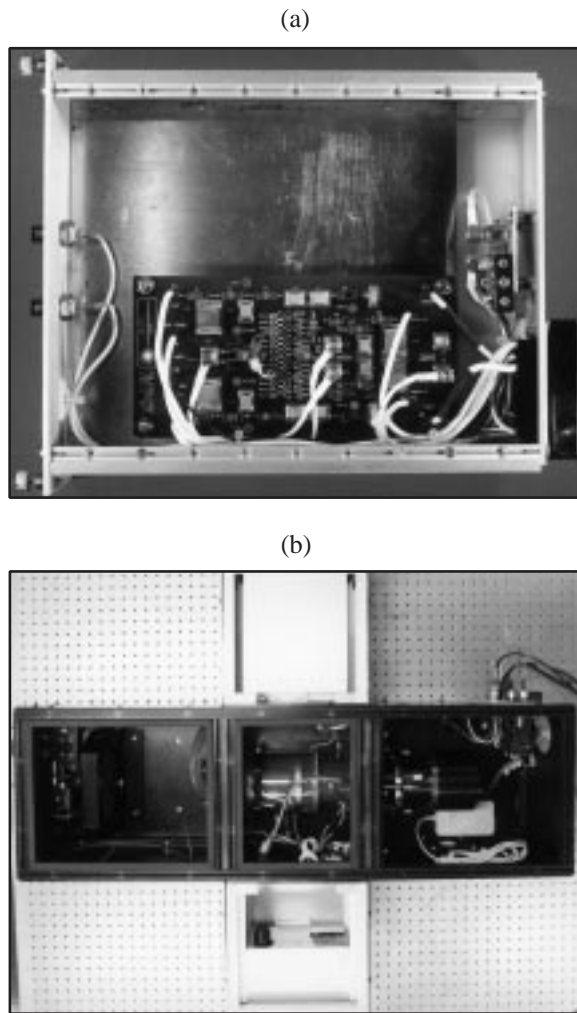

G4321

Figure 73.8
Streak tube schematic with deflection ramp sources.[1]

(a)

(b)

G4322

Figure 73.9
OMEGA multichannel streak camera: (a) sweep module and (b) streak camera frame.

The 6-ns sweep ramp is a high-bandwidth signal that requires care in design to account for nonideal component behavior. The particular problems encountered center around the stray reactive components, also known as parasitics, that are inherent in all electronic components. These parasitics are not usually a problem in low-frequency designs (<1 MHz) but become a significant contribution to performance, or lack thereof, in higher-frequency designs. The development of the streak camera sweep circuit accounts for the parasitics of the components to determine and correct for their effects. A circuit design accounting for all parasitics can become nearly impossible to solve in closed form resulting from the complexity of

the component parasitic models. To aid in the design, a circuit simulator computer program is used to model the circuitry with parasitics.

The modular design approach used here, while it does provide serviceability, requires additional mechanical interface complexity within the system interconnect structure. The interface complexity results from added connectors and increased wiring length to accommodate packaging. These extra wire lengths and added connectors introduce additional parasitic elements into the circuit interface that degrade high-bandwidth performance and must be accounted for in any modeling.

The goal of the sweep module design is achieved through the use of computer-aided analysis of the circuit design. The computer model includes parasitics that contribute to nonideal behavior. The initial design is conducted using this model. From the initial design a first-pass circuit "breadboard" is built and tested. An increasing complexity of parasitic elements is included until the model output compares to the actual breadboard circuit performance. With the model output matching the actual circuit, a rapid investigation of ways to optimize performance can then be accomplished. Also, anomalies in the circuit operation and performance measurement system can be analyzed. Although the main emphasis for use of the computer circuit model is to understand and correct the effects of the parasitics, it is also a valuable tool for circuit design and circuit optimization. The following is a comparison of the modeled and measured results for the sweep circuit along with a discussion on using the model to understand and correct undesired circuit behavior.

Streak Sweep Circuit Fundamental Design
The basic circuit concept for the deflection voltage generator in the sweep module is a voltage step applied to an RLC (resistor, inductor, capacitor) series resonant circuit as illustrated in Fig. 73.10. The deflection circuit is bipolar, and each deflection plate is driven by an equivalent RLC circuit (see Fig. 73.8). The step is positive for one deflection circuit and negative for the other. This creates a voltage ramp that is twice the amplitude of that applied to one plate only. The C in the resonant circuit is formed by the capacitance of the deflection plate in the streak tube. The voltage across the capacitor (deflection plate) is given by the following exponentially decaying sinusoidal form and is illustrated in Fig. 73.11:[2]

$$V_c(t) = V_{\text{step}}\left\{1 - e^{-\alpha \cdot t}\left[\cos(A\,\alpha \cdot t) + \frac{\sin(A\,\alpha \cdot t)}{A}\right]\right\}, \quad (1)$$
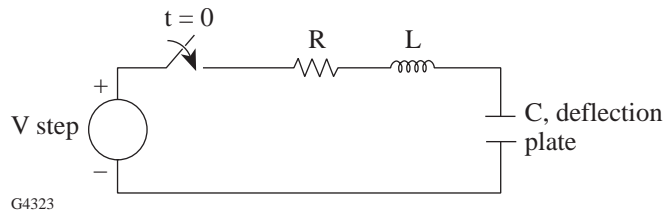
G4323

Figure 73.10
Basic RLC circuit with voltage step generator (R: resistor; L: inductor; C: capacitor).
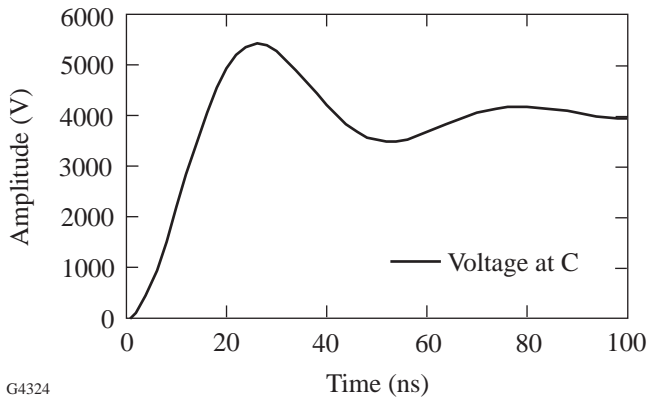

G4324

Figure 73.11
Exponentially decaying sinusoid produced by the step response of a series RLC circuit.

where

$$\alpha = \frac{R}{2L}, \quad A = \sqrt{4Q^2 - 1}, \quad Q = \frac{1}{R}\sqrt{\frac{L}{C}}.$$

Q represents the quality factor of the resonant circuit. The quality factor is the power stored by the resonant circuit divided by the power dissipated per cycle of the resonant frequency.

Ideally the sweep voltage should be a linear ramp. Although the voltage waveform produced by Eq. (1) is not linear, a section of the waveform in Fig. 73.11 between $t = 0$ and the voltage peak approximates a linear ramp. The linearity of this section is within a useable degree of accuracy for the streak camera sweep. The benefit in using the RLC resonator is that the sweep ramp can be adjusted by appropriate choice of R, L, and V_{step} without changing the circuit configuration. Another benefit is the low circuit complexity.

As an example of the achievable linearity, for a 4000-V step with a desired slope of 333 V/ns over a 2000-V range, the following values for R and L are used, given a 10-pF deflection plate capacitance: $R = 498\ \Omega$, $L = 6.3\ \mu H$. The waveform produced using these values has a slope of 306 V/ns at the start of the 2000-V sweep range (deflection plate voltage = 1340 V) and a slope of 310 V/ns at the end (deflection plate voltage = 3340 V). The center of the range has a slope of 333 V/ns as desired (deflection plate voltage = 2340 V). The slope deviates from an ideal linear slope by a maximum of 8.1% at the ends. This deviation translates into a maximum deflection-plate voltage error of 25 V, or a theoretical position error of 0.5 mm at the edges of the streak tube display used in the development. Choosing higher step voltages and higher circuit Q's will reduce this error.

To create the voltage step, a fast-switching, low-jitter, high-voltage circuit that can also accommodate high peak currents is necessary. Currently, the best device for this application is an avalanche transistor. An avalanche transistor is a bipolar junction transistor that can repetitively operate nondestructively in the current-mode second breakdown region.[3] When these transistors are off, they can hold off hundreds of volts with minimal conduction between the collector and emitter. When a small amount of carriers are injected into the base, the transistor goes from minimal conduction to current-mode second breakdown operation where the equivalent impedance between the collector and emitter drops to a few ohms. This action takes place in subnanosecond time frames. The transistor used for this project is the Zetex FMMT417.[4] This transistor is specifically designed for current-mode second breakdown operation. The FMMT417 transistor has a collector-to-emitter voltage self-breakdown of 320 V. Since each transistor can hold off >300 V, seven series-connected avalanche transistors are used for each of the two 2000-V step generators needed in the streak camera sweep circuit design. In a series-configured circuit only one of the transistors in the stack needs to be triggered to cause all of the remaining transistors to go into current-mode second breakdown. A schematic diagram of one sweep circuit of the bipolar sweep network is shown in Fig. 73.12.

Computer Modeling of the Sweep Circuit

The computer model for the sweep circuit is developed using Intusoft IsSpice4[5]—a commercially available version of the electronics-industry–accepted circuit analysis software called SPICE (Simulation Program Integrated Circuits Especially), which is based on Berkeley SPICE 3F.2.[6] This program accepts arbitrary circuit configurations and calculates

8
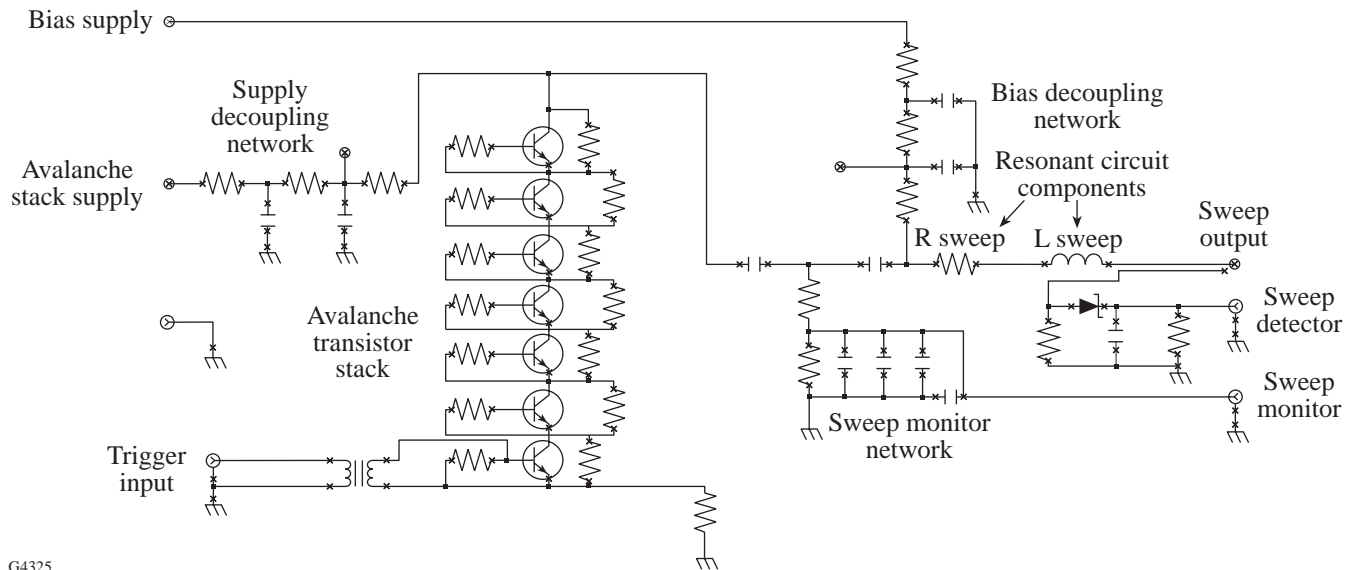
G4325

Figure 73.12
Schematic of the upper half of the multichannel streak camera sweep circuit.

currents and voltages throughout the circuit. A variety of analysis options are available in SPICE including dc, ac, and transient. For analyzing the streak sweep circuit, a transient, or time domain, analysis is performed. To simplify the model only half of the circuit is modeled, knowing that the other half provides identical results with inverted polarity. The sweep circuit is a bipolar, or balanced, configuration and can be divided into two equal parts along the line of symmetry. Each part can be analyzed independently without sacrificing accuracy. The model schematic is illustrated in Fig. 73.13.

A comparison of the schematics in Figs. 73.12 and 73.13 shows that there are significantly more components in the corresponding model network of Fig. 73.13. The components not shown in the actual circuit but shown in the model are the parasitic elements. These elements are determined through characterization of each component in the critical high-bandwidth signal path. Characterization is generally performed with calibrated test fixtures on a network analyzer. A network analyzer produces measurements of signal amplitude and phase in the frequency domain. The analyzer contains a swept calibrated signal source for excitation of the device under test and a tracking swept receiver for the measurements. One function of a network analyzer is to measure impedance of a component as a function of frequency. Care must be taken in these measurements to extract the actual component impedance from the characteristics of the test fixture. All components

have parasitic lead inductance as well as capacitance to ground. Between the terminals of a component there exists parasitic capacitance. Component losses are encountered as series and parallel loss resistance. The designer must determine which of the parasitics to consider when constructing component models. Some parasitics may not affect the analysis significantly and may be omitted, but a safe rule to follow is to include any parasitics where the designer is uncertain of their effect. Once the overall circuit model is completed the parasitics can be varied to determine their effect on circuit performance.

In the model in Fig. 73.13 the avalanche stack is replaced by a pulsed voltage source, V1. This source simulates the waveform observed across the avalanche stack. The actual avalanche stack dc supply is simulated by a short circuit to ground at R12 since an ideal voltage source has 0-Ω impedance. L1 is added to simulate the combined inductance of the avalanche transistors and the interconnect wiring. R3 simulates the combined on-state resistance of the avalanche transistors in current-mode second breakdown. The network to the left of the avalanche stack simulator, including R1, R2, and R12, simulates the stack supply decoupling network with parasitics. Likewise, the network including R5, R6, and R11 forms the decoupling network with parasitics for the bias supply, V2. The R and L for the slope-forming resonant circuit are represented by R14 and L8, respectively. The right-hand connection to R10 is the output of the module. This point is followed by a high
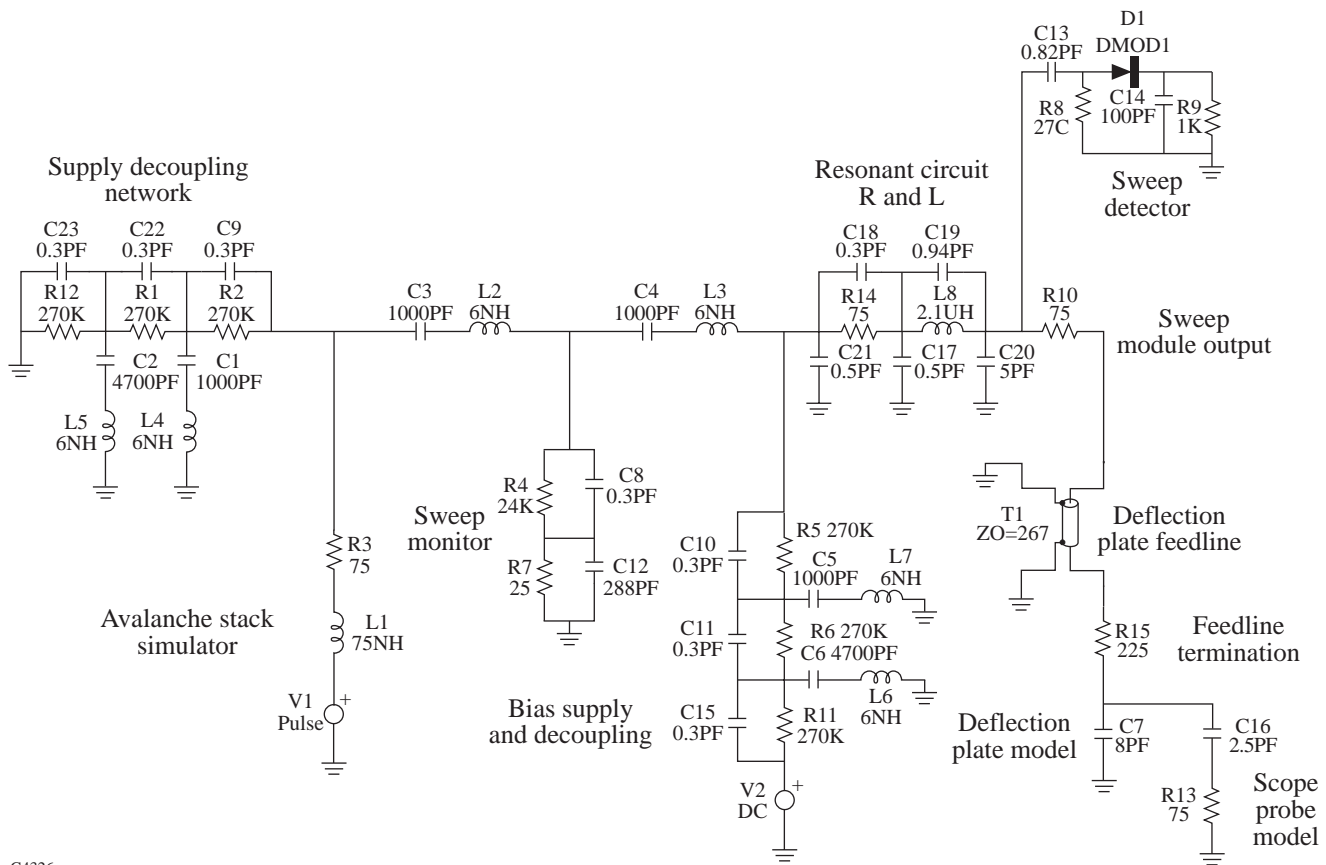
Figure 73.13
Schematic of the SPICE model for the multichannel streak camera sweep circuit.

impedance transmission line representing the feed wire to the deflection plate, C7. C16 and R13 represent a model of the oscilloscope probe used to monitor the performance of the sweep generator. The scope probe is modeled to determine its effective loading on the sweep waveform. The model also includes the sweep monitor network as well as the sweep detector network as seen in the original schematic of Fig. 73.12.

Model Results Versus Measured Results

Data from Figs. 73.14 and 73.15 illustrate a good correlation between the measured and model-predicted results for the sweep waveforms. The measured data is taken using a high-bandwidth oscilloscope connected to the deflection plates of the streak tube through 250-MHz-bandwidth, 100:1, high-impedance oscilloscope probes.[7,8] The plots in Fig. 73.14 are for one deflection plate voltage versus time. The other plate voltage is equivalent with opposite polarity. Figure 73.15 is the differential (slope) of the curves in Fig. 73.14. The desired theoretical slope is 167 V/ns for one deflection plate, or

333 V/ns for the differentially driven pair of plates to obtain a 6-ns sweep rate.

The curves presented are referenced in the time axis to the zero crossing of the deflection plate voltage. The illustrated curves extend past the active sweep time of 6 ns (active sweep time = −3 ns to +3 ns). Within the 6-ns time window the maximum voltage difference between the measured and modeled results is 29 V. The average slope within the window for the measured data is 167 V/ns and 168 V/ns for the SPICE data. The standard deviation of the measured slope from 167 V/ns is 14 V/ns and 10 V/ns for the SPICE model.

Utility of the SPICE Model

One of the fundamental uses of the SPICE model is to evaluate the performance of the sweep network with respect to the values of R and L, the sweep-rate–determining components. The initial values for these parts are determined by theoretical calculations base on Eq. (1) for the basic RLC
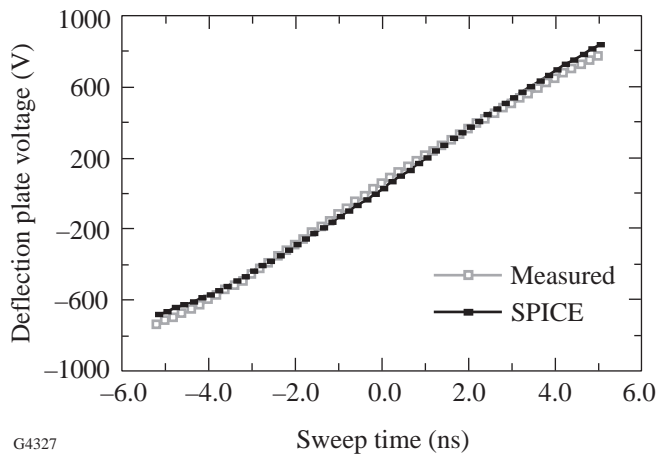
G4327

Figure 73.14
Measured sweep voltage and SPICE calculation.

G4328

Figure 73.15
Measured sweep slope and SPICE calculation.

resonator circuit. The predicted performance of the actual circuit with the initial theoretical values can then be evaluated using the model. The values are then iteratively optimized within the model to account for the parasitics within the sweep module and streak camera. A set of values that meets the performance criteria is then determined prior to actually mounting the components in the hardware. This approach is used to develop the streak module with the results as presented in Figs. 73.14 and 73.15.

Another use for the model is to analyze and correct anomalies in the sweep waveform observed during the sweep module development. Three anomalies were found that affected the camera performance: (1) the effect of the oscilloscope probe loading on the sweep waveform; (2) a small, damped, high-frequency sinusoid superimposed on the sweep waveform; and (3) an inflection in the start of the sweep waveform.

The loading effects of the oscilloscope probes can only be evaluated experimentally by comparing the spacing of accurately timed fiducial light pulses on the streak camera output with and without the probes attached. During the streak camera development, short fiducial laser pulses with a precise period of 500 ps were applied to the photocathode of the streak tube. The pulse train from the fiducial laser appears as an intensity-modulated streak on the output screen. The distance between the peak intensity points on the output 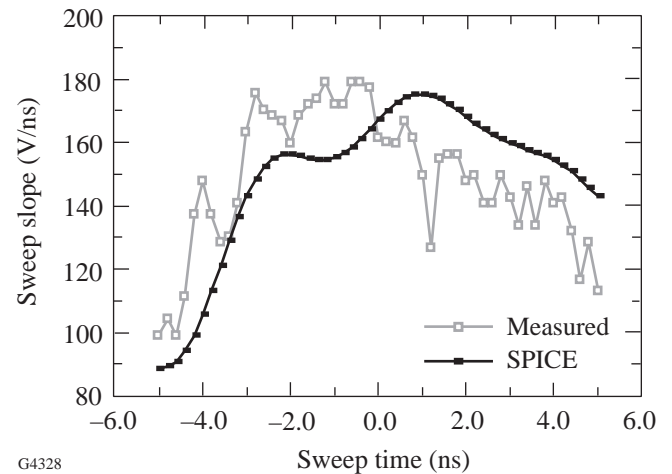screen is directly related to the sweep rate ramp applied to the deflection plates. Comparing the distance between the peaks with and without the probes connected determines the effect of the probes on sweep

rate. Using the SPICE model, a trivial effort is required to remove the simulated scope probes and calculate the change in the sweep speed. Figure 73.16 shows the change in the sweep speed as calculated by the SPICE model. The model-calculated sweep rate is 6.4 ns with the probes and 5.6 ns without. The measured sweep-rate change, using the fiducial method, is 6.6 ns with the probes and 5.6 ns with the probes removed. Good agreement is shown between the two methods. With this performance agreement the sweep-forming R and L values can be easily optimized in the model and applied to the actual circuit to compensate for oscilloscope probe loading. This is far less time consuming than optimization by iteratively changing the components in the actual sweep module and repeating the fiducial streak measurements. Also, knowing the magnitude of the probe-loading change allows actual oscilloscope-measured sweep voltage waveforms to be scaled to predict performance without the oscilloscope probe loading necessary to make the measurement.

During the initial tests of the streak camera a small sinusoidal modulation with a period of approximately 6 ns was observed superimposed on the oscilloscope display of the sweep ramp. This sinusoidal modulation was verified with streak measurements of the 500-ps-period fiducial optical timing pulse train in similar fashion to that used to determine effects of scope probe loading. Figure 73.17 shows the oscilloscope-measured sweep with the superimposed sinusoid. The model result verifies the oscilloscope measurements and is also plotted in Fig. 73.17. Figure 73.18 illustrates the verification plots from the fiducial measurements. This data agreement

proves that the problem is not just an artifact of the oscilloscope measurement. From the model it has been determined that the deflection-plate feed line is acting as a constant impedance transmission line terminated by the capacitive deflection plate. This reactively terminated transmission line forms a resonant circuit that has a center frequency close to that of the superimposed sinusoid. Network analyzer measurements of the feed line indicate that it has a characteristic impedance of 267 Ω with a delay of 1.5 ns. To remove the resonance problem the feed line is made lossy through the inclusion of distributed resistance. Theoretically, this decreases the Q of the resonant circuit formed by the feed line and reduces the sinusoidal current at resonance without significantly affecting the sweep

ramp. Results from the model demonstrate that this approach is capable of removing the sinusoid. The plot in Fig. 73.19 is the result produced by the model with the feed line terminated to remove the resonance condition. It was later found that a lumped resistance equal to the characteristic impedance of the line could be connected in series at the deflection plate to produce the same result. This fix is supported by oscilloscope sweep waveform measurements as illustrated in Fig. 73.14.

The last problem observed relates to an inflection in the measured sweep waveforms near the start of the sweep ramp. This is again supported with the results of the model as illustrated in Fig. 73.20 near 3 ns. In this figure the time axis
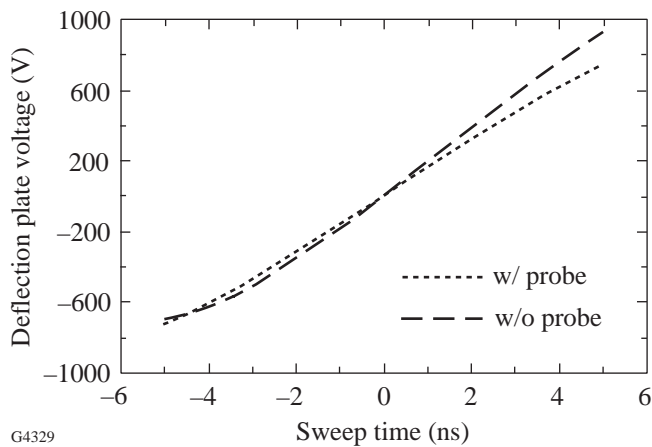
G4329

Figure 73.16
Calculated sweep-speed change with oscilloscope probe loading.
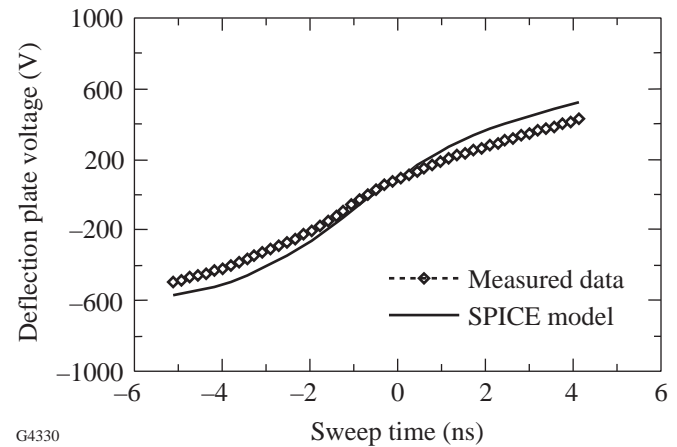
G4330

Figure 73.17
Measured sweep with superimposed sinusoid.
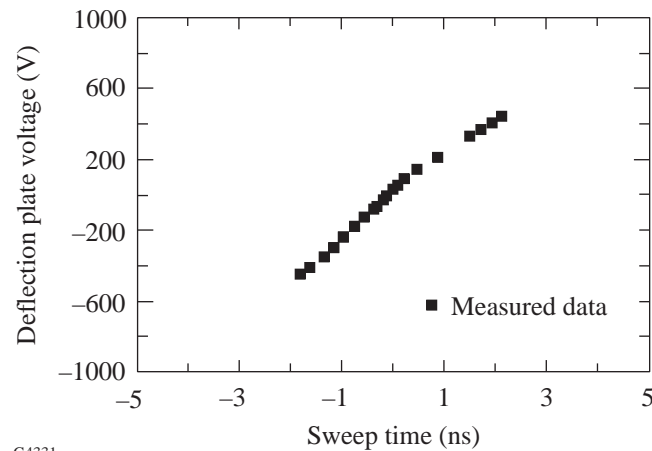
G4331

Figure 73.18
Measured sweep using optical fiducial marks.
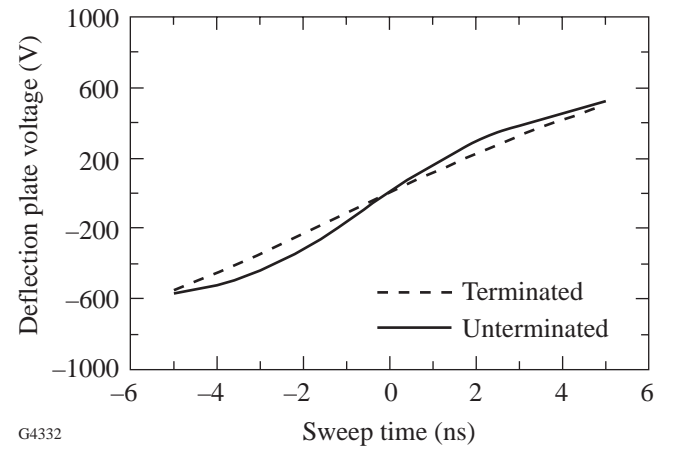
G4332

Figure 73.19
Calculated sweep with and without feed-line termination.

reference is at the start of the sweep waveform. Investigation of the inflection through its sensitivity to component value changes in the model led to the understanding of its cause. The inflection is caused by the resonance of the sweep-speed inductance (L8 in Fig. 73.13) with its parallel parasitic capacitance (C19). Using the model an investigation into the effect of the parasitic capacitance can be easily generated. It is found that a nonrealizable inductor is needed (an inductor with minimal parasitic C) to remove the inflection and that this problem cannot be eliminated. This analysis cannot be accomplished without the model since the model provides the freedom to change component characteristics outside the constraints imposed by realizable devices. Figure 73.21 shows the results of the model as the parasitic capacitance of the sweep inductor is varied. The point of this figure is that less inflection is produced by smaller parasitic capacitance.

Since the last problem is not resolvable using realizable components, the choice is made to alter the active sweep ramp range on the sweep waveform to avoid having the inflection within the active area of the sweep waveform. The operation range is altered by increasing the bias supply voltage, keeping all other circuit parameters fixed. In the waveform of Fig. 73.11, this is equivalent to setting the 2000-V active sweep ramp range to a section of the waveform closer to the peak voltage than directly in the middle between the waveform start and the peak. Care is taken to not move the range too close to the peak since linearity would be degraded at the end of the sweep ramp near the peak.

Conclusions

In this work we show that time-domain circuit modeling and simulation of the multichannel streak camera sweep circuit using SPICE is an accurate method of analysis. The accuracy is a direct result of the attention to the parasitics for the components and interconnections in the circuitry. The parasitics, while not a severe limitation in low-frequency analysis, are a great influence to the model results in wide-bandwidth and high-frequency analysis as encountered in the sweep circuit. Component parasitic elements are generally extracted from network analyzer terminal impedance measurements on individual components and circuit interconnects. The necessary complexity of the parasitic model utilized is determined by the calculated effect of the parasitic elements within the circuit application. A SPICE circuit model, when properly constructed using the parasitic component models, is a useful tool to analyze and optimize a design. The main benefit of the model is to present a theoretical evaluation of a circuit with parasitic elements where the complexity of obtaining a closed-form analysis is intractable. Optimization using the model analysis can help greatly in reducing the effects of parasitics. The theoretical computer analysis allows rapid circuit optimization iterations as compared to equivalent hardware implementation and measurement of the change. The model is extremely valuable in diagnosing anomalies in circuit performance. An accurate model can also provide useful performance-limit analysis through ideal, parasitic-free, component substitution.

G4333

Figure 73.20
Sweep inflection.

G4334
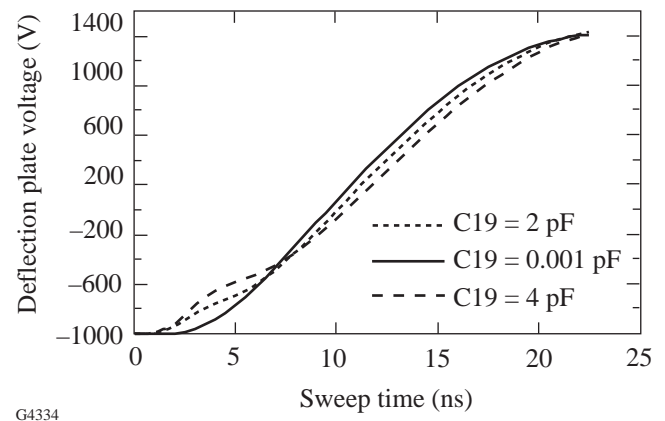
Figure 73.21
Calculated sweep with varying values of parasitic capacitance, C19, for the sweep-forming inductor, L8.

Utilizing the SPICE circuit model for the multichannel streak camera sweep module, an optimized design is developed that accommodates the component parasitics and parasitics introduced by the modular-design concept. Performance of the circuitry is optimized to remove, or accommodate, deflection-plate feedline effects, individual component parasitics, and oscilloscope probe loading. Sweep performance is optimized without the normal time-consuming change and test iterations necessary with a hardware-only approach.

ACKNOWLEDGMENT

REFERENCES

1. P510PSU streak tube, Philips Photonics, Slatersville, RI 02876.

2. S. W. Thomas, R. L. Griffith, and W. R. McDonald, Opt. Eng. **25**, 465 (1986).

3. R. J. Baker, Rev. Sci. Instrum. **62**, 1031 (1991).

4. Zetex, Inc., Commack, NY 11725.

5. Intusoft, San Pedro, CA 90733-0710.

6. SPICE 3F.2, developed by the Department of Electrical Engineering and Computer Sciences, University of California, Berkeley, CA 94720.

7. Oscilloscope, Model No. 9360, LeCroy, Chestnut Ridge, NY 10977.

8. Oscilloscope probe, Model No. P5100, Tektronix, Inc., Wilsonville, OR 97070.

D-^{3}He Protons as a Diagnostic for Target ρR

Areal density (ρR) is an important parameter for measuring compression in ICF experiments. Several diagnostics employing nuclear particles have been considered to deduce this quantity in implosions. One diagnostic is the knock-on deuterons,[1] i.e., deuterons produced by the elastic scattering of fuel deuterons and primary neutrons from the DT reaction. The number of knock-ons contained in the high-energy peak (typically 16% of the total produced) of the emergent spectrum is proportional to the fuel areal density [$(\rho R)_f$] and the position of the peak provides a measure of the plastic areal density [$(\rho R)_{CH}$]. This diagnostic, however, is limited to $(\rho R)_{CH} \sim$ 100 mg/cm^2 as higher compressions can considerably distort the emergent spectra, preventing a reliable interpretation of the signal.

For higher-density implosions, high-energy neutrons produced from the tertiary fusion reactions of the knock-on deuterons and tritons with the corresponding thermal fuel ions[2] have been considered as a diagnostic for fuel ρR. For instance, for "small" ρR (like those on OMEGA), the number of tertiary neutrons produced is proportional to $(\rho R)_f^2$, yielding a measure for the fuel areal density. However, since these neutrons are produced in tertiary reactions, their numbers are significantly lower relative to primary yields (typically by 5 to 6 orders of magnitude). This necessitates the development of new, sensitive neutron detectors.

An alternate technique for measuring high ρR is to use the primary protons from the D-^{3}He reaction, obtained by adding ^{3}He to the fuel. This diagnostic has the advantage that the charged-particle spectrometer for OMEGA,[3] currently being designed at MIT, can be used to detect the protons. In addition, these protons can serve as a diagnostic for cryogenic DD targets, which are being considered as initial cryogenic targets on OMEGA. DD targets do not have the drawbacks associated with the radioactivity of tritium and can be useful for standardizing laboratory techniques for cryogenics.

In what follows, we introduce the D-^{3}He proton diagnostic and set limits on the areal densities measurable through this method. We then examine the model dependence of this diagnostic by comparing results from a detailed time-dependent simulation and a simple model characterized by the conditions in the target around peak thermonuclear burn. This diagnostic is then discussed in the context of DT targets. Future areas of interest relating to this diagnostic will be discussed briefly.

The Diagnostic

The primary D-^{3}He protons are produced at an energy of 14.7 MeV from the reaction

$$D + {}^3\text{He} = \alpha + p\,(14.7 \text{ MeV}). \quad (1)$$

Protons lose energy as they traverse the target, and the energy loss of the emerging protons is proportional to ρR. Thus, unlike the knock-on diagnostic, which can provide a measure of the fuel and the tamper ρR individually, this diagnostic can be used to measure only the *total* ρR of the target. The interpretation of the signal can be complicated by the fact that this energy loss can be both temperature and density dependent.

Prior to its use on a cryogenic target, the D-^{3}He proton diagnostic can first be tested on current OMEGA gas targets. We demonstrate the diagnostic through a simple model for a typical gas target represented as a hot core (at 4 keV) surrounded by cold plastic (at 0.8 keV). The model serves to illustrate the limits of the diagnostic in terms of both ρR and temperatures in the target. We choose a fuel ρR of 30 mg/cm^2 corresponding to the typical fuel areal density during the time that the protons traverse the target in detailed 1-D simulations. The temperatures in the model are characteristic of the conditions during the peak thermonuclear burn. The emergent D-^{3}He proton spectrum, i.e., the normalized number of protons per unit energy interval, is shown in Fig. 73.22(a) for various values of plastic ρR. The figure shows the greater slowing down of the protons with increasing ρR of the plastic.

To examine the reliability of this diagnostic in the context of its sensitivity to temperatures in the target, we vary the electron temperatures in the plastic [Fig. 73.22(b)]. For a lower plastic

temperature the spectra are influenced only for lower proton energies (which occur for larger values of ρR). This can be easily explained through the energy-loss formulae that contribute to the spectrum.[4] We first note that the energy loss of the protons is dominated by losses to electrons. In addition, the D-^{3}He protons have much higher velocities than the electrons in the target for a wide range of energies and temperatures. In this regime, the thermal motion of the electrons can be ignored altogether. (The energy-loss mechanism is then through the

excitation of collective plasma oscillations in the plastic.) For OMEGA targets the cold plastic can have temperatures of 1 keV or less and thus will have only a small effect on the spectrum of the very energetic protons.

Detailed simulations through the 1-D code *LILAC*[5] of the same target indicate that the maximum ρR achieved in the target is about 70 mg/cm^2 for the fuel and 170 mg/cm^2 for the plastic [Fig. 73.23(a)]. The protons, however, provide a

TC4610
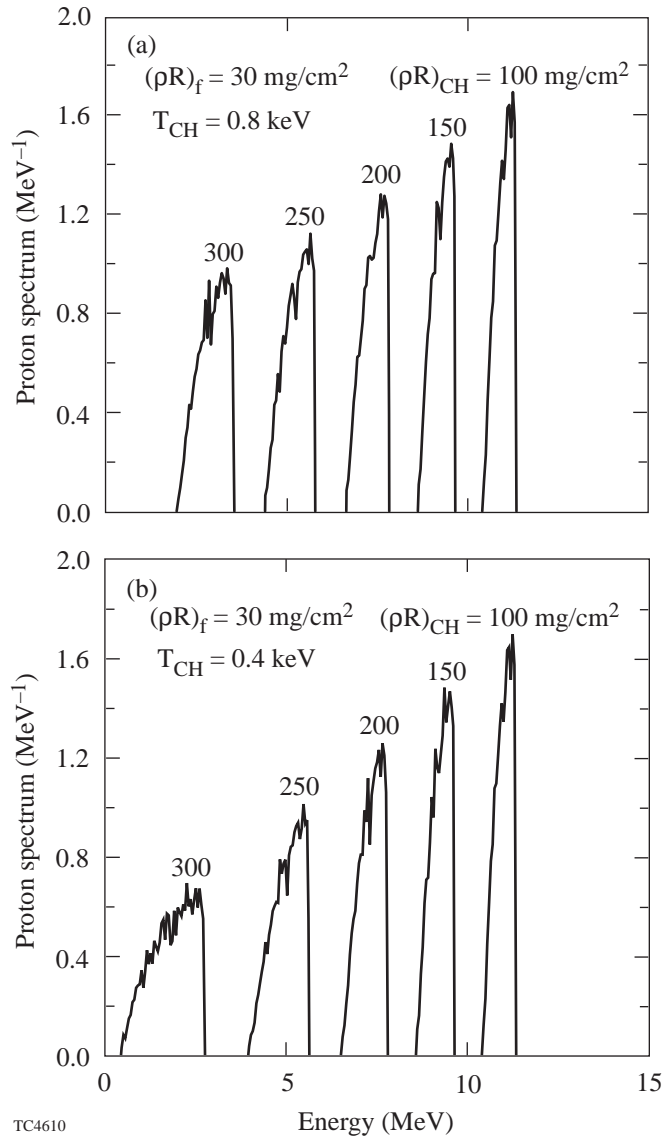
Figure 73.22

(a) Emergent D-^{3}He proton spectra (the normalized number of protons per unit energy interval) for the model (see text) with the choice of ρR as shown in the figure and with the plastic at a temperature of 0.8 keV. (b) Spectra of emergent protons with plastic at a temperature of 0.4 keV.

TC4611
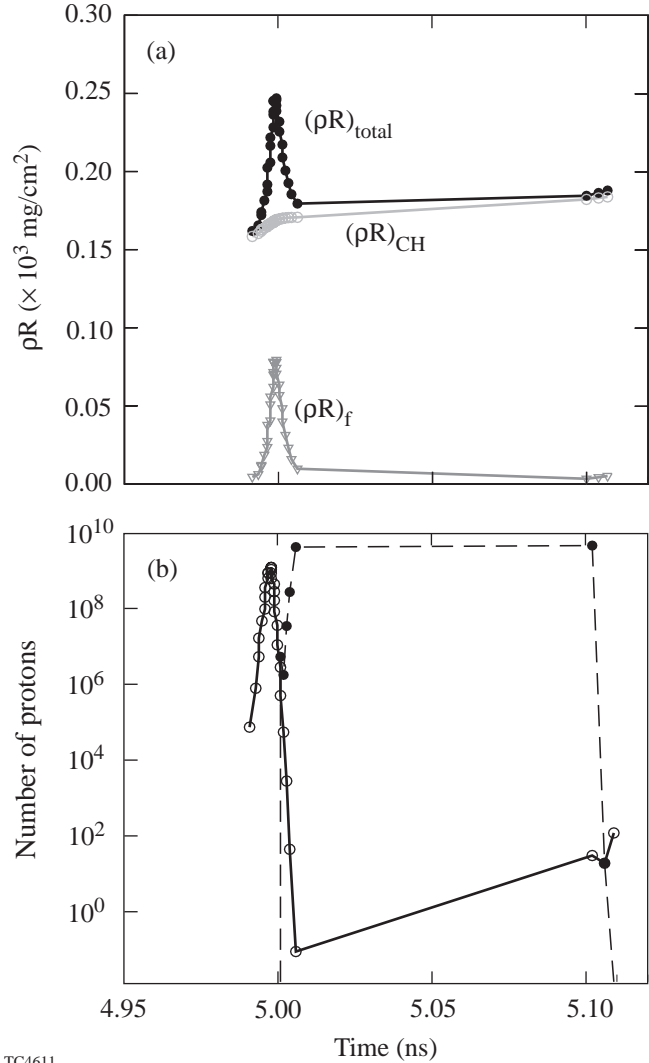
Figure 73.23

(a) Results from 1-D *LILAC* simulations for the ρR history of the target in Fig. 73.22(b); fuel ρR shown in triangles, plastic ρR shown in open circles, total target ρR shown in solid circles. (b) History of proton production in the target (open circles) and proton emission from the target (solid circles). The emergent protons measure an average total $\rho R \sim 200$ mg/cm^2.

measure of an average value of ρR, which is determined by the time that they traverse the target and can, in general, be less than the maximum value. Thus, by comparing the ρR history in Fig. 73.23(a), the history of proton production in the target [open circles in Fig. 73.23(b)], and the time history of protons exiting the target [solid circles in Fig. 73.23(b)], one can calculate the range of ρR measured through this diagnostic. The plastic ρR remains nearly constant at 170 mg/cm² during the time the protons traverse the target yielding this value as the average $(\rho R)_{CH}$. Furthermore, while a majority of the protons are produced near the peak value of $(\rho R)_f$ (70 mg/cm²), they exit the target when the fuel ρR is lower (10 mg/cm²), so that the protons sample a range of fuel ρR. Since the ρR of the plastic is so much larger than the average ρR of the fuel, the energy loss of the D-³He proton should be characterized by $(\rho R)_{CH}$ in this example. The emergent proton spectrum from this simulation is shown in Fig. 73.24. One-dimensional time-dependent profiles obtained from *LILAC* were used as an input to the Monte Carlo particle-tracking code *IRIS*,[6] which calculated the spectrum emerging from the target. Since the detailed simulation indicates that the average $(\rho R)_{CH}$ measured by the protons is about 170 mg/cm², Fig. 73.24 must be compared with a model calculation (in Fig. 73.22) corresponding approximately to this value of the plastic fuel areal density. The comparison shows that the time-dependent evolution of the target has little influence on the position of the peak of the emergent proton spectrum. Both the model and the detailed
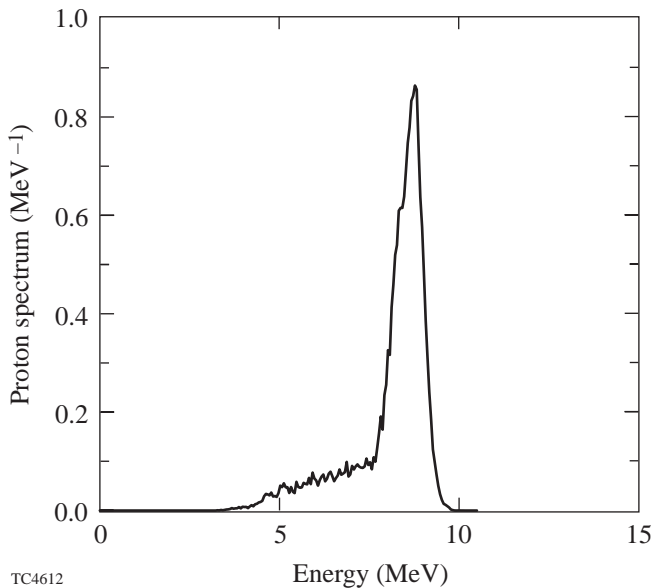
simulation peak at approximately the same energy. This feature will simplify the interpretation of an experimental signal; the position of the peak depends only on the knowledge of the fuel and plastic ρR. The width of the emergent spectrum, on the other hand, can depend on the details of the spatial profile of proton production, density, and fuel temperature history of the target. Even so, the energies at the FWHM of the spectrum provide a reasonable measure of the range of ρR in the target when compared to the model in Fig. 73.22. Some energy loss also takes place in the hot-fuel region. The low-energy tail is due to protons produced in the innermost regions of the hot fuel slowing down in the fuel, followed by energy loss in the plastic. For a target with lower fuel ρR, the slowing down in the fuel will be less significant and the range of ρR can be inferred more reliably. For larger $(\rho R)_f$, this model dependence must be constrained through comparisons of detailed simulations with simple models approximating conditions during thermonuclear burn.

The Diagnostic for DT Targets

The discussion thus far applies specifically to targets containing only deuterium and ³He. The proton signal from these targets can be unambiguously identified as that due to the D-³He proton. This signal is significantly larger than any other proton spectrum such as primary protons elastically scattered off fuel ions in the relevant energy region. We now discuss the diagnostic in the case where ³He is added to the fuel that includes tritium in addition to deuterium.

Background related to the presence of tritium in the target is caused by the 14.1-MeV primary neutron from the DT reaction

$$D + T = \alpha + n\,(14.1\ \text{MeV}). \qquad (2)$$

One source of background arises from the elastic scattering of the 14.1-MeV primary DT neutrons off the protons in the plastic. The scattered protons have energies up to the maximum of 14.1 MeV.

Another important source of background arises when the 14.1-MeV neutron breaks up the deuteron in the reaction

$$D + n = 2n + p, \qquad (3)$$

where protons are produced with energies up to 11.8 MeV.

Figure 73.24
Cumulative spectrum of D-³He protons escaping the target from a 1-D simulation.

As seen in Fig. 73.22, the D-³He proton spectrum can be significantly shifted downward due to energy losses in the

target for the range of ρR expected in high-density implosions on OMEGA. The interpretation of the diagnostic proton spectrum can then be complicated by protons from the background mentioned above in the relevant energy range. Figure 73.25 shows the emergent proton spectrum from the earlier simple model representation [corresponding to Fig. 73.22(a) with $(\rho R)_{CH}$ = 150 mg/cm^2] now being used for a gas target containing tritium in addition to deuterium and ^{3}He. The end point of the spectrum is at the maximum energy of the elastically scattered protons at 14.1 MeV. The proton background due to the deuteron breakup reaction is contained in Fig. 73.25 (and extends up to 4.5 MeV downshifted from the maximum of 11.8 MeV due to energy losses in the plastic). The D-^{3}He proton spectrum (whose range is shown as a dotted line) appears as an easily identifiable peak over the spectrum from the two sources of background mentioned above. A detailed simulation (not shown here) also shows the promise of this diagnostic for gas DT targets; the signal is somewhat broadened (with a width similar to Fig. 73.24) and is dominant over the background.

Several comments in the context of cryogenic targets are in order here. The background protons due to scattering in the plastic will be significantly reduced in this case because most of the plastic will have been ablated from the target before thermonuclear burn.

In Fig. 73.26(a) we show the emergent proton spectrum from a 1-D simulation of an OMEGA cryogenic DT target. (The target comprises solid deuterium and tritium in a 1:1 ratio and encloses D-^{3}He gas. We ignore any confining plastic remnants that may exist during thermonuclear burn.) The D-^{3}He signal [shown as a dashed line in the region of its overlap with protons from the $(n,2n)$ reaction] extends from about 10 MeV to 14 MeV and is significantly broadened principally due to the time evolution of densities in the target. This dependence on the hydrodynamic evolution of the target can be constrained by comparing the emergent proton spectrum with that from a range of models similar to those used for the gas target in Fig. 73.22. However, the large $(n,2n)$ proton signal (about three orders of magnitude more protons are produced in the deuteron breakup reaction than in the D-^{3}He fusion) extends to about 11.8 MeV and makes the interpretation of the signal very dubious.

One possible method to lower this background is to include different proportions of deuterium and tritium in the solid fuel in order to reduce the yield of neutrons from the DT reaction and to reduce the numbers of protons from the $(n,2n)$ reaction. The proton spectrum from a target where the deuterium and tritium are in a ratio of 1:9 respectively is shown in Fig. 73.26(b). The number of background protons is significantly reduced, and the proton signal dominates in the region of overlap with the background. Thus, with some target optimization an unambiguous D-^{3}He proton signal can be obtained from cryogenic DT targets on OMEGA. In this context, tertiary neutrons mentioned earlier are a more attractive diagnostic for cryogenic DT targets because they have no background, place no constraints on the targets, and are applicable to higher densities.

Summary

In summary, the D-^{3}He proton spectrum is being considered as a means for inferring the total ρR of cryogenic DD targets. Using a gas target capable of achieving high areal densities, we have demonstrated that this diagnostic can be useful for up to $\rho R \sim 300$ mg/cm^2 for targets containing only D and ^{3}He. The reliability of this diagnostic is strengthened by its weak sensitivity to temperatures in the cold regions of the target for a wide range of ρR. For targets containing tritium, the interpretation of the signal is more difficult due to background arising from the 14.1-MeV primary DT neutron.
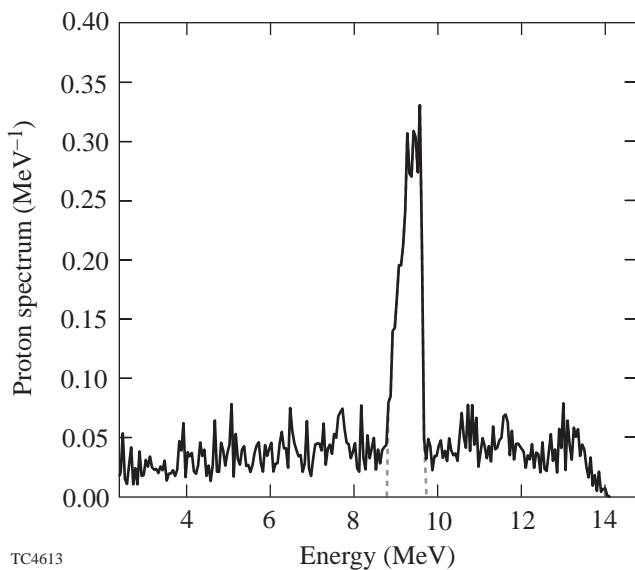

Figure 73.25
Spectrum of protons escaping a gas target containing DT and ^{3}He and modeled as described in the text. The peak is due to the D-^{3}He proton signal, and the background comprises protons from the deuteron breakup reaction and the elastic scattering of protons in the plastic. The dotted extension of the peak shows the range of the D-^{3}He proton signal.
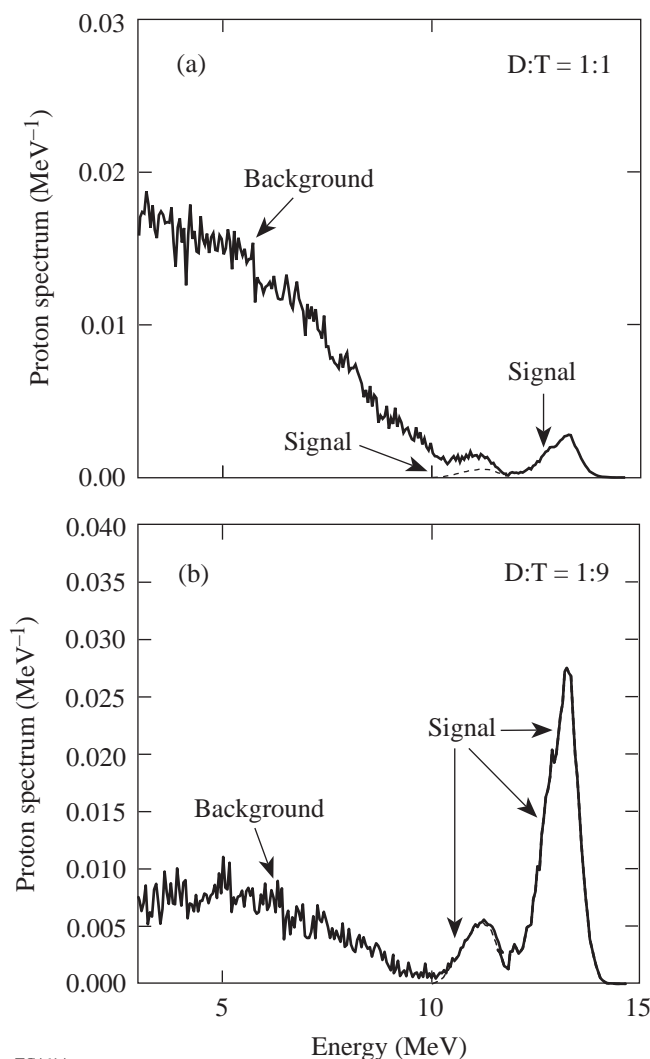
Figure 73.26
(a) Spectrum of emergent protons from an OMEGA cryogenic target with D:T = 1:1 in solid DT. D-³He protons extend from about 10 MeV to 14 MeV. The dashed line is the extension of the signal in the region of its overlap with the background protons from the deuteron breakup reaction, which extends to 11.8 MeV. (b) Spectrum of protons from an OMEGA cryogenic target with D:T = 1:9.

Future Applications

This diagnostic could also serve as a method to measure gross asymmetries in the target that may arise due to energy imbalance in the beams, laser mispointing, etc. The D-³He protons are produced isotropically, and any angular dependence of the proton yield or the spectrum is an indication of asymmetries in the target. Experimentally, track detectors placed strategically at various angles around the target could be used in conjunction with the charged-particle spectrometer to measure the various emergent proton spectra. Fuel areal densities could be inferred by comparing these spectra to calculations that include analytic angular variations in the target profiles. These measurements would track only gross variations in density (and temperature) constraining the calculations; inclusion of only "long"-wavelength perturbations to spherical symmetry should adequately model the emergent proton spectra. The Monte Carlo particle-tracking code *IRIS* is currently being modified with a view toward including such asymmetries in target profiles. Diagnostics for asymmetries in the target could then be developed.

REFERENCES

1. S. Skupsky and S. Kacenjar, J. Appl. Phys. **52**, 2608 (1981).

2. D. R. Welch, H. Kislev, and G. H. Miley, Rev. Sci. Instrum. **59**, 610 (1988). See also Laboratory for Laser Energetics LLE Review **69**, 46, NTIS document No. DOE/SF/19460-152 (1996). Copies may be obtained from the National Technical Information Service, Springfield, VA 22161.

3. D. G. Hicks, C. K. Li, R. D. Petrasso, F. H. Seguin, B. E. Burke, J. P. Knauer, S. Cremer, R. L. Kremens, M. D. Cable, and T. W. Phillips, Rev. Sci. Instrum. **68**, 589 (1997).

4. J. D. Jackson, *Classical Electrodynamics*, 2nd ed. (Wiley, New York, 1975).

5. *LILAC*, E. B. Goldman, Laboratory for Laser Energetics Report No. 16, University of Rochester (1973).

6. *IRIS*, S. Cremer, University of Rochester Laboratory for Laser Energetics (unpublished).

Growth Rates of the Ablative Rayleigh–Taylor Instability in Inertial Confinement Fusion

In recent years, several authors[1–14] have studied the linear growth of the Rayleigh–Taylor (RT) instability in ablation fronts accelerated by laser irradiations. The determination of the instability growth rate is crucial to the success of inertial confinement fusion (ICF)[15,16] because an excessive distortion of the front could lead to a severe degradation of the capsule performance with respect to the final core conditions by seeding the deceleration-phase RT instability and preventing the onset of the ignition process.

For a successful implosion, ICF targets must be designed to keep the RT growth at an acceptable level. Because of the complexity of 2-D or 3-D codes and the mesh refinement needed to simulate hydro-instabilities, 2-D or 3-D simulations cannot be routinely used to study the capsule stability and mixing. The best approach to target design is to carry out a preliminary analysis by using 1-D simulations to study the main characteristics of the implosion and then processing the data with a mixing model to study the evolution of the instability and the induced rms deviations. Once the preliminary design is completed, the optimization can be carried out by using 2-D or 3-D codes. Since the mixing model predictions are based on the initial perturbation amplitude and linear growth rates, it is very important to generate an accurate and reliable growth-rate formula to be used in conjunction with the 1-D code output.

According to the linear classical theory,[17] the interface between a heavy fluid of constant density ρ_h and a light fluid of constant density ρ_l in a gravitational field g pointing toward the light fluid is unstable. A small perturbation would grow exponentially in time, $\sim e^{\gamma_{cl} t}$, at a rate

$$\gamma_{cl} = \sqrt{A_T^{cl} \, kg} \,, \tag{1}$$

where $A_T^{cl} = (\rho_h - \rho_l)/(\rho_h + \rho_l)$ is the Atwood number and k is the perturbation wave number.

If the density is smoothly varying between the two fluids and the minimum density-gradient scale length $L_m = \min \left| \rho/(d\rho/dx) \right|$ is finite, then a distinction must be made between those modes with wavelength larger and smaller than L_m. The long-wavelength modes ($kL_m \ll 1$) are not affected by the finite L_m and grow according to Eq. (1), while the short-wavelength modes ($kL_m \gg 1$) are localized inside the smooth interface and grow at the rate[18]

$$\gamma = \sqrt{\frac{g}{L_m}} \,. \tag{2}$$

An asymptotic formula reproducing the results at short and long wavelengths can be easily generated by inspection of Eqs. (1) and (2) leading to

$$\gamma = \sqrt{\frac{A_T^{cl} kg}{1 + A_T^{cl} kL_m}} \,. \tag{3}$$

In laser-accelerated targets, the ablation process and the thermal transport add a great deal of complication to the evolution of the instability. The overdense target material (with density ρ_a) is ablated at a rate $\dot{m} = \rho_a V_a$, where V_a is the ablation velocity. The latter represents the penetration speed of the ablation front in the overdense target. The ablated material blowing off the target rapidly expands inside the ablation front and accelerates to large velocities relative to the overdense targets.

Several authors[1–14] have shown that the ablation process leads to a reduction of the instability growth rate. The so-called ablative stabilization was first discussed in Ref. 1 and thereafter extensively studied in Refs. 2–13. Because of the mathematical complexity of the problem, simplified analytic models such as the sharp boundary model have been used to describe the linear phase of the instability. However, such models are

heuristic in nature as they lack a proper closure, which is left to the physical intuition. For such reasons, different authors using different closure equations have produced different growth-rate formulas (see Refs. 1, 5, and 12). Numerical simulations have confirmed the stabilizing effect of ablation and indicated that, in some cases (as described later), the growth rate can be approximated by the following formula:

$$\gamma = 0.9\sqrt{kg} - 3.1\, kV_a. \tag{4}$$

Equation (4) was derived in Ref. 3 by fitting the numerical solution of the linearized conservation equations including ablation and electronic heat conduction. As stated in the **Growth Rates** section, Eq. (4) does not correctly reproduce the growth rates in the presence of a significant radiation energy transport leading to smooth density profiles. It is important to observe that Eq. (4) does not include the stabilizing effect of finite density-gradient scale length and it can only be applied to very sharp ablation fronts or modes with $kL_m \ll 1$.

Only very recently, the analytic stability theory of accelerated ablation fronts has been carried out in the limit of subsonic ablation flows[8–12] (i.e., fronts with ablation velocity less than the sound speed at the ablation front) by using complicated asymptotic matching techniques. Subsonic ablation fronts are characterized by two dimensionless parameters:[10] the Froude number $Fr = V_a^2 / gL_0$ and the power index for thermal conduction $v\,(\kappa \sim T^v)$. Here, L_0 is the characteristic thickness of the ablation front, which is proportional to the minimum value of the density-gradient scale length[6] $L_m\left[L_0 = L_m v^v / (v+1)^{v+1}\right]$. The analytic theory developed in Refs. 8–11 shows that the instability growth rate is strongly dependent on the magnitude of the Froude number. For large Froude numbers,[9,10] the main stabilizing effects are ablation and blowoff convection, and the growth rate can be written in the following form:[9,12]

$$\gamma = \sqrt{A_T kg - A_T^2 k^2 V_a V_{\text{b.o.}}} - (1 + A_T)kV_a, \tag{5}$$

where

$$A_T \equiv \frac{1 - (\rho_{\text{b.o.}}/\rho_a)}{1 + (\rho_{\text{b.o.}}/\rho_a)}, \qquad V_{\text{b.o.}} = V_a \frac{\rho_a}{\rho_{\text{b.o.}}}, \tag{6a}$$

$$\frac{\rho_{\text{b.o.}}}{\rho_a} = \mu_0 (kL_0)^{1/v}, \qquad \mu_0 = \frac{(2/v)^{1/v}}{\Gamma(1+1/v)} + \frac{0.12}{v^2}, \tag{6b}$$

$\Gamma(x)$ is the gamma function and $V_{\text{b.o.}}$ is the velocity of the blowoff material at the distance $\sim\lambda$ from the ablation front. Observe that the cutoff wave number obtained by setting $\gamma = 0$ in Eq. (5) occurs at long wavelengths,[8]

$$k_c L_0 = \left[\frac{\mu_0(v)}{Fr}\right]^{v/(v-1)} \left\{1 + O\left[(kL_0)^{1/v}\right]\right\} \ll 1, \tag{7}$$

and short-wavelength modes are stable. As shown in Refs. 9 and 10, Eq. (5) can be accurately fitted by Eq. (4) for $v = 2.5$ and $0.1 < Fr < 5$, thus suggesting that the latter can be applied to ablation fronts with large Froude numbers.

When the Froude number is less than unity ($Fr \ll 1$), the analytic stability theory becomes more complicated and can be carried out only in the limits of $\in\, = kL_0 \ll 1$ and $\in\, \gg 1$. The analysis of Ref. 11 has shown that long-wavelength modes with wave numbers $\in\, \ll 1$ have a growth rate $\gamma \simeq \sqrt{A_T kg} - \beta kV_a$, where $1 < \beta < 2$ is a function of v, $\beta = \Gamma(1+2/v)/\Gamma^2(1+1/v)$. Short-wavelength modes ($kL_0 > 1$) are unstable, and the corresponding perturbations are mitigated by ablative convection, finite density gradient, and thermal smoothing. Their growth rate can be written as

$$\gamma = \sqrt{\alpha g/L_0 + c_0^2 k^4 L_0^2 V_a^2} - c_0 k^2 L_0 V_a$$

for $1 \ll kL_0 \ll Fr^{-1/3}$, and

$$\gamma = c_1 g/\left(V_a k^2 L_0^2\right) - c_2 kV_a$$

for the wave numbers near the cutoff ($k \approx k_c$). The parameters α and $c_{0–2}$ have lengthy expressions described in Ref. 11, and a complete summary of the growth-rate formulas is given in Table 1 of Ref. 11. The cutoff wave number k_c of ablation fronts with small Froude numbers occurs at short wavelengths and scales as $k_c L_0 \sim Fr^{-1/3} \gg 1$.

The growth-rate formulas obtained in Ref. 11 for small Froude numbers and short/long wavelengths can be combined with the formula (5) for large Froude numbers into a single expression that reproduces the analytic results in the appropriate limits ($Fr \ll 1$, $Fr \gg 1$, $\in\, \ll 1$, $\in\, \gg 1$). According to

Ref. 11, the asymptotic formula can be written in the following form:

$$\gamma = \sqrt{\hat{A}_T kg + \delta^2 k^4 L_0^2 V_a^2 + \left(\omega^2 - \frac{1}{\xi_l}\right)k^2 V_a^2}$$
$$- \delta k^2 L_0 V_a - \hat{\beta} k V_a, \tag{8a}$$

where

$$\hat{A}_T = \frac{\xi_h - \xi_l}{\xi_h + \xi_l}, \qquad \xi_h = \left(1 + K_1 e^{-\frac{K_3}{\epsilon}}\right)^{-1}, \tag{8b}$$

$$\xi_l = \mu_0 \left(\frac{1}{\epsilon} + K_2\right)^{-\frac{1}{\nu}},$$

$$\hat{\beta} = \omega \frac{1 + T_1 \epsilon}{1 + T_2 \epsilon}, \qquad T_1 = \frac{\beta_0 - \beta_1}{\beta_2 \beta_0}, \tag{8c}$$

$$T_2 = \frac{\beta_0 - \beta_1}{\beta_2 \beta_1},$$

$$\omega = \beta_0 \frac{1 + \left(1 + \hat{A}_T\right)/\beta_0 \sinh(Fr)}{1 + \sinh(Fr)}, \tag{8d}$$

$$\beta_0 = \frac{\Gamma\left(1 + \frac{2}{\nu + 0.1/\nu^4}\right)}{\Gamma^2\left(1 + \frac{1}{\nu + 0.1/\nu^4}\right)},$$

$$\beta_1 = \frac{1}{\xi_0 \sqrt{5}}, \qquad \beta_2 = B + \frac{\beta_0^2 + \beta_1^2}{2\delta\beta_1} - \frac{1 + K_1}{2\delta\beta_1}, \tag{8e}$$

$$\delta = \frac{1}{2\Upsilon}\left[K_1 A + \frac{1}{\nu K_2}\right.$$
$$\left. \times \sqrt{\left(\frac{1}{\nu K_2} + K_1 A\right)^2 - 4K_1\beta_1\Upsilon - \frac{1 + K_1\nu}{\nu^2 K_2^2}}\right], \tag{8f}$$

$$\Upsilon = \frac{25}{8} \frac{\xi_0^{2\nu+1}}{2\nu + 3}, \qquad K_2 = \left[(1 + K_1)\mu_0\right]^\nu, \tag{8g}$$

$$K_1 = \frac{1}{\xi_0} - 1,$$

$$K_3 = \frac{1 + K_1}{K_1}\left(2\delta\Upsilon - \frac{1}{\nu K_2}\right), \qquad \mu_0 = \frac{(2/\nu)^{1/\nu}}{\Gamma\left(1 + \frac{1}{\nu}\right)} + \frac{0.12}{\nu^2}, \tag{8h}$$

$$\xi_0 = \frac{2\nu + 2}{2\nu + 3},$$

$$A = \frac{\sqrt{5}}{4} \frac{\xi_0^{\nu-1}}{(2\nu + 3)^2}$$
$$\times \left[\sqrt{\frac{2}{5}\xi_0}\left(12\nu^2 + 25\nu + 18\right) + \frac{\nu + 2}{2\nu + 3}\left(8\nu^2 + 20\nu + 17\right)\right], \tag{8i}$$

$$B = \frac{\sqrt{5}}{4} \frac{\xi_0^{\nu-1}}{(2\nu + 3)^2}$$
$$\times \left[\sqrt{\frac{2}{5}\xi_0}\left(8\nu^2 + 25\nu + 12\right) - \frac{8\nu^3 + 16\nu^2 + 7\nu + 4}{2\nu + 3}\right]. \tag{8j}$$

A detailed comparison of the growth rates obtained by using Eq. (8) and the numerical solutions of the conservation equations has demonstrated a remarkable agreement over a wide range of values for Fr, ν, and ϵ (see Ref. 11).

Despite its lengthy expression, the asymptotic formula can be easily computed once the Froude number Fr, the length L_0, the acceleration g, the ablation velocity V_a, and the power index for thermal conduction ν are known. The main difficulty in using Eq. (8) lies in the determination of the equilibrium parameters whose values are strongly dependent on the dominant energy transport mechanism. In this article, we describe a simple procedure to be used in conjunction with existing one-dimensional hydrodynamic codes to determine Fr, L_0, g, V_a,

and v. In addition, we apply this procedure to accelerated flat foils commonly used in ICF experiments and determine the unstable spectrum using Eq. (8). We also compare the analytic growth rates with the results of two-dimensional simulations obtained using the code *ORCHID*.[19] Numerical fits of Eq. (8) are also studied for different ablators, and simplified formulas are generated for a fast growth-rate estimate. It is the aim of this article to simplify the theoretical result of Betti *et al.* (Refs. 8–11) to make it useful to ICF target design.

Equilibrium Parameters

One-dimensional simulations are commonly used in ICF target design, and several 1-D codes describing laser-accelerated targets are available at universities and national laboratories. Among them, the most frequently used are the codes *LILAC*,[20] *HYADES*,[21] *LASNEX*,[22] etc. In this article, the authors have extensively used the code *LILAC*, a 1-D Lagrangian code including laser absorption, classical flux-limited thermal transport, and multigroup radiation diffusive transport. The equation-of-state package available in *LILAC* includes the ideal gas, Thomas–Fermi, and SESAME tables.

The analytic stability analyses are usually based on a single-temperature (or one-group) diffusive model for the heat transport, i.e., the heat flux is proportional to the temperature gradient, and the thermal conductivity follows a power law of the temperature, $\kappa = \kappa_a (T/T_a)^v$, where κ_a, T_a are the thermal conductivity and temperature calculated at the peak density, and v is the power index. These simplifications make the problem solvable with analytic techniques.[8–12,14] If the radiated energy is negligible (low-Z materials, such as DT), the energy is transported mainly by electronic heat conduction. In this case, the power index $v = 2.5$ (as given by Spitzer[23]) and $L_0 = (\gamma_h - 1)/\gamma_h A \kappa_a /(\rho_a V_a)$, where γ_h is the ratio of the specific heats, $A = m_i /(1 + Z)$ is the average particle mass, ρ_a is the maximum density, and V_a is the ablation velocity, respectively (see Ref. 8). However, if a significant amount of energy is present in the radiation field, then an accurate estimate of the energy transport requires the use of multigroup radiation transport models. In such models, the radiation energy spectrum is divided into several groups. Each group is described by a radiation temperature obeying an energy diffusion equation. Because of the complexity of such models, an analytic stability analysis would be intractable. For such reason, the analytic theories are based on a single-group model (one temperature). However, if the one-group diffusive transport model is used in the stability analysis, then one should at least make sure that such a model reproduces the one-dimensional hydrodynamic profiles obtained using the multigroup

model. In other words, one should fit the multigroup hydro-profiles with the one-group profiles by properly selecting the value of v and L_0. This is an essential requirement for the stability analysis, assuring that the linearization is performed about the right equilibrium. Of course, there is no guarantee that the two-dimensional effects are correctly included in the one-group model, even though the one-dimensional profiles are correctly reproduced. However, the RT is mainly a hydro-dynamic instability, and one could hope that if the 1-D hydro-dynamic profiles are correctly included, then the 2-D/3-D stability analysis would be independent of the heat transport model. This speculation could be verified *a posteriori* by comparing the analytic results with 2-D simulations including multigroup radiation transport.

In summary, the analytic analysis is based on the one-group subsonic diffusive transport model (or isobaric model). The parameters v, Fr, and L_0 of such a model are determined by fitting the analytic hydro-profiles with those obtained from 1-D simulations including multigroup radiation transport. The results of the analytic stability theory are then compared with the full 2-D simulations including multigroup radiation transport.

As shown in Ref. 6, the density profile of subsonic ablation fronts, described by the one-temperature diffusive transport model, obeys the following first-order differential equation:

$$d\xi/dy = -\xi^{v+1}(1-\xi)/L_0, \qquad (9)$$

where ξ is the density normalized to its peak value, $\xi = \rho/\rho_a$, and v is the power index for thermal conduction. The equilibrium pressure is determined by the momentum-conservation equation $d(p + \rho U^2)/dy = \rho g$ and the mass conservation equation $[d(\rho U)/dy = 0]$, which can be rewritten in the following dimensionless form:

$$\frac{1}{\Pi_a} \frac{d\Pi}{dy} = \xi^2 \frac{d\xi}{dy} + \frac{\xi}{Fr\,L_0}, \qquad \xi U(y) = V_a, \qquad (10)$$

where $\Pi = p/p_a$, $\Pi_a = V_a/\sqrt{p_a/\rho_a}$ is the normalized ablation velocity, and p_a is the pressure at the location of the peak density ρ_a. Observe that Eqs. (9) and (10) for the unknowns ξ and Π depend on the four parameters Π_a, Fr, L_0, and v. Keeping in mind that our goal is to reproduce the hydro-profiles of the 1-D simulations, we determine these parameters by fitting the analytic hydro-profiles with the numerical ones. Let's define with $\xi_s = \rho/\rho_a$ and $\Pi_s = p/p_a$ the normalized simulated

density and pressure profiles. If the predictions of the one-group model were exact, then the simulated profiles would represent an exact solution of Eqs. (9) and (10); however, this is not the case, and replacing ξ with ξ_s in Eq. (9) leads to an error. For convenience, we take the logarithm of Eq. (9) and define the error as

$$\mathrm{er} = (\nu + 1)\ln \xi_s - \ln L_0 - \ln\left(-\frac{d\xi_s}{dy}\frac{1}{1-\xi_s}\right). \qquad (11)$$

Observe that $\mathrm{er} = 0$ if $\xi_s = \xi$. In order to reproduce the simulated profiles over the entire ablation front, it is useful to minimize the integrated quadratic error (δ) defined as

$$\delta(\nu, L_0) \equiv$$

$$\int_{\xi_{\min}}^{\xi_{\max}} \left[(\nu+1)\ln\xi_s - \ln L_0 - \ln\left(-\frac{d\xi_s}{dy}\frac{1}{1-\xi_s}\right)\right]^2 d\xi_s, \qquad (12)$$

where $\xi_{\min}$, $\xi_{\max}$ are the minimum and the maximum values of the density of the fitting region defining the extension of the ablation front ($\xi_{\min} = 0.01$ and $\xi_{\max} = 0.99$ are two possible values). The minimization of δ is obtained by setting to zero the partial derivatives with respect to ν and L_0:

$$\frac{\partial\delta}{\partial L_0} = \frac{\partial\delta}{\partial\nu} = 0. \qquad (13)$$

Substituting Eq. (12) into Eq. (13) leads to the following estimates of L_0 and ν:

$$\nu = \frac{c_1 a_1 - c_2 b_1}{a_1^2 - a_2 b_1} - 1, \qquad L_0 = \exp\left(\frac{+a_2 c_1 - a_1 c_2}{a_1^2 - a_2 b_1}\right), \qquad (14)$$

where

$$a_1 = [\![\xi(\ln\xi - 1)]\!],$$

$$\qquad (15a)$$

$$a_2 = [\![\xi(\ln\xi - 1)^2 + \xi]\!], \qquad b_1 = [\![\xi]\!],$$

$$c_1 = \int_{y(\xi_{\min})}^{y(\xi_{\max})} \ln\left[-\frac{d\xi_s}{dy}\frac{1}{1-\xi_s}\right]\frac{d\xi_s}{dy}\,dy, \qquad (15b)$$

$$c_2 = \int_{y(\xi_{\min})}^{y(\xi_{\max})} \ln\xi_s \ln\left[-\frac{d\xi_s}{dy}\frac{1}{1-\xi_s}\right]\frac{d\xi_s}{dy}\,dy, \qquad (15c)$$

and $[\![H(\xi)]\!] = H(\xi_{\max}) - H(\xi_{\min})$. In the same fashion, the Froude number and dimensionless ablation velocity Π_a can be determined by minimizing the integrated quadratic error η in the momentum conservation equation

$$\eta(Fr, \Pi_a)$$

$$= \int_{y(\xi_{\min})}^{y(\xi_{\max})} \left(\frac{1}{\Pi_a^2}\frac{d\Pi_s}{dy} - \frac{1}{\xi_s^2}\frac{d\xi_s}{dy} - \frac{\xi_s}{FrL_0}\right)^2 dy, \qquad (16)$$

where $\Pi_s = p_s/p_a$ is the simulated normalized pressure profile. After some straightforward algebra, the minimization with respect to Π_a and Fr yields

$$Fr = \frac{a_3 b_4 + b_3^2}{b_3 c_3 + a_3 c_4}\frac{1}{L_0}, \qquad \Pi_a^2 = \frac{a_3 b_4 + b_3^2}{c_3 b_4 - c_4 b_3}, \qquad (17a)$$

where

$$a_3 = \int_{y(\xi_{\min})}^{y(\xi_{\max})} \left(\frac{d\Pi_s}{dy}\right)^2 dy,$$

$$\qquad (17b)$$

$$b_3 = -\int_{y(\xi_{\min})}^{y(\xi_{\max})} \xi_s \frac{d\Pi_s}{dy}\,dy,$$

$$b_4 = -\int_{y(\xi_{\min})}^{y(\xi_{\max})} \xi_s^2\,dy, \qquad c_3 = \int_{y(\xi_{\min})}^{y(\xi_{\max})} \frac{1}{\xi_s^2}\frac{d\Pi_s}{dy}\frac{d\xi_s}{dy}\,dy,$$

$$\qquad (17c)$$

$$c_4 = \ln\frac{\xi_{\max}}{\xi_{\min}}.$$

The integration limits $y(\xi_{\min})$, $y(\xi_{\max})$ represent the location of the points with density $\xi_{\min}$ and $\xi_{\max}$, respectively. Using the peak density ρ_a and the pressure at the location of the peak

density p_a, the acceleration and ablation velocity can be easily determined from Eqs. (14) and (17):

$$V_a = \Pi_a \sqrt{\frac{p_a}{\rho_a}}, \qquad g = \frac{V_a^2}{L_0} \frac{1}{Fr}. \qquad (18)$$

This technique has been tested on the hydrodynamic profiles obtained using the code *LILAC*. We consider a planar CH foil of thickness $d = 18$ μm irradiated by a 0.35-μm-wavelength laser of 50-TW/cm^2 intensity with a 1-ns linear ramp. The pulse duration is 3 ns. The profiles obtained from the simulation are slowly varying in time. For the test, we consider the profiles at time $t = 2$ ns and substitute the simulated density and pressure into Eqs. (14), (17), and (18) and obtain $v = 0.7$, $L_0 = 0.24$ μm, $Fr = 0.032$, $g = 36$ μm/ns^2, and $V_a = 0.54$ μm/ns. Then, using these values, we solve Eqs. (9) and (10) to determine the analytic density and pressure profiles. Figure 73.27 shows the simulated and the analytic profiles for the CH target. The excellent agreement between the profiles shows the accuracy of the fitting procedure described above. In Fig. 73.28, the fitting parameters v, L_0, and Fr are plotted as functions of time, and the dashed lines represent the corresponding average values. It is important to notice that the power index for thermal conduction to be used in the one-group model ($v = 0.7$) is well below the Spitzer[23] ($v = 2.5$) or the Zeldovich[24] value ($v \simeq 6.5$), thus showing the importance of the multigroup treatment of the radiation transport in plastic targets.

Lower-Z materials such as solid DT are a good test of the fitting procedure because they are expected to produce a very low level of radiation and to approximately follow the Spitzer model with $v \approx 2.5$. We have considered a planar DT foil of

thickness $d = 120$ μm irradiated by the pulse described above. Substituting the simulated profiles into Eqs. (9) and (10) yields $v = 2$, $L_0 = 0.03$ μm, and $Fr = 5$. This result indicates that radiation transport has a small effect in cryogenic DT targets.

Tables 73.I and 73.II show the time-averaged values of Fr, v, L_0, and V_a for several plastic (CH) and DT targets of different thicknesses (Th) and laser intensities (I). It is important to observe that plastic targets have smooth density profiles (large density-gradient scale length), low ablation velocity, $v < 1$, and small Froude numbers while solid-DT targets have sharp profiles, large ablation velocity, $v \approx 2$, and large Froude numbers.

TC4538
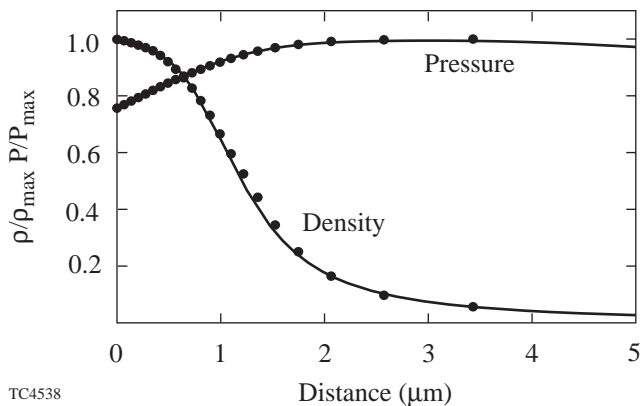
Figure 73.27
Normalized density and pressure profiles obtained by using isobaric model (solid lines) and 1-D numerical simulation (dots).
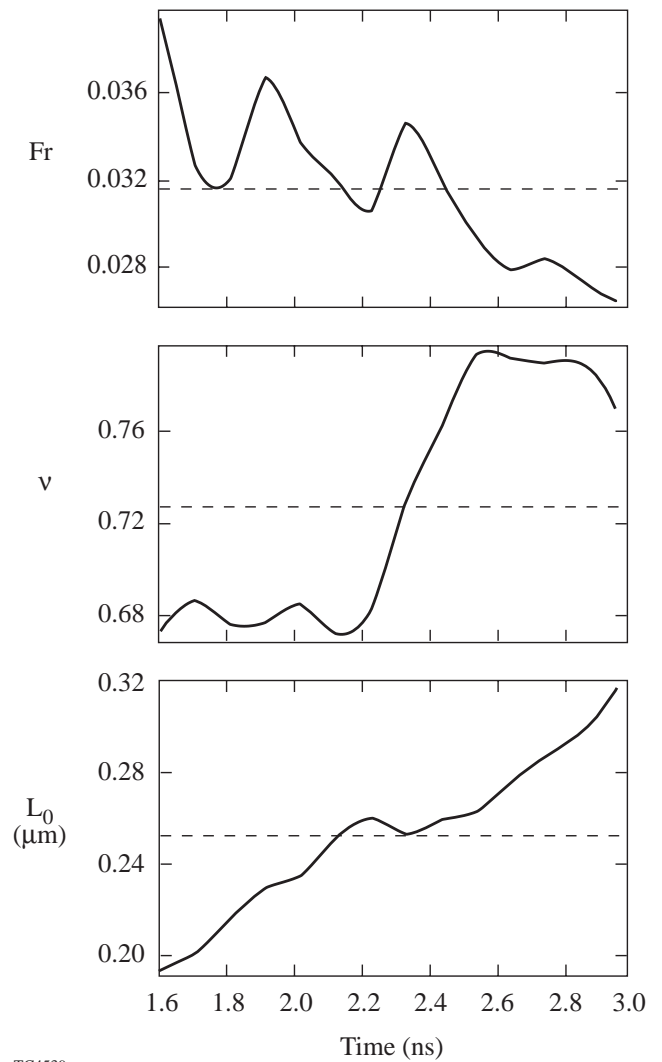

TC4539

Figure 73.28
Temporal evolution (solid lines) and average values (dashed lines) of the Froude number Fr, power index for thermal conduction v, and the characteristic thickness of ablation front L_0 for a CH target.

Growth Rates

1. Comparison with Numerical Results

Once the equilibrium parameters are calculated, Eq. (8) can be used to determine the growth rates. As discussed in the previous section, there is no guarantee that the analytic stability analysis using the one-temperature model would reproduce the results of the 2-D simulations using the multigroup radiation diffusion treatment even though the 1-D simulated and analytic hydrodynamic profiles are identical. It is necessary to validate the formula by comparing the analytic and the numerical growth rates.

As a first test of the analytic theory, we compare the analytic growth rates with Takabe's formula.[3] The latter has been derived by fitting the numerical solution of the exact, linearized, single-fluid conservation equations including Spitzer conductivity and a finite Mach number. This test is useful because it validates the assumption of subsonic flow and the simplification leading to the isobaric model.[5] Takabe's formula can be written in the following dimensionless form:[3]

$$\hat{\gamma} = \frac{\gamma}{\gamma_{cl}} = \alpha_T - \beta_T X, \tag{19}$$

where $\gamma_{cl} = \sqrt{kg}$ is the classical growth rate, $X = \sqrt{kV_a^2/g}$, $\alpha_T \simeq 0.9$, and $\beta_T \simeq 3.1$. Similarly, Eq. (8) can also be rewritten in dimensionless form:

$$\hat{\gamma} = \sqrt{\hat{A}_T + \delta^2 \frac{X^6}{Fr^2} + \left(\omega^2 - \frac{1}{\xi_l}\right)X^2} - \delta \frac{X^3}{Fr} - \hat{\beta}X. \tag{20}$$

Table 73.I: CH targets.

Th (μm)	I (TW/cm²)	$\langle Fr \rangle$	$\langle v \rangle$	$\langle L_0 \rangle$ (μm)	$\langle L_m \rangle$ (μm)	$\langle V_a \rangle$ (μm/ns)	$\langle g \rangle$ (μm/ns²)	Growth Rate [fit of Eq. (8)]
10	50	0.03	0.8	0.2	0.7	0.8	95	$1.01\sqrt{\dfrac{kg}{1+k\,L_m}} - 1.8\,kV_a$
18	50	0.03	0.8	0.3	1.0	0.6	50	$1.01\sqrt{\dfrac{kg}{1+k\,L_m}} - 1.8\,kV_a$
20	100	0.04	0.9	0.3	1.1	0.9	76	$0.99\sqrt{\dfrac{kg}{1+k\,L_m}} - 1.7\,kV_a$
20	240*	0.05	0.9	0.2	0.7	1.3	130	$0.97\sqrt{\dfrac{kg}{1+k\,L_m}} - 1.6\,kV_a$
25	240*	0.05	0.9	0.2	0.7	1.2	123	$0.98\sqrt{\dfrac{kg}{1+k\,L_m}} - 1.6\,kV_a$

*Linear-rise laser pulse

Table 73.II: DT targets.

Th (μm)	I (TW/cm²)	$\langle Fr \rangle$	$\langle v \rangle$	$\langle L_0 \rangle$ (μm)	$\langle L_m \rangle$ (μm)	$\langle V_a \rangle$ (μm/ns)	$\langle g \rangle$ (μm/ns²)	Growth Rate [fit of Eq. (8)]
100	50	4.1	2.0	0.02	0.13	2.8	97	$0.94\sqrt{kg} - 2.6\,kV_a$
190	50	3.8	2.0	0.03	0.20	2.7	60	$0.94\sqrt{kg} - 2.6\,kV_a$
190	100	4.0	2.1	0.07	0.49	4.6	77	$0.94\sqrt{kg} - 2.6\,kV_a$

The growth rates calculated using Eq. (19) and Eq. (20) for ν = 2.5 and different Froude numbers are shown in Fig. 73.29. Observe that the two formulas approximately agree for Froude numbers between 0.1 and 5. This result is not surprising as Takabe's formula has been derived using Spitzer conductivity leading to sharp profiles (small L_0 and therefore relatively large Froude numbers). We conclude that the RT growth rate in low-Z materials with $Fr > 0.1$, such as solid DT, is well described by Takabe's formula over a wide range of Fr ($0.1 < Fr < 5$). For small Froude numbers or different values of ν, Takabe's formula doesn't provide an accurate estimate of the growth rate so Eq. (8) or its fitting formulas must be used.

When the ablation velocity is small or the density profile is smooth—as in the case of large radiation energy transport—we expect the Froude number to decrease. As shown in Fig. 73.29, Takabe's formula and Eq. (8) yield very different results for this case. In addition, radiative transport causes the deviation of the power index ν from the Spitzer value requiring a more general formula than Takabe's. For such targets, Eq. (8) can be compared only with the results of full 2-D simulations including a multigroup radiation-transport model. We consider the same 18-μm plastic target described in the previous section, and we simulate it with the code *ORCHID*. We then calculate the parameters ν, Fr, L_0, and V_a to be used in Eq. (8) by substituting *ORCHID* density and pressure profiles into Eqs. (14), (17), and (18) and find $Fr = 0.043$, $L_0 = 0.24$ μm, $V_a = 0.66$ μm/ns, $\nu = 0.96$, and $g = 43$ μm/ns^2. In Fig. 73.30, the growth rates obtained using *ORCHID* (dots) are compared with Eq. (8) (solid line), Takabe's (dot–dashed line), and

modified Takabe's (dashed line) formulas. The latter is the Takabe's formula including the stabilizing effects of finite density-gradient scale length in a heuristic fashion,

$$\gamma_{\text{m.T.}} = \alpha_T \sqrt{\frac{kg}{1 + kL_m}} - \beta_T kV_a, \tag{21}$$

where L_m is the minimum density-gradient scale length, L_m = 0.93 μm. Observe that Takabe's and modified Takabe's formulas fail to reproduce the simulation results in the short-wavelength regime. Instead, the growth rates obtained with Eq. (8) are in excellent agreement with the simulated ones over the entire unstable spectrum.

Furthermore, we study different pulse shapes and different target materials. We consider a 20-μm-thick CH target irradiated by a square pulse with an intensity of 200 TW/cm^2 and 100-ps linear rise time. According to the *ORCHID* simulations, the hydrodynamic profiles reach a steady state after 1.3 ns. The growth rates of 30-μm and 15-μm wavelength perturbations are determined from the 2-D simulations yielding $\gamma^{\text{sim}}(15\,\mu\text{m})$ = 4.9 ns^{-1} and $\gamma^{\text{sim}}(30\,\mu\text{m})$ = 4.1 ns^{-1}. Using the *ORCHID* hydrodynamic profiles and Eqs. (14), (17), and (18), we estimate the relevant hydrodynamic parameters $\nu = 1.2$, $L_0 = 0.22$ μm, $V_a = 2.0$ μm/ns, $Fr = 0.12$, and $g = 144$ μm/ns^2. Substituting such parameters into the asymptotic formula [Eq. (8)] yields the theoretical growth rates $\gamma^{\text{th}}(15\,\mu\text{m})$ = 4.9 ns^{-1} and $\gamma^{\text{th}}(30\,\mu\text{m})$ = 4.06 ns^{-1}, reproducing the simulation results.
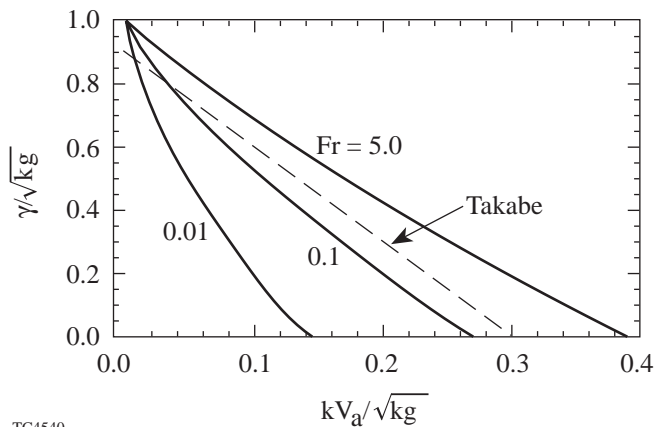
TC4540

Figure 73.29
Normalized growth rate $\left(\gamma/\sqrt{kg}\right)$ versus normalized wave number $\left(\sqrt{kV_a^2/g}\right)$ calculated using the Takabe's formula (dashed line) and Eq. (8) (solid line) for different values of the Froude number and $\nu = 2.5$.
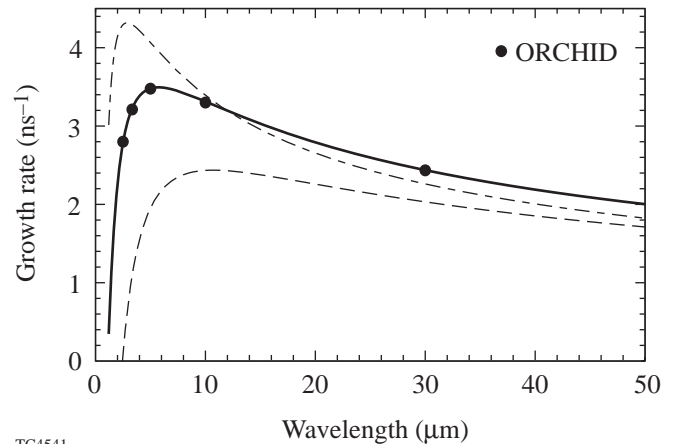
TC4541

Figure 73.30
Unstable spectrum calculated using the analytic formula (8) (solid line) compared with the numerical results (dots) of 2-D hydrocode *ORCHID*, Takabe's formula (dot-dashed line) and modified Takabe's formula (dashed line).

Next, we simulate the evolution of 6-μm-wavelength surface perturbation on a 20-μm-thick beryllium foil irradiated by a square pulse with an intensity of 50 TW/cm^2 and 100-ps linear rise time. The steady state is reached after 1.5 ns and the *ORCHID* simulation yields the mode growth rate $\gamma^{\text{sim}} = 2.27$ ns^{-1}. The simulated and analytic hydrodynamic profiles match for $\nu = 0.63$, $L_0 = 0.36\ \mu m$, $V_a = 0.73\ \mu m/ns$, $Fr = 0.06$, and $g = 25\ \mu m/ns^2$, thus yielding the theoretical growth rate $\gamma^{\text{th}} = 2.28$ ns^{-1} in good agreement with the numerical simulations.

These tests are a clear indication that Eq. (8) can be used to determine the RT growth rates for ablation fronts with large/small Froude numbers and short-/long-wavelength perturbations.

2. Fitting Formula for the Growth Rate

Although Eq. (8) provides an accurate estimate of the ablative RT growth rates, its expression is too complicated for practical applications. Without a doubt, a simplification of Eq. (8) would greatly help the target designers in the choice of the ablator material and the implementation of the RT mixing models. For this purpose, we simplify Eq. (8) using two well-known fitting formulas:

$$\gamma_1 = \alpha_1(Fr, \nu)\sqrt{kg} - \beta_1(Fr, \nu)kV_a, \qquad (22)$$

$$\gamma_2 = \alpha_2(Fr, \nu)\sqrt{\frac{kg}{1 + kL_m}} - \beta_2(Fr, \nu)kV_a, \qquad (23)$$

where $L_m = L_0(\nu + 1)^{\nu+1}/\nu^\nu$ is the minimum density-gradient scale length, and the α's and β's are functions of Fr and ν. It turns out that Eq. (22) is particularly accurate in fitting the large Froude number results, while Eq. (23) is suitable for low Froude numbers. This is not surprising as ablation fronts with small Froude numbers are unstable to modes with wavelengths smaller than the density-gradient scale length whose growth is strongly affected by the finite kL_m.

The calculation of the coefficients α_1, β_1 and α_2, β_2 is carried out using the standard fitting procedures of the Mathematica software package.[25] We define a range of interest for the mode wavelength from the cutoff λ_c to about 200 times the cutoff wavelength $\lambda_{\max} \approx 200\ \lambda_c$ (the parameters α and β have shown little sensitivity to the value of $\lambda_{\max}$). The α's and β's are determined by fitting the growth rate γ obtained using Eq. (8) with the formulas (22) and (23) over the wavelength range $\lambda_c < \lambda < \lambda_{\max}$. Figures 73.31 and 73.32 show

the value of α, β for different Fr and ν. The solid section of the curves represents the region of optimum fit, i.e., the region where each formula fits the data at its best. According to the value of Fr and ν, one should use the formula corresponding to a solid curve.

As an example, we consider the plastic target used in the *ORCHID* simulations described in the previous section. The values $Fr = 0.043$ and $\nu = 0.96$ are obtained by processing the *ORCHID* hydro-profiles with the procedure described in the **Equilibrium Parameters** section. Using Fig. 73.32, we determine the optimum fit by using γ_2 with $\alpha_2 = 0.98$ and $\beta_2 = 1.64$. Figure 73.33 shows a plot of the unstable spectrum obtained using Eq. (8) (solid line) and the fitting formula γ_2 (dashed line). The excellent agreement between the two curves indicates that the fitting formula represents a good approximation of Eq. (8).

TC4542
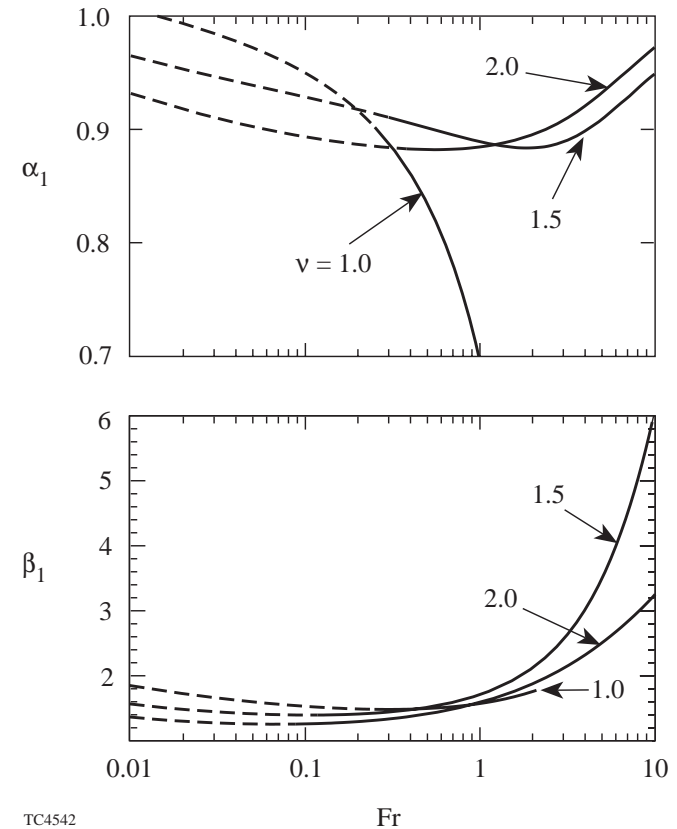
Figure 73.31
Plot of coefficients α_1, β_1 of the fitting formula (22) versus Froude number for different values of the power index ν. Solid line represents the regions of the best fit of the analytical formula (8) with Eq. (22).

We have determined the optimum fit for several plastic and solid-DT targets commonly used in direct-drive ICF experiments. Table 73.I shows the results of the fitting procedure described above for different laser pulses and plastic target thicknesses. It appears that over a wide range of thicknesses and laser powers, the growth rate of the RT instability for directly driven CH targets can be approximated by

$$\gamma_{\mathrm{CH}} \approx 0.98 \sqrt{\frac{kg}{1+kL_m}} - 1.7 \; kV_a, \quad (24)$$

where $0.6 < L_m < 1 \; \mu\mathrm{m}$. The same formula has been derived for the aluminum-coated CH and beryllium targets. The corresponding time-averaged values of Fr, ν, L_0, g, and V_a are shown in Tables 73.III and 73.IV, respectively. The growth rate for cryogenic DT targets is better represented by the fit γ_1, and Table 73.II shows the optimum fit for different flat targets driven by a 1-ns linear ramp followed by a flat-top pulse. These

results indicate that the growth rate of solid-DT targets is well approximated by a Takabe-like formula

$$\gamma_{\mathrm{DT}} \approx 0.94 \sqrt{kg} - 2.7 \; kV_a. \quad (25)$$

The RT growth rate for different ablator materials can be determined in the same fashion by using 1-D hydro-simulations to reproduce the density and pressure profiles; Eqs. (14), (17), and (18) to calculate the equilibrium parameters; and Figs. 73.31 and 73.32 to generate the growth-rate formulas.

It is very important that the 1-D hydrodynamic analytic profiles be carefully matched with the simulation results when determining the relevant equilibrium parameters. Even though the analytic theory yields satisfactory results for DT, CH, and Be targets, it might fail to reproduce the profiles of other materials. For instance, the hydrodynamic profiles of plastic targets with high-Z dopants are not well reproduced by the single temperature model, and Eq. (8) cannot be applied to determine the RT growth rate. The study of the RT instability in such targets is currently under investigation.

An interesting result of the analytic theory concerns those equilibria with $\nu \simeq 1$ and $Fr > 2$. Figure 73.31 shows that α_1 decreases dramatically with increasing Froude numbers. This result is not surprising as the same conclusion can be reached using the results of the self-consistent stability analysis of Ref. 9 reported in Eq. (5). The growth-rate formula (5) yields zero growth rate for equilibria with $\nu = 1$ and $Fr > 2$ when the
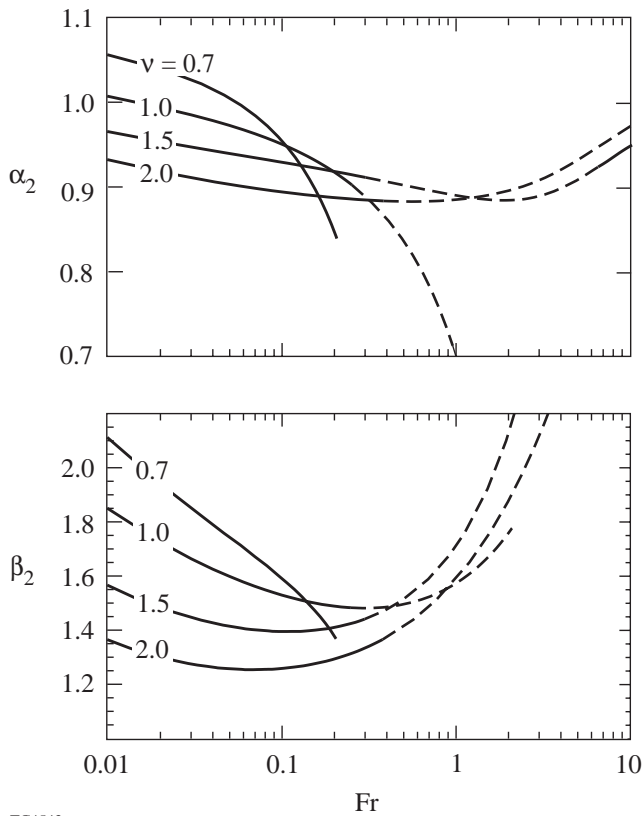
TC4543

Figure 73.32
Plot of coefficients α_2, β_2 of the fitting formula (23) versus Froude number for different values of the power index ν. Solid line represents the regions of the best fit of the analytical formula (8) with Eq. (23).
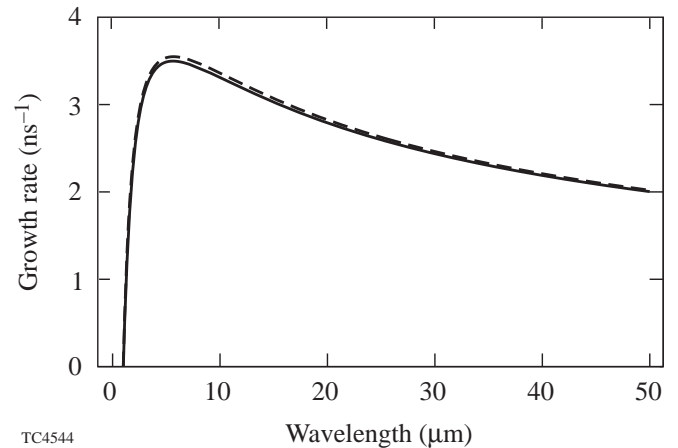
TC4544

Figure 73.33
Unstable spectrum of the target described in the **Equilibrium Parameters** section calculated using the analytic formula (8) (solid line) and the fitting formula (23) (dashed line).

Table 73.III: Be targets.

Th (μm)	I (TW/cm^2)	$\langle Fr \rangle$	$\langle v \rangle$	$\langle L_0 \rangle$ (μm)	$\langle L_m \rangle$ (μm)	$\langle V_a \rangle$ (μm/ns)	$\langle g \rangle$ (μm/ns^2)	Growth Rate [fit of Eq. (8)]
16	50	0.05	0.7	0.2	0.6	0.6	40	$1.00\sqrt{\dfrac{kg}{1+k\,L_m}} - 1.7\,kV_a$
16	100	0.06	0.7	0.2	0.6	0.8	60	$0.99\sqrt{\dfrac{kg}{1+k\,L_m}} - 1.7\,kV_a$
32	100	0.06	0.6	0.4	1.2	0.8	28	$1.00\sqrt{\dfrac{kg}{1+k\,L_m}} - 1.7\,kV_a$
16	240*	0.10	0.8	0.1	0.4	1.1	28	$0.95\sqrt{\dfrac{kg}{1+k\,L_m}} - 1.7\,kV_a$

*Linear-rise laser pulse

Table 73.IV: CH targets with aluminum coating.

Th (μm)	I (TW/cm^2)	$\langle Fr \rangle$	$\langle v \rangle$	$\langle L_0 \rangle$ (μm)	$\langle L_m \rangle$ (μm)	$\langle V_a \rangle$ (μm/ns)	$\langle g \rangle$ (μm/ns^2)	Growth Rate [fit of Eq. (8)]
20+0.5	100	0.07	0.9	0.7	2.6	1.9	72	$0.97\sqrt{\dfrac{kg}{1+k\,L_m}} - 1.7\,kV_a$
20+1.0	100	0.08	0.7	1.6	5.0	2.8	63	$0.98\sqrt{\dfrac{kg}{1+k\,L_m}} - 1.7\,kV_a$

second term in the square root $-A_T^2 k^2 V_a V_{\text{b.o.}}$ (caused by overpressure of the blowoff region with respect to the overdense region) is larger than the instability-drive term $A_T kg$ for any wave number. This result has also been confirmed by solving the system (2)–(4) of Ref. 9 using an initial value code and is also in agreement with the numerical results of Kull (see Ref. 6). In addition, the numerical results seem to indicate that such a stabilization occurs for any $v \leq 1$. In conclusion, hydrodynamic profiles with $v \leq 1$ and $Fr > 2$ are RT stable for all wavelengths.

Conclusions

The growth rate of the ablative Rayleigh–Taylor instability is calculated using the analytic theory of Goncharov *et al.* (Ref. 11) and the output of one-dimensional simulations of laser-accelerated targets. The simulated density and pressure profiles are used to determine the equilibrium parameters Fr, V_a, g, v, and L_0 via a newly developed fitting procedure. Those parameters are then substituted into the self-consistent growth-rate formula of Goncharov *et al.* (Ref. 11). The accuracy of such a procedure has been tested by comparing the analytic growth rates for a plastic target with the ones obtained using two-dimensional simulations. This theory suggests that Takabe's formula represents a good approximation of the growth rates for only relatively large Froude numbers ($0.1 < Fr < 5$) and electronic heat conduction ($v \approx 2.5$) but fails for small Froude numbers and radiative materials. The complicated asymptotic formula of Ref. 11, which is valid for arbitrary Froude numbers, has been simplified by using simple fits over a wide range of Froude numbers and power indices for thermal conduction. In addition, simple growth-rate formulas for solid DT, plastic (CH), and beryllium targets have been derived. Even though the analytic theory yields satisfactory results for DT, CH, and Be targets, it might not be adequate for other materials such as chlorinated plastic. The hydrodynamic profiles of plastic targets with high-Z dopants are not well reproduced by the single temperature model and Eq. (8) cannot be applied to determine the RT growth rate.

REFERENCES

1. S. E. Bodner, Phys. Rev. Lett. **33**, 761 (1974).

2. K. O. Mikaelian, Phys. Rev. A **42**, 4944 (1990).

3. H. Takabe *et al.*, Phys. Fluids **28**, 3676 (1985).

4. C. P. Verdon, R. L. McCrory, R. L. Morse, G. R. Baker, D. I. Meiron, and S. A. Orszag, Phys. Fluids **25**, 1653 (1982).

5. H. J. Kull and S. I. Anisimov, Phys. Fluids **29**, 2067 (1986).

6. H. J. Kull, Phys. Fluids B **1**, 170 (1989).

7. J. D. Kilkenny, S. G. Glendinning, S. W. Haan, B. A. Hammel, J. D. Lindl, D. Munro, B. A. Remington, S. V. Weber, J. P. Knauer, and C. P. Verdon, Phys. Plasmas **1**, 1379 (1994).

8. R. Betti, V. N. Goncharov, R. L. McCrory, and C. P. Verdon, Phys. Plasmas **2**, 3844 (1995).

9. V. N. Goncharov, R. Betti, R. L. McCrory, P. Sorotokin, and C. P. Verdon, Phys. Plasmas **3**, 1402 (1996).

10. R. Betti, V. N. Goncharov, R. L. McCrory, P. Sorotokin, and C. P. Verdon, Phys. Plasmas **3**, 2122 (1996).

11. V. N. Goncharov, R. Betti, R. L. McCrory, and C. P. Verdon, Phys. Plasmas **3**, 4665 (1996).

12. A. R. Piriz, J. Sanz, and L. F. Ibanez, Phys. Plasmas **4**, 1117 (1997).

13. S. Atzeni, Nucl. Fusion **36**, 69 (1996).

14. J. Sanz, Phys. Rev. E **53**, 4026 (1996).

15. J. H. Nuckolls *et al.*, Nature **239**, 139 (1972).

16. J. D. Lindl, Phys. Plasmas **2**, 3933 (1995).

17. Lord Rayleigh, in *Scientific Papers* (Cambridge University Press, Cambridge, England, 1900), Vol. II, pp. 200–207; G. Taylor, Proc. R. Soc. London Ser. A **201**, 192 (1950).

18. A. B. Bud'ko and M. A. Liberman, Phys. Fluids B **4**, 3499 (1992).

19. R. L. McCrory and C. P. Verdon, in *Computer Applications in Plasma Science and Engineering*, edited by A. T. Drobot (Springer-Verlag, New York, 1991).

20. J. Delettrez and E. B. Goldman, Laboratory for Laser Energetics Report No. 36, University of Rochester (1976).

21. J. T. Larsen and S. M. Lane, J. Quant. Spectrosc. Radiat. Transf. **51**, 179 (1994).

22. G. B. Zimmerman and W. L. Kruer, Comments Plasma Phys. Control. Fusion **2**, 51 (1975).

23. L. Spitzer, Jr. and R. Härm, Phys. Rev. **89**, 977 (1953).

24. Ya. B. Zel'dovich and Yu. P. Raizer, in *Physics of Shock Waves and High-Temperature Hydrodynamic Phenomena*, edited by W. D. Hayes and R. F. Probstein (Academic Press, New York, 1966), Vol. I, p. 152.

25. S. Wolfram, *The Mathematica Book*, 3rd ed. (Wolfram Media/ Cambridge University Press, 1996).

Three-Dimensional Analysis of the Power Transfer Between Crossed Laser Beams

The indirect-drive approach to inertial confinement fusion[1] involves laser beams that overlap as they enter the hohlraum. Because a power transfer between the beams affects the implosion symmetry adversely, it is important to understand the mechanisms that make such a power transfer possible.

The power transfer between crossed laser beams made possible by an ion-acoustic (sound) wave (grating) has been studied theoretically[2–5] and experimentally.[6,7] Previously,[4] we made a two-dimensional analysis of the power transfer between beams with top-hat intensity profiles in a homogeneous plasma. In this article we extend our previous analysis to include three dimensions and arbitrary intensity profiles.

The interaction geometry is illustrated in Fig. 73.34. Notice that the beam axes intersect at the origin. It was shown in Ref. 4 that the steady-state interaction of the beams is governed by

$$\partial_x A_1 = (i\alpha_1 - \beta_1)|A_2|^2 A_1 \,,$$
$$\partial_y A_2 = (i\alpha_2 + \beta_2)|A_1|^2 A_2 \,,$$

(1)

where the characteristic variables x and y measure distance in the propagation directions of beams 1 and 2, respectively. The beam amplitude $A_j = (u_j/c_s)(m_e/m_i)^{1/2}$ is the quiver velocity of electrons in the high-frequency electric field of beam j divided by a speed that is of the order of the electron thermal speed. The nonlinear coefficients

$$\alpha_j = \frac{\omega_e^2 \omega_s^2 (\omega_s^2 - \omega^2)}{2\omega_j v_j \left[(\omega_s^2 - \omega^2)^2 + 4 v_s^2 \omega^2\right]},$$

$$\beta_j = \frac{\omega_e^2 \omega v_s \omega}{\omega_j v_j \left[(\omega_s^2 - \omega^2)^2 + 4 v_s^2 \omega^2\right]},$$

(2)
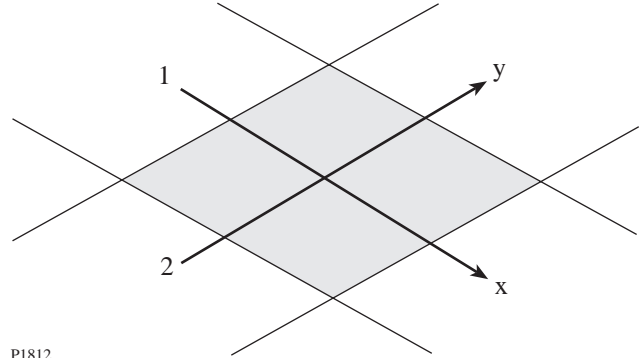
P1812

Figure 73.34
Geometry of the interaction of crossed laser beams. The characteristic coordinates x and y measure distance in the propagation directions of beams 1 and 2, respectively.

where ω_j is the frequency of beam j, v_j is the group speed of beam j, $\omega = \omega_1 - \omega_2$ is the difference between the beam frequencies, and $\omega_s = c_s|\mathbf{k}_1 - \mathbf{k}_2|$ and v_s are the sound frequency and damping rate, respectively. Since $|\omega| \ll \omega_1$, the differences between ω_1 and ω_2, and v_1 and v_2, can be neglected in Eqs. (2). Henceforth, the subscripts on the nonlinear coefficients will be omitted. These coefficients characterize the way in which the grating responds to the low-frequency ponderomotive force. Apart from a factor of $|A_1|^2$, at resonance β is the spatial growth rate of stimulated Brillouin scattering (SBS) in the strong-damping limit.

It follows from Eqs. (1) that the beam intensities $I_j = |A_j|^2$ satisfy the equations

$$\partial_x I_1 = -2\beta I_2 I_1 \,, \quad \partial_y I_2 = 2\beta I_1 I_2 \,.$$

(3)

The boundary conditions are

$$I_1(-\infty, y, z) = J_1(y, z), \quad I_2(x, -\infty, z) = J_2(x, z), \quad (4)$$

where $J_1(y,z)$ and $J_2(x,z)$ are the upstream intensity profiles of the beams.

It follows from Eqs. (3) that the beam evolution in any characteristic plane, labeled by the associated value of z, is independent of the beam evolution in the neighboring planes. Consequently, the method used in Ref. 4 to analyze the two-dimensional interaction of the beam applies, with minor modifications, to the three-dimensional interaction considered herein. This method was used by several authors[8–10] to study the interaction of two pulses in one spatial dimension and time.

It is convenient to define

$$P_1(x,y,z) = \int_{-\infty}^{y} I_1(x,y',z)\,dy',$$
$$P_2(x,y,z) = \int_{-\infty}^{x} I_2(x',y,z)\,dx'. \quad (5)$$

Physically, $P_1(x,\infty,z)$ is the power per unit height in the slice of beam 1 that is a distance x from the center the interaction region, and $P_2(\infty,y,z)$ is the power per unit height in the slice of beam 2 that is a distance y from the center of the interaction region. By combining Eqs. (3) and (5), one can show that

$$\partial_x P_1 = J_2\left[1 - \exp(2\beta P_1)\right]. \quad (6)$$

It follows from Eq. (6) that

$$2\beta P_1 = -\log\left\{1 - \exp(-\xi)\left[1 - \exp(-\eta)\right]\right\}, \quad (7)$$

where the distance variables

$$\xi = 2\beta\int_{-\infty}^{x} J_2(x',z)\,dx', \quad \eta = 2\beta\int_{-\infty}^{y} J_1(y',z)\,dy'. \quad (8)$$

It follows from Eq. (7), and the relations $I_1 = \partial_y P_1$ and $I_2 = J_2\exp(2\beta P_1)$, that

$$I_1 = \frac{J_1\exp(-\eta)}{\exp(\xi) - 1 + \exp(-\eta)},$$
$$I_2 = \frac{J_2\exp(\xi)}{\exp(\xi) - 1 + \exp(-\eta)}. \quad (9)$$

By combining Eqs. (3) and (5), one can also show that

$$2\beta P_2 = \log\left\{1 + \exp(\eta)\left[\exp(\xi) - 1\right]\right\}. \quad (10)$$

Equation (10) and the relations $I_2 = \partial_x P_2$ and $I_1 = J_1\exp(-2\beta P_2)$ are consistent with solutions (9).

It follows from Eqs. (7) and (10) that

$$P_2(x,y,z) - P_2(x,-\infty,z) = P_1(-\infty,y,z) - P_1(x,y,z), \quad (11)$$

which reflects the fact that the power gained by beam 2 must equal the power lost by beam 1. The power transfer for each slice, $T(z) = P_2(\infty,\infty,z) - P_2(\infty,-\infty,z)$, is given by

$$2\beta T = \log\left\{\exp(-w_2) + \exp(w_1)\left[1 - \exp(-w_2)\right]\right\}, \quad (12)$$

where $w_1(z) = \eta(\infty,z)$ and $w_2(z) = \xi(\infty,z)$ are the normalized beam widths.

When $\alpha \neq 0$, the interaction of beams 1 and 2 causes their phases to be shifted by ϕ_1 and ϕ_2, respectively. By modifying the analysis of Ref. 4, one can show that the downstream phase shifts

$$\phi_1(y,z) = \alpha P_2(\infty,y,z), \quad \phi_2(x,z) = \alpha P_1(x,\infty,z). \quad (13)$$

According to the laws of geometric optics, the beams are deflected in the direction of increasing phase shift.

Equations (9), (12), and (13) are valid for arbitrary upstream intensity profiles. In the following examples we consider three different profiles: The first profile, $I(u,v) = \exp(-u^2 - v^2)$, is Gaussian, as illustrated in Fig. 73.35(a). The second profile, $I(u,v) = \exp(-u^2 - v^2)\cos^2(\pi u)\cos^2(\pi v)$, has hot spots with a central maximum, as illustrated in Fig. 73.35(b). The third profile, $I(u,v) = \exp(-u^2 - v^2)\sin^2(\pi u)\sin^2(\pi v)$, has hot spots with a central minimum, as illustrated in Fig. 73.35(c). In Figs. 73.36–73.41 all intensities are normalized to I, the peak upstream intensity of a Gaussian beam; all distances are normalized to $1/2\beta I$, the SBS gain length; and all phase shifts are normalized to $\alpha/2\beta$.

In the first example the upstream intensity profiles $I_1(y,z) = \exp(-y^2 - z^2)$ and $I_2(x,z) = 0.5\exp(-x^2 - z^2)$ are Gaussian. Contour plots of the downstream intensity profiles of beams 1 and 2 are displayed in Figs. 73.36(a) and 73.36(b), respectively. The downstream intensity of beam 2, which has a maximum of 1.2, is higher than the upstream intensity of beam 1. Both beams are distorted by the interaction. Beam 2 grows as it propagates in the positive y direction. Consequently, more power is siphoned from the $y > 0$ side of

P1813
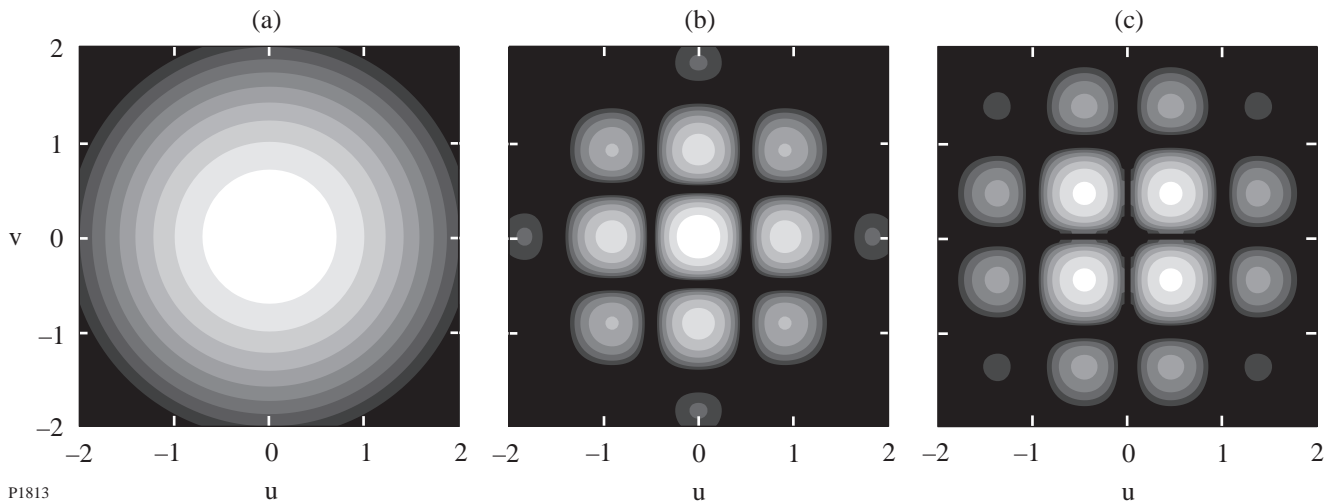
Figure 73.35
Logarithmic contour plots of the upstream intensity profiles used to generate Figs. 73.36–73.41. White represents high intensity; black represents low intensity. (a) Gaussian profile; (b) profile with hot spots and a central maximum; (c) profile with hot spots and a central minimum.
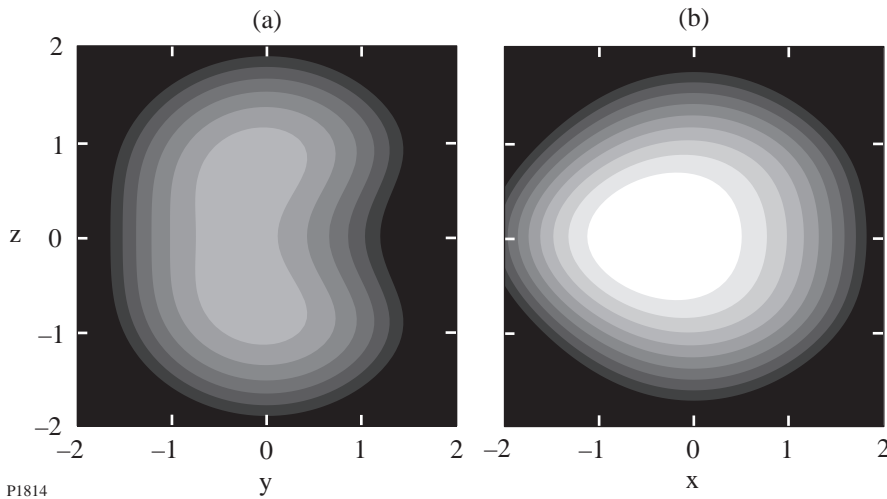
P1814

Figure 73.36
Logarithmic contour plots of the downstream intensity profiles of (a) beam 1 and (b) beam 2 corresponding to upstream intensity profiles that are Gaussian. White represents high intensity; black represents low intensity. Both beams are distorted by the interaction, and their centroids are shifted.
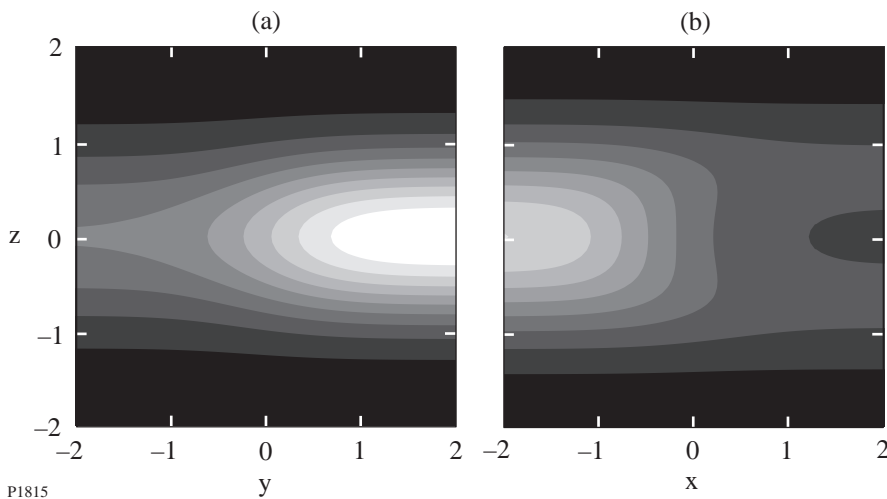
P1815

Figure 73.37
Linear contour plots of the downstream phase shifts of (a) beam 1 and (b) beam 2 corresponding to upstream intensity profiles that are Gaussian. White represents a large positive phase shift; gray represents a small positive phase shift; and black represents a phase shift of zero. Since the beams are deflected in the direction of increasing phase shift, beam 1 is deflected in the positive y direction and beam 2 is deflected in the negative x direction. The upper and lower parts of both beams are deflected toward the z axis.

beam 1 than from the $y < 0$ side, and the centroid of beam 1 is shifted in the negative y direction. The downstream intensity of beam 1 has off-axis maxima because the on-axis slice of beam 1 drives the interaction with the corresponding slice of beam 2 most strongly and is depleted most severely. Beam 1 is depleted as it propagates in the positive x direction. The centroid of beam 2 is shifted in the negative x direction because more power can be siphoned from the undepleted parts of beam 1 than from the depleted parts. Contour plots of the downstream phase shifts of beams 1 and 2 are displayed in Figs. 73.37(a) and 73.37(b), respectively. The maximal phase shift of beam 1 is 2.2. Since the beams are deflected in the direction of increasing phase shift, beam 1 is deflected in the positive y direction and beam 2 is deflected in the negative x direction ($\alpha > 0$). The upper and lower parts of both beams are deflected toward the z axis ($\alpha > 0$).

In the second example the upstream intensity profiles $I_1(y,z) = 4 \exp(-y^2 - z^2) \cos^2(\pi y) \cos^2(\pi z)$ and $I_2(x,z) = 2 \exp(-x^2 - z^2) \cos^2(\pi x) \cos^2(\pi z)$ produce intersecting filaments. The factors of 4 were included to make the beam powers in this example approximately equal to the beam powers in the first example. Contour plots of the downstream intensity profiles of beams 1 and 2 are displayed in Figs. 73.38(a) and 73.38(b), respectively. The maximal intensity of beam 2 is 4.6. According to Eqs. (9), the downstream intensities are the products of the upstream intensities and nonlinear transfer functions that depend on the (spatially integrated) power per unit height of each slice. Thus, the intensity profiles in this example evolve in a manner similar to those in the first example: The centroid of beam 1 is shifted in the negative y direction, and the centroid of beam 2 is shifted in the negative x direction. In this example, however, the

(a)   (b)

P1816

Figure 73.38
Logarithmic contour plots of the downstream intensity profiles of (a) beam 1 and (b) beam 2 corresponding to upstream intensity profiles that produce intersecting filaments. White represents high intensity; black represents low intensity. The beam distortions are more pronounced in this figure than in Fig. 73.36 because the hot-spot intensities are higher than the corresponding intensities of Gaussian beams.

(a)   (b)

P1817

Figure 73.39
Linear contour plots of the downstream phase shifts of (a) beam 1 and (b) beam 2 corresponding to upstream intensity profiles that produce intersecting filaments. White represents a large positive phase shift; gray represents a small positive phase shift; and black represents a phase shift of zero. Beam 1 is deflected in the positive y direction, and beam 2 is defected in the negative x direction. The upper and lower parts of each row of hot spots are deflected toward the center of the row.

distortions are more pronounced because some slices contain twice the power per unit height of the corresponding slices in the first example. Contour plots of the downstream phase shifts of beams 1 and 2 are displayed in Figs. 73.39(a) and 73.39(b), respectively. The maximal phase shift of beam 1 is 5.1. Beam 1 is deflected in the positive y direction, and beam 2 is deflected in the negative x direction ($\alpha > 0$). The upper and lower parts of each row of hot spots are deflected toward the center of the row ($\alpha > 0$).

In the third example the upstream intensity profiles $I_1(y,z) = 4 \exp(-y^2 - z^2) \cos^2(\pi y) \cos^2(\pi z)$ and $I_2(y,x) = 2 \exp(-x^2 - z^2) \sin^2(\pi x) \sin^2(\pi z)$ produce nonintersecting filaments. Contour plots of the downstream intensity profiles of beams 1 and 2 are displayed in Figs. 73.40(a) and 73.40(b), respectively. The maximal intensity of beam 2 is 2.6. The distortions of the intensity profiles in this example are similar to those in the first and second examples. They are less pronounced, however, because the upstream intensity profiles
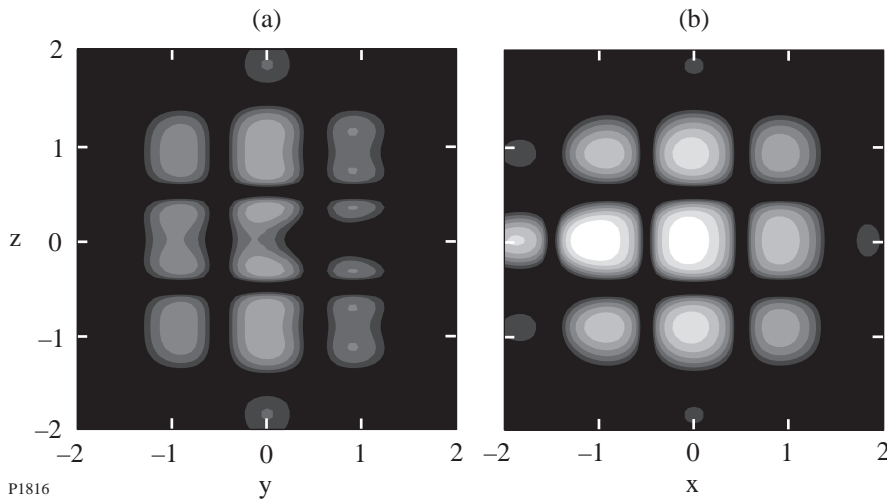

P1818
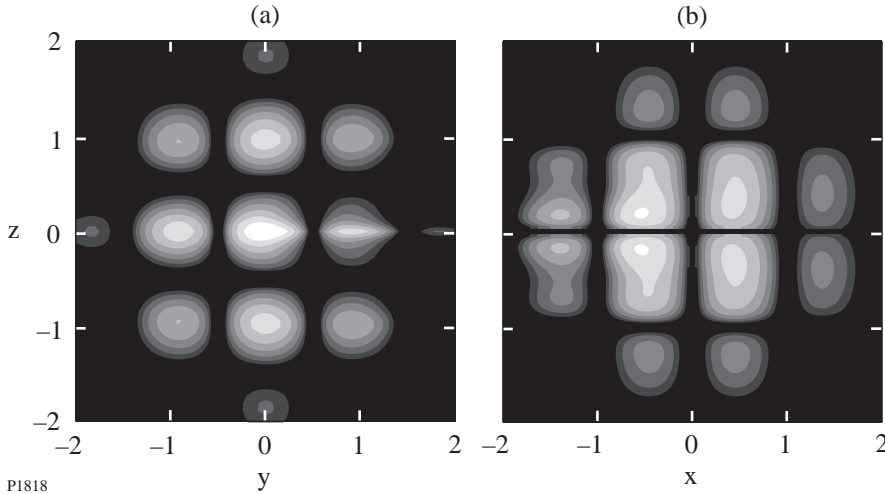
Figure 73.40
Logarithmic contour plots of the downstream intensity profiles of (a) beam 1 and (b) beam 2 corresponding to upstream intensity profiles that produce nonintersecting filaments. White represents high intensity; black represents low intensity. The beam distortions are less pronounced in this figure than in Fig. 73.36 because the beam filaments do not interact strongly.
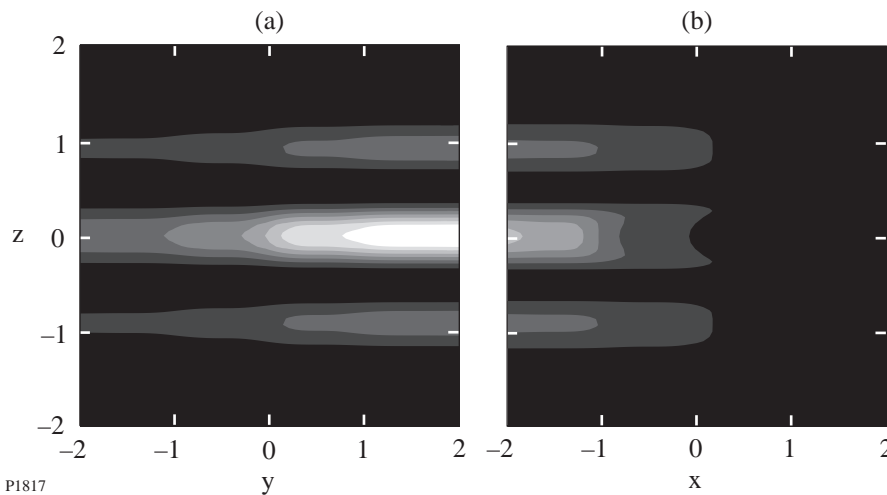

P1819
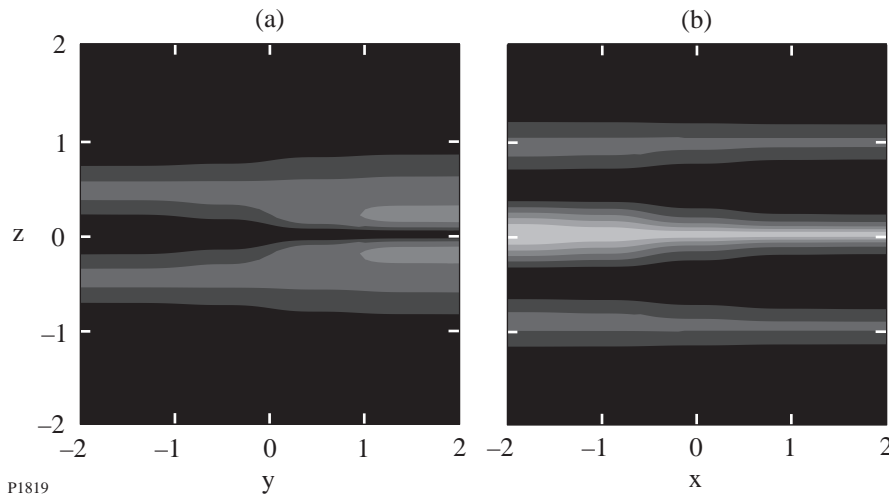
Figure 73.41
Linear contour plots of the downstream phase shifts of (a) beam 1 and (b) beam 2 corresponding to upstream intensity profiles that produce nonintersecting filaments. White represents a large positive phase shift; gray represents a small positive phase shift; and black represents a phase shift of zero. The beam deflections associated with this figure are less important than those associated with Fig. 73.39 because the regions of large phase shift are aligned with the regions of low intensity.

produce filaments that do not interact strongly. Contour plots of the downstream phase shifts of beams 1 and 2 are displayed in Figs. 73.41(a) and 73.41(b), respectively. The maximal phase shift of beam 1 is 2.1. According to Eqs. (13), each beam acquires a phase shift that reflects the intensity profile of the other beam. The regions of large phase shift, however, are aligned with the regions of low intensity, and beam deflections are less important in this example than in the first and second examples.

In summary, we made a three-dimensional analysis of the power transfer between crossed laser beams with arbitrary upstream intensity profiles. We derived simple formulas for the downstream intensity profiles [Eqs. (9)], the power transfer [Eq. (12)], and the downstream phase shifts that depend on the power transfer [Eqs. (13)]. The power transfer shifts the beam centroids, and the phase shifts alter the beam directions and focal lengths. For beams with hot spots in their upstream intensity profiles, the power transfer depends sensitively on whether the associated filaments intersect.

ACKNOWLEDGMENT

REFERENCES

1. J. D. Lindl, Phys. Plasmas **2**, 3933 (1995).

2. W. L. Kruer *et al.*, Phys. Plasmas **3**, 382 (1996).

3. V. V. Eliseev *et al.*, Phys. Plasmas **3**, 2215 (1996).

4. C. J. McKinstrie, J. S. Li, R. E. Giacone, and H. X. Vu, Phys. Plasmas **3**, 2686 (1996). Equations (3) and (4) of this paper were misstated. They should be $A_h = A_1 \exp[i(\mathbf{k}_1 \cdot \mathbf{r} - \omega_1 t)] + A_2 \exp[i(\mathbf{k}_2 \cdot \mathbf{r} - \omega_2 t)] + c.c.$ and $n_l = n \exp[i(\mathbf{k}_1 - \mathbf{k}_2) \cdot \mathbf{r}] + c.c.$, respectively. Equations (5) and (6) are correct.

5. C. J. McKinstrie, V. A. Smalyuk, R. E. Giacone, and H. X. Vu, Phys. Rev. E **55**, 2044 (1997).

6. R. K. Kirkwood *et al.*, Phys. Rev. Lett. **76**, 2065 (1996).

7. A. K. Lal, K. A. Marsh, C. E. Clayton, C. Joshi, C. J. McKinstrie, J. S. Li, and T. W. Johnston, Phys. Rev. Lett. **78**, 670 (1997).

8. M. Maier, W. Kaiser, and J. A. Giordmaine, Phys. Rev. **177**, 580 (1969).

9. B. I. Cohen, Phys. Fluids **17**, 496 (1974).

10. F. Y. F. Chu, Phys. Lett. **51A**, 129 (1975).

Characterization of Freestanding Polymer Films for Application in 351-nm, High-Peak-Power Laser Systems

A major roadblock to rapid progress in laser fusion is the enormous price of the necessary experimental facilities. Currently under planning or nearing construction are 40-cm-clear-aperture (per beam line), 200-or-more-channel, glass-laser systems that will each cost in excess of U.S. 10^9 in pursuit of laser-fusion research.[1] A sizable portion of this price bears witness to the costs of optical materials and of the precision manufacturing methods for treating these materials at aperture scales that, up to now, were the domain of astronomers. There is strong incentive for developing lower-cost, high-throughput manufacturing technology and materials engineering, yielding devices that meet all the performance challenges typically demanded by such lasers.

One key constraint to limiting laser-system cost by aperture downscaling is the so-called *laser-damage threshold*.[2] The higher the damage threshold for given system-operating conditions (wavelength, pulse length, etc.), the more photons per cm^2 and seconds may be passed through a given device without incurring permanent performance penalties. In the asymptotic limit of an infinite laser-damage threshold, one could build infinitely powerful lasers having very affordable, small apertures. Short of this elusive condition, however, the quest for higher thresholds is both a material-design and device-processing imperative. It must be kept in mind, though, that any enhanced laser-damage threshold is useful only if no other optical performance parameters are sacrificed in the process.

Among such parameters are *wavefront quality*, absence of, or at least control of, *birefringence*, and long-term environmental and photolytic stability of the material. The latter assuages the need for reworking, replacing, or swapping devices frequently and thus affects the *operating* costs of large-clear-aperture lasers. The former two parameters are essential to transporting beams both with minimum static phase-front error and without polarization error. Both are pivotal to efficient higher-harmonic frequency conversion and to good focusability of beams onto the fusion targets.

With these demands in mind, we recently set out to test the utility of thin polymer membranes (pellicles) in high-peak-power, UV lasers. Scale-up of such membranes, and their preparation under ultraclean conditions, has been spurred by advances in UV lithography[3] of both semiconductor wafers and liquid crystal displays. The specific aim in these applications is to prevent particulate from falling onto, or settling on, the lithographic photomasks. As these primary applications call for excellent material homogeneity and low UV-absorption loss in pellicles, key prerequisites for successful pellicle use on high-peak-power UV lasers seemed already met. In this article, we will present an account of initial tests of such pellicles under 351-nm irradiation conditions significantly higher in fluence than in normal, photolithographic use.

In the following sections, the foil materials will be defined, the test procedures explained, and test results presented.

Sample Characterization

During this screening samples from three vendors[4] were sorted according to whether or not they were offered for *i*-line lithography, i.e., transmittance tuned for a maximum at 365 nm and prepared from a polymer with 280-nm cutoff (cellulose derivative), or for 248-nm, deep-UV lithography. In the following, we will sidestep reporting on cellulose derivatives since these foils are, in the current context, not noteworthy. They do find use, however, in optical-fuse (i.e., "must fail"), power-limiting applications where defined or downward-adjustable laser-damage thresholds are a key performance requirement.

Vendors offer two pellicle options: bare, single-layer foils or multilayer combinations with antireflective properties. In either implementation, pellicles are thin enough to act as both optically self-referencing etalons and freestanding samples in Fourier-transform IR spectroscopy. As will be shown here, the latter method is a simple and effective analysis tool for specifying the chemical similarities and differences in the samples from various vendors.

For these tests, vendors were not required to supply samples of a *prescribed thickness*, but only of a thickness *typically supplied for lithography applications*. Data, including those in Fig. 73.42, are therefore results from slightly different-thickness films (between 0.9 μm and 2.9 μm).

Figure 73.42 shows an overlay of three samples' IR absorption over the 4000 cm^{-1} to 400 cm^{-1} spectral range. From the general features it becomes immediately apparent that there is prominent overlap among the samples, i.e., largely similar addition polymers are used by the various suppliers. All samples show a weak "waviness" in their spectra—a manifestation of the samples' etalon effect in this wavelength range. Note the absence of any signal in the 2800-cm^{-1} area, the characteristic band for alkyl signatures, as well as the absence of signal around 3200 cm^{-1} for alkenes. There are, instead, strong, overlapping peaks between 1200 and 1400 cm^{-1}, characteristic for condensed system carbon–fluorine Q vibrations.[5] This permits identification of the materials as highly fluorinated (*perfluorinated*) homo- or copolymers. A widely known example of such a compound is tetrafluoroethylene.

After expanding the "fingerprint region" (see Fig. 73.43), subtle differences between samples become noticeable. Transmittance dips at 1030 cm^{-1} and 980 cm^{-1} in sample 2 (throughout this article, samples will be simply identified with numerals 1, 2, and 3 corresponding to sources in Ref. 4) and absent in sample 1 can be assigned to CF$_2$–CO vibrations found in perfluorinated 1,3-dioxolanes.[6] This sample thus belongs to the group of copolymers of perfluorinated dioxolane and tetrafluoroethylene. For certain weight ratios between the two members,[7] this copolymer remains amorphous over a wide temperature range and becomes solvent-processable—an important advantage for manufacturing low-scatter-loss, low-birefringence optical films.

It must be mentioned here that fluoropolymers are not the only deep-UV lithography materials. As early as 1985, a U.S. patent granted to Duly *et al.*[8] disclosed a polymethylmethacrylate pellicle for deep-UV lithography. We did not prepare
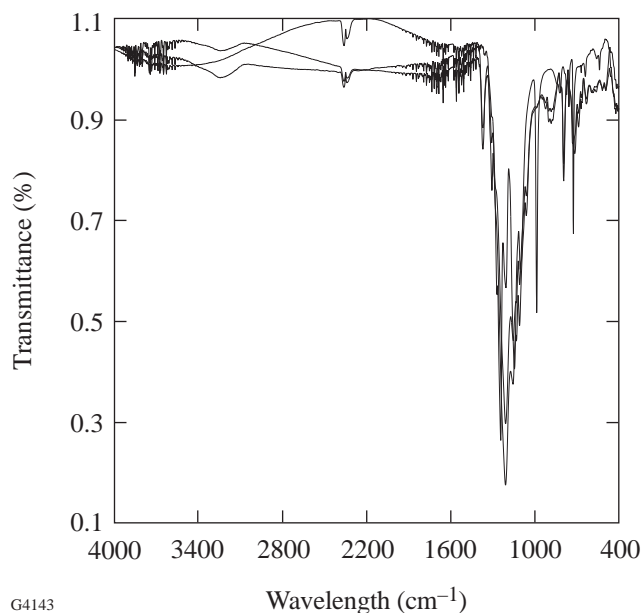
Figure 73.42
Infrared transmittance spectra (400 cm^{-1} to 4000 cm^{-1}) of the three sample types used in these measurements show the absence of alkyl and alkene characteristics (2900 cm^{-1} to 3200 cm^{-1}), while displaying strong carbon–fluorine vibrations.

G4143
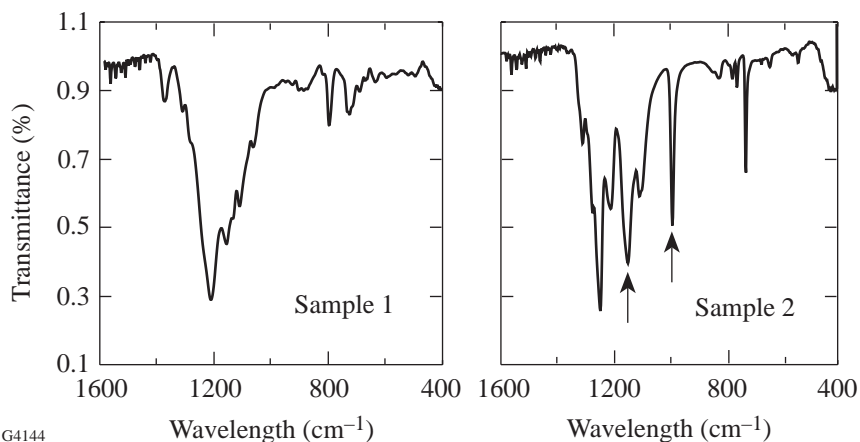
Figure 73.43
The "fingerprint" region (400 cm^{-1} to 1900 cm^{-1}) of the spectrum in Fig. 73.42. The fluorodioxolane signatures at 1030 cm^{-1} and 980 cm^{-1} are absent in sample 1 and highlighted in sample 2.

G4144

or obtain a pellicle from this material for comparison purposes; however, the issue of acrylates in high-peak-power laser use will be revisited during the discussion of current results.

Test Procedures

1. Damage-Threshold Measurements

A 7-s-repetition-rate, frequency-tripled Nd:glass laser in a standard laboratory environment is used for laser-damage testing. Its pulse length is 0.5 ns at the third harmonic, produced by Fourier-transform spectral narrowing through intracavity etalons, and the UV interaction spot size at the pellicle surface is 600 μm, produced by a 2-m-focal-length, fused-silica lens. The pulse length is sporadically monitored by a combination of a vacuum photodiode[9] and a 6-Ghz oscilloscope.[10] Each sample site is imaged under 110× dark-field microscopy both before and after laser irradiation. Any permanent, observable sample change is identified as damage.

At each irradiation instance, a digital record of the fluence distribution in a sample-equivalent plane is used to calculate the maximum shot fluence on target. Two irradiation modes are practiced: 1-on-1 and *N*-on-1. Samples are first tested in 1-on-1 mode and subsequently in *N*-on-1 mode. Mounted on a raster stage, random sample sites are moved into the irradiation position and irradiated by either one exposure (1-on-1 mode) or a sequence of increasingly intense pulses (*N*-on-1). The purpose of 1-on-1 irradiation lies in finding an *average damage threshold* averaged over a statistical number of sample sites. Backing off from this single-exposure average value by about a factor of 2, one may in subsequent *N*-on-1 testing start a fluence sequence at each *N*-on-1 site that ramps up until the damage fluence for each specific site has been found. Again this is carried out over a statistical number of sites. *N*-on-1 testing offers the more *realistic* threshold values as it simulates multishot, in-system-use conditions and accounts for various material-hardening effects known from the literature.[11]

In the case of 1-on-1 measurements, the average threshold value is the mean between the *highest nondamaging fluence* and the *lowest damaging fluence*, with the error derived from summing over all data points within the interval bracketed by these two fluences.

2. Photolysis Characterization

Long-term photolytic stability, i.e., change in sample absorbance in response to a large number of irradiations (1000) by *below-average-damage-threshold fluences* (nominally 3 J/cm^2, i.e., the maximum 351-nm system-design fluence on the

OMEGA laser), is monitored by a calorimeter pair that samples the ratio of incident to transmitted pulse energy. To save time, a 5-s pulse repetition period is chosen. As a consequence, the unequal decay times of the two calorimeters introduce a constant bias that is measured under "sample absent" conditions over several hundred shots. Its slope is subsequently compared with that obtained under "sample in" conditions. Any observable *slope* differences are manifestations of sample photolysis effects.

This qualitative procedure is preferred over spectrophotometric measurements that offer quantitative results because of the small irradiation spot size (see previous section) and the associated registration accuracies involved in moving samples from one instrument to another. Even after registration issues are resolved, the task becomes one of microspectrophotometry, i.e, special effort has to be made to probe only the prior irradiated sample area if measurement sensitivity is to be kept acceptable.

3. Birefringence

Sample birefringence was evaluated by two methods: (1) a facile, low-contrast, visual check across the entire aperture between crossed sheet polarizers (100:1 contrast), and (2) a spot-by-spot measurement using a laser ellipsometer at 1053 nm. In this instrument, the sensitivity limit is 1/40 of a wave retardance averaged across a 0.8-mm spot size.

4. Interferometry in Transmission

A commercial interferometer[12] at $\lambda = 633$ nm was used to measure *transmission* wavefront errors in a double-pass mode. The interferometer is housed in a vibration-isolated, temperature- and air-draft–controlled enclosure.

Results

Even a decade ago, serious attempts at strengthening the laser-damage threshold of polymers[13] pointed out the critical importance of removing trace impurities from the (polyacrylic) polymer matrix. With the absorbance criterion having been made more rigorous since then by lithography demands, materials and processes for pellicles in 248-nm KrF excimer-laser lithography undergo strict optical-loss control,[3] both in terms of particulate as well as dissolved absorbers. It is thus not fully unexpected that we are able to report here the highest, 351-nm-laser-damage thresholds in our records covering tests on inorganic and organic optical materials for more than 15 years. The results are summarized in Fig. 73.44.

In Fig. 73.44, 1-on-1 and *N*-on-1 thresholds for the three vendors' foils are displayed. Although there is considerable variation among the thresholds for pellicles from different vendors, even the lowest reported threshold among them at 20 J/cm² is well above any operational 351-nm fluence on any large-scale glass laser in use or under design to date. Regarding these values, an important distinction must be made. In the **Test Procedures** section, the methodology for arriving at damage-threshold values was described. The thresholds marked with an asterisk in Fig. 73.44, i.e., those above 42 J/cm², *do not strictly comply* with this methodology for the following reason: The laser in use is *unable to generate the fluences at the given interaction spot size*, necessary to ascertain the *highest nondamaging fluence*. Thresholds marked with an asterisk represent the lowest damaging fluence obtainable from our laser at this spot size *for this given material*. In this regard, the perfluorinated pellicles are unique among the 1780 samples damage tested at this facility to date. They may also be unique at still shorter wavelengths.[14]

An additional challenge in determining these extraordinarily high thresholds derives from the interaction of the laser beam with air: at the stated fluences, particulates in air may get ionized near the sample surface and, pellicles being excellent dielectrics, locally charge the polymer. It becomes a daunting task to distinguish the electrostatically adhering particulates from "genuine damage" scatter sites. The threshold for vendor 3 at 69 J/cm² is an average over two sites on two films, both sites exhibiting a single detectable scatterer that remains uncertain as to whether or not it attracted dust.

Figure 73.44 also reveals a consistent hardening in all samples upon multiple irradiation, i.e., the *N*-on-1 thresholds exceed the 1-on-1 thresholds by up to 30%. While this effect is neither new nor unique to these samples, it must be noted that the just-mentioned charging by air ionization may provide the basis for photorefractive effects in these polymers. In this instance, charge-separation time constants are critical, and the damage thresholds measured at the very-low repetition governing the current *N*-on-1 measurements, i.e., the sample is investigated after *each* exposure, are expected to be different from those that one would obtain under *high-repetition-rate* conditions. Such tests are still to be carried out.

For comparison, 351-nm bulk damage fluences for KDP (potassium dihydrogen phosphate) frequency-conversion crystals, as acquired for the OMEGA laser during the last five years, are lower by factors of 3 to 5 (with current crystal-growth technology, the canonical number is 10 J/cm² @ 351 nm, 1 ns). Three factors seem responsible for this remarkable superiority in damage-threshold values: (1) There is the already-mentioned attention to purity in starting materials and cleanliness in membrane processing. (2) More importantly, these pellicles intrinsically do not have to suffer the violent intrusions by grinding and polishing, typical for conventional optical elements, in order to achieve the transmission-wavefront uniformity reported below. (3) Being freestanding, frame-supported films, they expose very little bulk to the transiting laser pulse. Since thermodynamics requires that a finite density of defects must exist, even in very pure materials, this last property may be the pellicles' greatest asset in laser applications.

These advantages are further illustrated by data in Table 73.V, where 351-nm damage-threshold values are listed for a 240-nm-thick, inorganic, SiO$_x$ film simultaneously vacuum-deposited on three different substrates and damage tested concurrently with the pellicles, i.e., under similar irradiation conditions. (The film stoichiometry is identified with only *x* here since no effort was made to accurately ascertain its value. We believe that *x* = 2.) This comparison shows how severe a price is paid for grinding and polishing: the damage threshold for the same film drops by an order of magnitude, depending on whether it is deposited on a conventionally
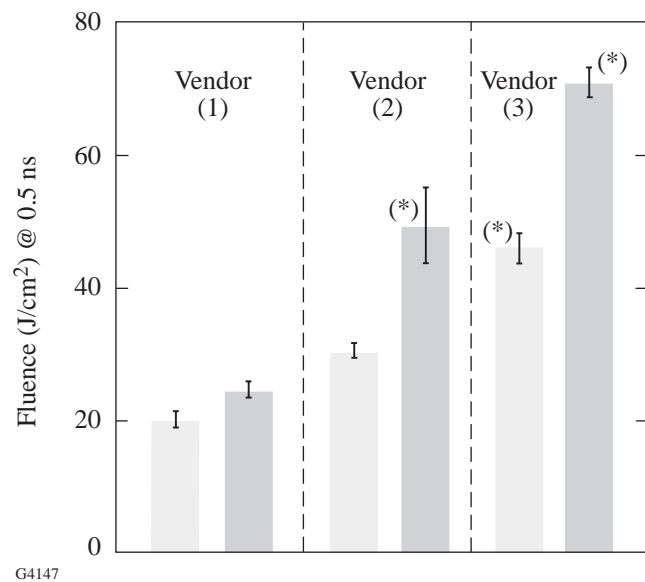

G4147

Figure 73.44
1-on-1 (light gray) and *N*-on-1 (dark gray) average damage thresholds for the three sample types identified as (1), (2), and (3) and tested at 351 nm (0.5-ns pulse length). Different sample types were received from different vendors. For the meaning of the asterisks, consult the text.

Table 73.V: Comparison of 351-nm, 0.5-ns laser-damage thresholds in J/cm^2 for a 240-nm-thick SiO$_2$ film concurrently vacuum deposited on three select surfaces: conventionally polished and cleaned fused silica,[15] freshly cleaved fused silica,[15] and freshly cleaved float glass.

Substrate Material and Surface Condition	Damage threshold (J/cm^2)	
	1-on-1	N-on-1
Polished fused silica	6.9±0.3	9.7±1.1
Cleaved fused silica	22.8±2.5	34.6±2.0
Cleaved float glass	27.7±1.3	24.5±2.0

prepared and cleaned fused silica[15] surface or on a freshly cleaved, otherwise untreated surface of either fused silica or inexpensive float glass. A lift-off technology, as is applied to the preparation of pellicles, can avoid this downside of conventional manufacturing.

As the sample films are homogenous, single-material layers, the *E*-field distributions of the transiting laser pulse inside the polymer are expected to *not exceed* the corresponding magnitudes *in vacuo*. No *E*-field *enhancement* needs to be considered in determining laser-damage thresholds for these films.

Next, we address sample *birefringence* results. Figure 73.45 shows a side-by-side comparison of parallel polarizers and crossed polarizers. Also included in the images is an extruded, 5-μm-thick Mylar® foil[16] whose intrinsic birefringence pattern in the two cases offers an instructive reference. Similar

data exist, but are not shown here, for all vendors' pellicles. In quantitative terms (ellipsometry), no pellicle, including those with clear apertures as large as 30 cm, offered a single site in which the local birefringence exceeded the instrument sensitivity (λ/40 @ 1053 nm). Moreover, by applying uniaxial stress to square-frame–mounted pellicles of 0.9-mm thickness, even at stresses that visibly (unaided eye) distorted the frame, induced film birefringence remained below instrument sensitivity. In accordance with vendor specifications,[17] the stress-optic coefficient for perfluorinated-pellicle materials lies within 10% of that of the widely used stress-modeling material polymethacrylate. Owing to their short pathlength, however, pellicle films, even if nonuniformly stressed by, for instance, mounting or temperature biases, respond with retardance excursions tolerable in most high-peak-power laser systems.

Long-term photolytic stability, as measured by energy ratiometry, shows no measurable increase in absorptance in perfluorinated foils after 1000 exposures at nominally 3-J/cm^2 fluences per given site. The data shown in Fig. 73.46 represent ten-shot average values per data point for two cases: solid circles are data for beams passed through samples; open circles for "no-sample" conditions. The horizontal axis marks a cumulative number of shots. The offset between the two similarly sloped curves corresponds to the Fresnel insertion loss for this particular sample (16%, includes etalon reflectance and absorption). The slope itself is a result of unequal amounts of energy being deposited in each calorimeter at a repetition rate shorter than the thermal decay time of the calorimeter(s). Since any long-term increase (or decrease) in sample absorbance would have to manifest itself in a *change* in this slope,

Parallel Polarizers   Nearly Crossed Polarizers
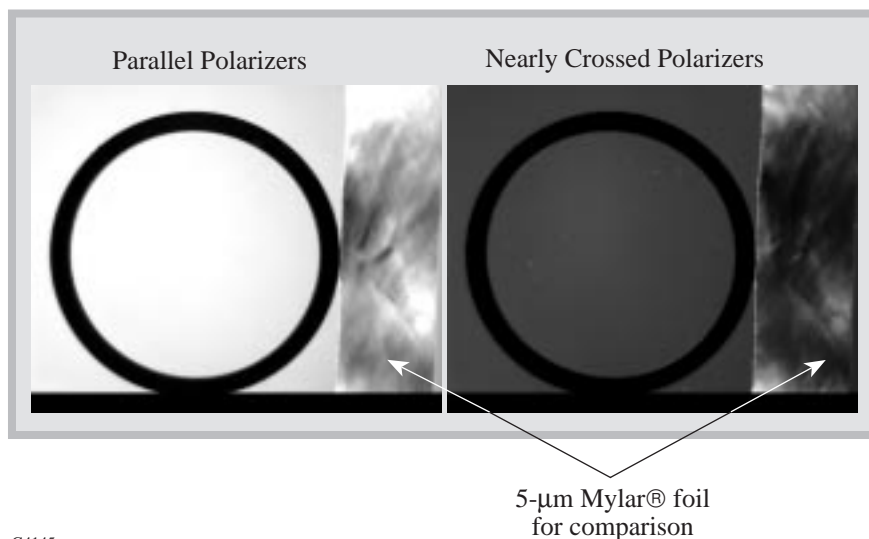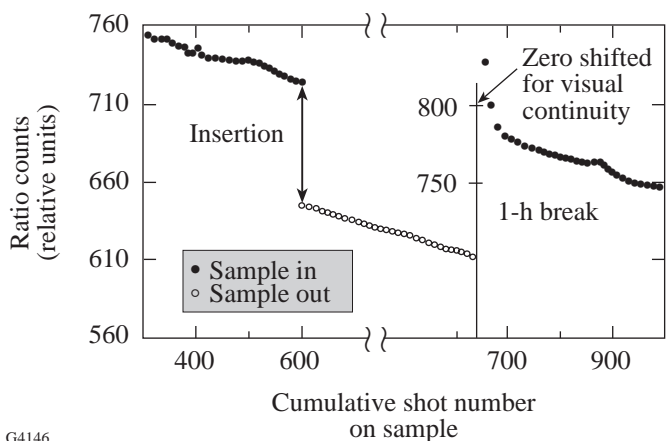
5-µm Mylar® foil for comparison

Figure 73.45
Comparison of birefringence between a 5-cm-clear-aperture, perfluorinated pellicle and an extruded, 5-μm-thick Mylar® foil placed between (a) parallel and (b) nearly crossed polarizers. Note the extensive stress birefringence imparted onto the Mylar® foil by the manufacturing process.

G4145

G4146

Figure 73.46
Calorimetric ratios of incident over transmitted energy (each data point is a ten-shot average) as a function of accumulated exposure. Nominal fluences on each shot were 3 J/cm^2. Full circles: sample in the beam; open circles: sample out.

the good agreement among slopes in Fig. 73.46 is taken as evidence for sufficient absence of such a cumulative absorbance increase. For a much smaller number of exposures per site, this is further corroborated by the distinction between 1-on-1 and N-on-1 thresholds depicted in Fig. 73.44. If there was substantial photolytic activity present in these samples, the evidenced "hardening" trend among all three sample types would be reversed.

We note here in passing that this absence of photolytic processes distinguishes the perfluorinated foils from cellulose-derivative ones, which, owing to such "photorefractive" response, give rise to interesting nonlinear scattering phenomena.[18] We note further that future large-scale laser systems are designed for >3-J/cm^2 maximum 351-nm fluence. Long-term photolytic stability in the 10- to 20-J/cm^2 fluence range still remains to be tested.

We also note that within the limited laser-output-power/spot-size phase space of our setup, i.e., a limited-range intensity gainlength test, a special effort to detect transverse stimulated Brillouin scattering yielded only *null results* in perfluorinated samples.

Interferometric tests of *thickness uniformity* (wavefront uniformity) pose a genuine challenge: the phase error measured between two consecutive, *empty-cavity* scans taken 10 min apart *is larger than* the phase error detectable *after the pellicle is inserted*. This result is true for pellicles up to 40 cm long (longest dimension). Thus, pellicle uniformity is better

than can be measured with current state-of-the-art interferometers. This was independently verified by spectrophotometric scans at select sites across the pellicle aperture (all at 0° incidence). The objective in this test was to discern site-dependent wavelength peak shifts in the etalon spectral peaks in response to path-length differences. Again, within instrument resolution, only null results were obtained. As one would expect, such pellicles "ring" under all realistic mounting conditions—interferometry in *reflection* is a fruitless exercise, even if the sample film is mounted on a lapped frame that, by itself, is interferometrically flat.

System-Integration Considerations

From a systems-integration viewpoint, these perfluorinated films offer advantages but also a few drawbacks. Although highly elastic, the membranes are only a few microns thick and, accordingly, vulnerable to mechanical attack. Rapidly changing air-pressure differentials across the membranes, or directed air bursts typical of procedures for dust removal from optical surfaces, may cause membrane rupture. Another challenge is the still-limited clear-aperture size available commercially. The laser systems mentioned at the outset are designed for near-40-cm clear aperture: to date no perfluorinated pellicle measuring *40 cm in every direction* has been made. The largest pellicles available to this laboratory are 30 cm × 40 cm and 30 cm in diameter (circular).

Owing to the "drumhead" vibrations, pellicles are not suitable for image-quality, *reflective* applications. If the requirement, however, is simply one of getting photon energy into a certain direction, such as toward spatially integrating detectors or sensors, this drawback will be irrelevant.

Another challenge is posed by the *very low surface energy* of perfluorinated polymers (well-known "Teflon® effect"). There is not great latitude in choosing materials for multilayer designs, as poor wettability of perfluorinated surfaces makes uniform spin deposition of other materials nearly impossible.

Summary

The advantages of freestanding polymer film pellicles, apparent from the foregoing discussion, are rapid fabrication (spin on, lift off, mount on frame), robustness against 351-nm laser damage, photolytic stability, chemical inertness, amorphous structure, excellent transmitted-wavefront uniformity, and absence of birefringence. The best pellicles tested to date show UV damage thresholds up to five times higher than the frequency-conversion crystals (KDP) required for converting glass-laser output to the UV.

REFERENCES

1. *Energy and Technology Review*, Lawrence Livermore National Laboratory, Livermore, CA, UCRL-52000-94-12, 1 (1994).

2. Many empirical as well as fundamental research results on laser damage can be found in the series of proceedings from the Annual Symposia on High-Power-Laser Materials (Boulder Conferences) published by the U.S. Government Printing Office as Special NBS Publications (until 1990) and by SPIE (after 1990).

3. T. Shirasaki *et al.*, in *Photomask and X-Ray Mask Technology*, edited by H. Yoshihara (SPIE, Bellingham, WA, 1994), Vol. 2254, pp. 392–400.

4. Shin-Etsu Chemicals, New Functional Materials Department, Research Center, Annoka, Gunma, Japan; DuPont Photomasks, Inc., Danbury, CT 06810; MicroLithography, Inc., Sunnyvale, CA 94089.

5. L. M. Sverdlov, M. A. Kovner, and E. P. Krainov, *Vibrational Spectra of Polyatomic Molecules* (Wiley, New York, 1974), p. 397.

6. J. R. Throckmorton, J. Org. Chem. **34**, 3438 (1969).

7. E. N. Squire, U.S. Patent No. 4,948,851 (14 August 1990); U.S. Patent No. 4,973,142 (27 November 1990).

8. D. L. Duly, H. Windischmann, and W. D. Buckley, U.S. Patent No. 4,523,974 (18 June 1985).

9. Hamamatsu U1381R-01, Hamamatsu Photonic Systems, Bridgewater, NJ 08807-0910.

10. Tektronix 7250, Tektronix, Inc., Beaverton, OR 97077.

11. M. R. Kozlowski *et al.*, in *Laser-Induced Damage in Optical Materials: 1990*, edited by H. E. Bennett *et al.* (SPIE, Bellingham, WA, 1991), Vol. 1441, pp. 269–282.

12. Zygo Mark IV-XP, Zygo Corporation, Middlefield, CT 06455-0448.

13. K. M. Dyumaev *et al.*, Bull. Acad. Sci. USSR Phys. Ser. **53**, 194 (1989).

14. While this manuscript was completed, 248-nm test results (15 ns) on select samples became available, buttressing the results listed here: T. Lehecka, U.S. Naval Research Laboratory (private communication). Request further information at lehecka@nemesis.nrl.navy.mil.

15. Corning 7940, Corning, Inc., Technical Products Division, Corning, NY 14831.

16. DuPont Mylar®, DuPont Packaging and Industrial Polymers, D-5100, Wilmington, DE 19898.

17. DuPont AF-1600, DuPont Fluoroproducts, Wilmington, DE 19880-0702.

18. S. Papernov, A. Schmid, and F. Dahmani, "Laser Damage in Polymer Waveguides Driven Purely by a Nonlinear, Transverse-Scattering Process," to appear in *Optics Communications*.

Subsurface Damage in Microgrinding Optical Glasses

In cold processing of optical glasses by microgrinding,[1,2] the resulting brittle-material-removal rate induces a cracked layer near the glass surface, referred to as subsurface damage (SSD). [Editor's note: The acronym for subsurface damage (SSD) used in this article should not be confused with its more common use as an acronym for smoothing by spectral dispersion.] In addition, there is a corresponding surface microroughness (SR), often found to increase in proportion to SSD, as originally observed by Preston.[3] SSD is a statistical measure and not necessarily equal to the flaw depth that may control mechanical strength of the brittle surface.

Direct measurement of SSD is tedious: The dimple method is often used[4,5] as well as wafering methods. Aleinikov[6] showed that SSD induced by lapping of glasses and other brittle ceramics (with hardness changing 30-fold, fracture toughness 6-fold, and Young's modulus 20-fold) was 3.9±0.2 times SR for SiC abrasives (100 to 150 μm), thus indicating that SSD may be estimated from SR. Aleinikov also found that SSD increased with increasing size of microindentation cracks (see Fig. 73.47). Thus, microindentation may be used to evaluate propensity to damage in lapping.

More recently, Edwards and Hed[8] studied the relation of SSD to SR under bound-diamond-abrasive conditions (53 to 65 μm and 180 to 250 μm in size) and found that for the three glasses studied (borosilicate crown BK7, zerodur, and fused silica) the average SSD was 6.4±1.3 times the peak-to-valley surface roughness (measured by a profilometer). The factor of 6.4 was arrived at by dividing SSD by SR for each glass. This proportionality factor becomes identical to that of Aleinikov[6] when all three materials tested by Edwards and Hed[8] are treated together (see Fig. 73.48). Similar observations have been reported for deterministic microgrinding of optical glasses with bound-abrasive-diamond tools of smaller size (2 to 4 μm) (see Lambropoulos et al.[9]).

In addition to correlating SSD with SR, it is possible also to correlate SSD for brittle materials with the materials' mechanical properties. Zhang[10] used metal bond wheels with bound diamond abrasives (40 to 230 μm in size) to grind structural ceramics under fixed infeed conditions and reported a subsurface damage depth (consisting of voids induced by the grinding) that correlated with the ductility index $(K_c/H_V)^2$ of these materials (see Fig. 73.49). The ductility index[9] is
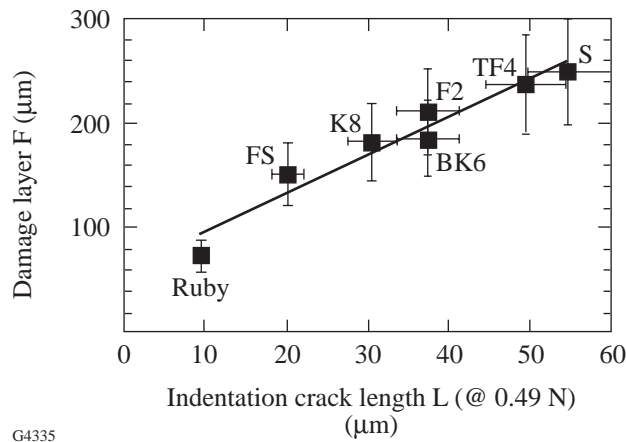
Figure 73.47

SSD in lapping versus indentation crack size (0.49 N) for brittle materials, based on Aleinikov.[6] Russian glass K8 is equivalent to Schott BK7 (Hoya BSC7, Ohara S-BSL7).[7]
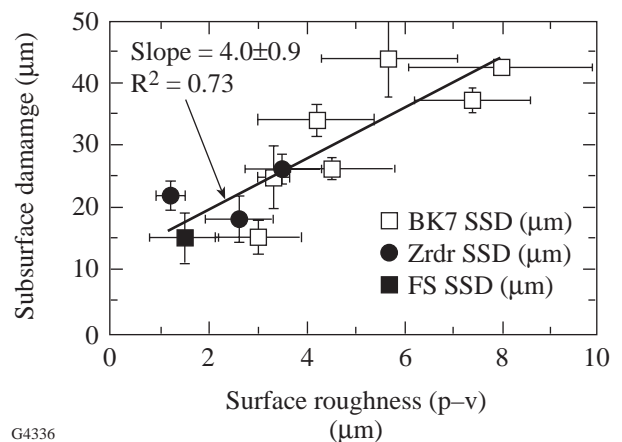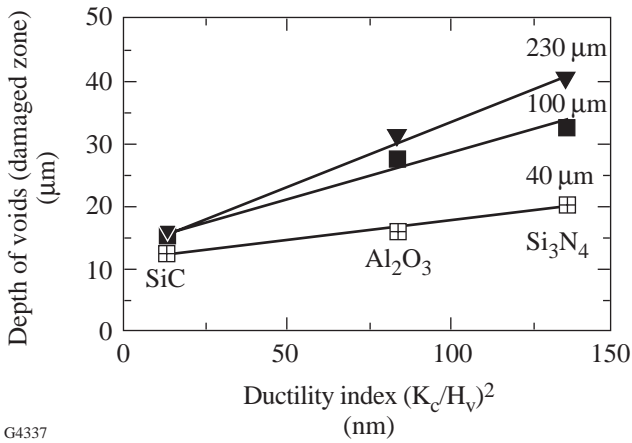
Figure 73.48

Relation of SSD to SR, as measured in bound-diamond-abrasive grinding by Edwards and Hed.[8]

G4337

Figure 73.49
Subsurface damage versus mechanical properties of structural ceramics (SSD data from Zhang[10].)

inversely related to the brittleness H/K_c originally introduced by Lawn *et al.*[11,12]

In our notation, H denotes hardness, or resistance to plastic, irreversible deformation, measured by estimating the area of an indentation impressed under load P. Hardness is defined in terms of either projected area or actual area of contact. Specifically, H_K denotes Knoop hardness, extracted from measuring the long diagonal of a rhomboidal pyramid impression under load P by P/(projected contact area) = (constant) P/(long diagonal)^2, with the (constant) dependent on the rhomboidal pyramid geometry. H_V denotes Vickers indentation, extracted from measuring the average diagonal of a square pyramid impression under load P by P/(actual contact area) = (con-

stant) P/(average diagonal)^2, with the (constant) dependent on the square pyramid geometry. For the same measured diagonal, Knoop indentations penetrate about half as much into the surface as Vickers indentations; thus, H_K more closely measures near-surface hardness. Generally, Knoop hardness H_K increases with Vickers hardness H_V. This correlation has been described in detail by Lambropoulos *et al.*[9]

Microgrinding Experiments
1. Lapping: Surface Roughness (SR) versus Subsurface Damage (SSD)

In all the following experiments, surface roughness was measured by a white-light interferometer (NewView 100, 0.35 × 0.26 mm^2, 20× Mirau, five measurements per surface) and subsurface damage by the dimple method (typically three to five dimples per surface[4,5]).

The goal of the lapping experiment was to investigate whether surface roughness can provide information about subsurface damage. Loose-abrasive lapping experiments were conducted on two glasses: the soft phosphate laser glass LHG8 (63% P_2O_5, 14% BaO, 12% K_2O, 7% Al_2O_3, 4% Nd_2O_3/Nb_2O_5) and the harder borosilicate crown optical glass BK7 (68.9% SiO_2, 10.1% B_2O_3, 8.8% Na_2O, 8.4% K_2O, 2.8% BaO, 1% As_2O_3, % by weight) (see Table 73.VI).

Five separate LHG8 blocks were lapped on both sides with Al_2O_3 abrasives (median size 30, 9, 5, 3, 1 μm). Measured SSD and SR, after grinding with each abrasive, are shown in Fig. 73.50.

Table 73.VI: Thermomechanical properties of optical glasses. Data for density ρ, glass transition temperature T_g, coefficient thermal expansion α, Young's modulus E, and Poisson ratio v are from manufacturers' glass catalogs. Hardness H and fracture toughness K_c are from Schulman *et al.*[16] Knoop hardness is at 1.96 N. The fracture toughness of LaK9 was estimated from that of LaK10.

Glass	ρ (g/cm^3)	T_g (°C)	α (10^{-6} °C^{-1})	E (GPa)	v	H_K (GPa)	K_c (MPa m$^{1/2}$)
LHG8	2.83	485	12.7	50	0.26	2.3	0.43
FS-C7940	2.20	1,090	0.52	73	0.17	5.6	0.75
SF58	5.51	422	9.0	52	0.26	2.7	0.46
SF7	3.80	448	7.9	56	0.23	3.4	0.67
BK7	2.51	559	7.1	81	0.21	5.1	0.82
K7	2.53	513	8.4	69	0.21	4.6	0.95
KzF6	2.54	444	5.5	52	0.21	3.7	1.03
LaK9	3.51	650	6.3	110	0.29	5.7	(0.90)
TaFD5	4.92	670	7.9	126	0.30	7.3	1.54
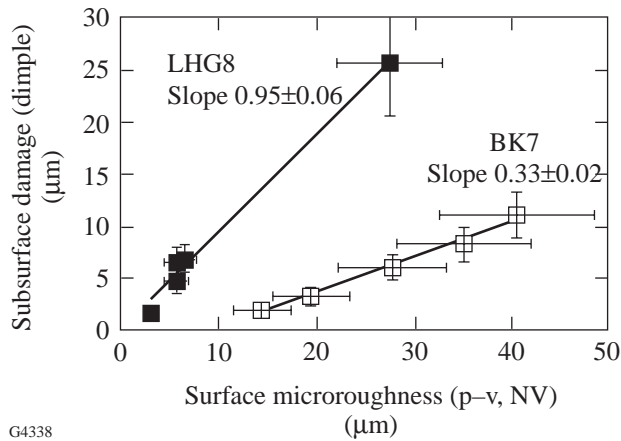
Figure 73.50
Correlation of SR (p–v) with SSD for loose-abrasive lapping of optical glasses (Al_2O_3 abrasives).

A similar experiment used BK7 with a wider abrasive size range (median size 40, 30, 20, 9, 5, 3, 1 μm). A single BK7 part was first lapped by 40-μm abrasives, then with 30-μm abrasives, and finally with 20-, 9-, 5-, 3-, and 1-μm abrasives. SSD and SR were measured at each step. Each lapping step removed between 0.3 to 1 mm of material and thus removed all the residual SSD from the previous abrasives used in the sequence. Larger abrasives typically led to higher SSD and higher SR.

The correlations of the subsurface damage to the peak-to-valley surface roughness for lapped LHG8 and BK7 are shown in Fig. 73.50. For LHG8 the p–v SR is equal to the measured SSD, whereas for BK7 the p–v SR is about 3 to 5 times the measured SSD. We conclude from these experiments that the p–v SR measured with the white-light interferometer provides an upper bound for the SSD measured by the dimple method.

2. Deterministic Microgrinding: Surface Roughness (SR) versus Subsurface Damage (SSD)

A series of multicomponent optical glasses, as well as fused silica,[13] were also ground under fixed infeed deterministic microgrinding conditions on the Opticam SM CNC machining platform,[14,15] which can manufacture planar and spherical surfaces, as well as aspheres.[9,14,15] Table 73.VI summarizes some of the glass properties.

Three metal-bonded diamond-abrasive ring tools were sequentially used on each surface (aqueous coolant Loh K-40, relative speed of work and tool of about 30 m/s): 70 to 80 μm, 10 to 20 μm, and 2 to 4 μm at infeed rates of 1 mm/min, 50 μm/min, and 5 μm/min, respectively. Three cuts were done with each tool. After each cut, SR of the optical surface was

measured for microgrinding with all three tools, and SSD (three dimples for each cut) for the 2- to 4-μm and 10- to 20-μm tools.

Figure 73.51 shows the correlation between the measured p–v and rms SR for the three tools used, with each point representing one of the glasses ground and measured. Figure 73.52 shows the correlation of SSD (dimple method) and the p–v SR. It is seen that, as in lapping, the p–v SR may be used as an upper bound for the SSD for the 10- to 20-μm and 2- to 4-μm tools, within the uncertainty in the measurement of SSD and SR.
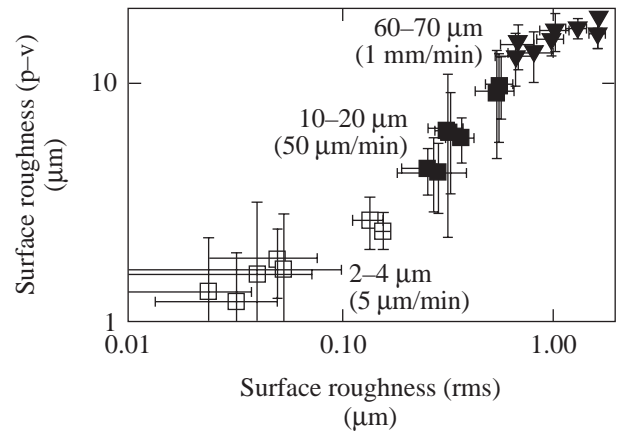
Figure 73.51
Correlation of p–v and rms SR under fixed infeed deterministic microgrinding of various optical glasses.
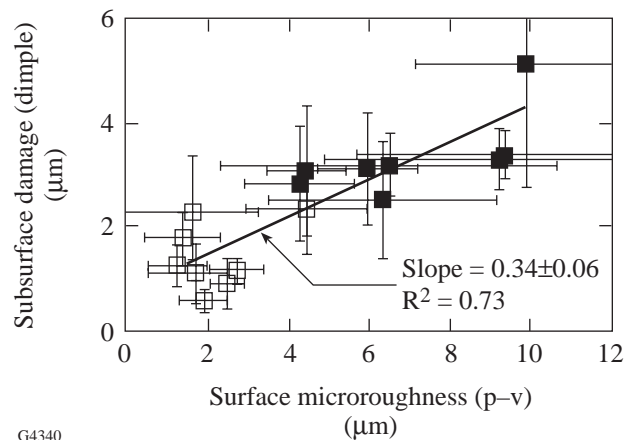
Figure 73.52
SSD (dimple method) versus p–v SR (via NewView 100 white-light interferometer) for fixed infeed deterministic microgrinding.

The effect of glass mechanical properties on SSD is shown in Fig. 73.53, where we have used the ductility index as the correlating parameter.[9] It is seen that, under fixed infeed grinding conditions, increasing ductility produces higher SSD, as observed in structural ceramics (Fig. 73.49). Correlations of measured SSD with the critical depth of cut discussed by Bifano et al.[17] or the critical load for fracture initiation discussed by Chiang et al.[18,19] gave similar trends.

The dependence of SSD on the ductility index is interpreted by a simple model of residual tensile stresses $\sigma \approx \beta \sigma_y$ (parallel to the surface), where $\beta \approx 0.08$[20] and σ_y is glass uniaxial yield stress ($\sigma_y \approx H_V/2$, see Ref. 9). Thus, crack depth a in the presence of such tensile stresses is estimated as

$$K_c = \Omega \left(\beta \, \sigma_y \right) \sqrt{\pi a} \Rightarrow a = \frac{1}{\pi} \left(\frac{K_c}{\Omega \beta \sigma_y} \right).$$

$\Omega \approx 1.1$ is a geometric factor accounting for the proximity of the free surface. Typical data for, say, BK7 give a crack depth of 2.1 to 4.3 μm, i.e., quite comparable to the measured SSD (see Fig. 73.52).

3. Comparison of Surface Quality Induced by Lapping and Deterministic Microgrinding

Figure 73.54 compares the surface quality of the optical glass BK7 (commonly used in many optical designs) resulting from loose-abrasive lapping with Al_2O_3 abrasives (seven sizes spanning 1 to 40 μm) and from deterministic microgrinding (three sizes spanning 3 to 75 μm) with bound diamond abrasives, over a wide range of abrasive sizes. The infeed rates for deterministic microgrinding were 5 μm/min (2- to 4-μm tool), 50 μm/min (10- to 20-μm tool), and 1 mm/min (70- to 80-μm tool). For both lapping and deterministic microgrinding, larger abrasives lead to deeper SSD and higher SR. The lapping results apparently become insensitive to abrasive size for abrasives in the 1- to 3-μm range.

For a given abrasive size, deterministic microgrinding results in surfaces with lower subsurface damage and lower surface microroughness (p–v or rms). Such surface features are in addition to any "figure" features extending over the whole aperture of the ground optical surface.

Conclusions

The quality of a manufactured optical surface can be characterized in a variety of ways, including surface microroughness[9] subsurface damage, surface figure error, residual stresses induced by the grinding process,[20,21] the rate of material removal,[22] and the rate of tool wear. In our work we have concentrated on subsurface damage and surface microroughness and addressed the following questions:

How can subsurface damage in a given brittle material be estimated from the measured surface microroughness? How can subsurface damage among brittle materials be correlated to their near-surface mechanical properties? How is the resulting
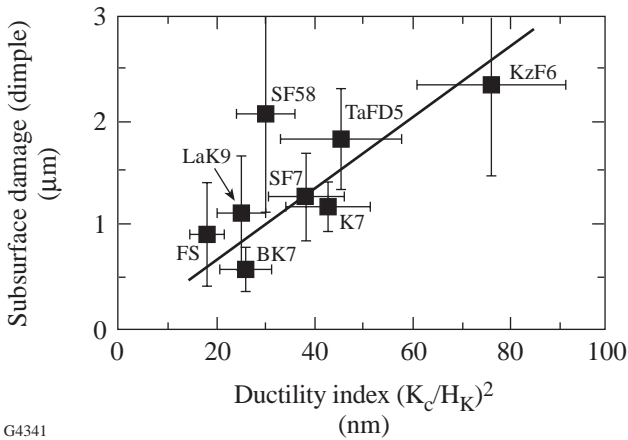

G4341

Figure 73.53
Dependence of subsurface damage SSD on glass mechanical properties via the ductility index $(K_c/H_K)^2$.
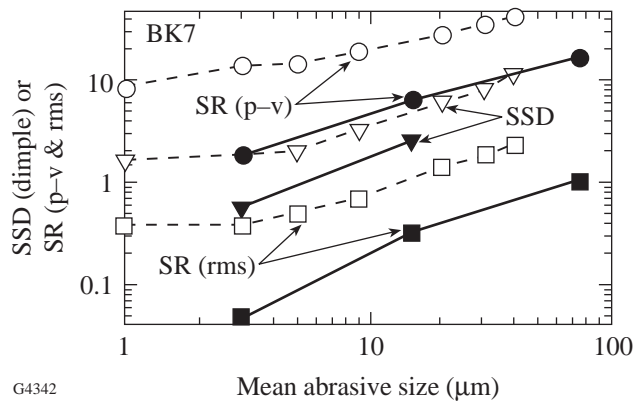

G4342

Figure 73.54
BK7 surfaces: lapping at fixed pressure (open symbols) versus deterministic microgrinding at fixed infeed with metal bonded-diamond-abrasive ring tools (solid symbols).

surface quality affected by material removal under loose-abrasive microgrinding at fixed nominal pressure (lapping) or by deterministic microgrinding under fixed infeed rate?

We have performed a series of loose-abrasive microgrinding (lapping at fixed nominal pressure) and deterministic microgrinding (at fixed infeed) experiments on various optical glasses. We summarize our results as follows:

- Peak-to-valley surface microroughness for the optical glasses tested (measured by the white-light interferometer, a relatively easy measurement to perform) provides an upper bound to the subsurface damage measured by the more-time-consuming dimple method;

- Subsurface damage in optical glasses under deterministic microgrinding conditions with 2- to 4-μm bound-diamond-abrasive tools scales with the glass ductility index $(K_c/H)^2$ in a manner similar to that reported for fixed infeed grinding of structural ceramics;[10] and

- For a given abrasive size, deterministic microgrinding produces lower subsurface damage and lower surface microroughness as compared to lapping.

The issue of residual stresses induced by grinding is also important and often referred to as the Twyman effect.[21] Although we have not measured residual stresses in this work, our previous work on optical glasses[20] and glass ceramics[23] shows that, for comparable abrasive sizes, deterministic microgrinding induces lower residual stresses than loose-abrasive lapping, while maintaining a higher material-removal rate and producing a lower surface roughness.

REFERENCES

1. T. S. Izumitani, *Optical Glass*, American Institute of Physics Translation Series (American Institute of Physics, New York, 1986), Chap. 4, pp. 91–146.

2. H. H. Karow, *Fabrication Methods for Precision Optics* (Wiley, New York, 1993), Chap. 5.

3. F. W. Preston, Trans. Opt. Soc. **XXIII**, 141 (1921–22).

4. A. Lindquist, S. D. Jacobs, and A. Feltz, in *Science of Optical Finishing*, 1990 Technical Digest Series (Optical Society of America, Washington, DC, 1990), Vol. 9, pp. 57–60.

5. Y. Zhou *et al.*, J. Am. Ceram. Soc. **77**, 3277 (1994).

6. F. K. Aleinikov, Sov. Phys. Tech. Phys. **27**, 2529 (1957).

7. L. B. Glebov and M. N. Tolstoi, in *CRC Handbook of Laser Science and Technology*, Vol. V: Optical Materials, Part 3, Supplement 2: Optical Materials, edited by M. J. Weber (CRC Press, Boca Raton, FL, 1995), pp. 823–826.

8. D. F. Edwards and P. P. Hed, Appl. Opt. **26**, 4677 (1987).

9. J. C. Lambropoulos, T. Fang, P. D. Funkenbusch, S. D. Jacobs, M. J. Cumbo, and D. Golini, Appl. Opt. **35**, 4448 (1996).

10. B. Zhang, in *Proc. ASPE*, 1996 Spring Topical Meeting on Precision Grinding of Brittle Materials (ASPE, Raleigh, NC, 1996), Vol. 13, pp. 76–81.

11. B. R. Lawn, T. Jensen, and A. Arora, J. Mater. Sci. **11**, 573 (1976).

12. B. R. Lawn and D. B. Marshall, J. Am. Ceram. Soc. **62**, 347 (1979).

13. Corning 7940, Corning, Inc., Technical Products Division, Corning, NY 14831.

14. H. M. Pollicove and D. T. Moore, Laser Focus World, March 1991, 145.

15. H. M. Pollicove and D. T. Moore, in *Optical Fabrication and Testing Workshop Topical Meeting*, 1992 Technical Digest Series (Optical Society of America, Washington, DC, 1992), Vol. 24, pp. 44–47.

16. J. Schulman, T. Fang, and J. Lambropoulos, *Brittleness/Ductility Database for Optical Glasses*, ver. 2.0, Department of Mechanical Engineering and Center for Optics Manufacturing, University of Rochester, Rochester, NY (1996).

17. T. G. Bifano, T. A. Dow, and R. O. Scattergood, Trans. ASME, B, J. Eng. Ind. **113**, 184 (1991).

18. S. S. Chiang, D. B. Marshall, and A. G. Evans, J. Appl. Phys. **53**, 298 (1982).

19. *ibid.*, 312.

20. J. C. Lambropoulos, S. Xu, T. Fang, and D. Golini, Appl. Opt. **35**, 5704 (1996).

21. J. C. Lambropoulos, S. Xu, and T. Fang, Appl. Opt. **36**, 1501 (1997).

22. F. Twyman, *Prism and Lens Making: A Textbook for Optical Glassworkers*, The Adam Hilger Series on Optics and Optoelectronics (Hilger & Watts, London, 1952), p. 318.

23. J. C. Lambropoulos, B. E. Gillman, Y. Zhou, S. D. Jacobs, and H. J. Stevens, in *Optical Manufacturing and Testing II*, edited by H. P. Stahl (SPIE, Bellingham, WA, 1997), Vol. 3134, pp. 178–189.

Bound-Abrasive Polishers for Optical Glass

Optical finishing of glass consists of generating (grinding) and polishing stages. In grinding, brittle fracture is performed on a workpiece using a series of two or three bound-abrasive grinding tools. These tools are composed of diamonds in a metal or resin matrix. The generating process starts with a coarse (~60 μm) diamond tool, and concludes with a medium (~15 μm) and (optional) a fine (~3 μm) tool. Reliable, repeatable, deterministic microgrinding with ring tools using Opticam CNC machining platforms developed at the Center for Optics Manufacturing (COM) produces spherical surfaces with rms surface microroughness of ~10 nm,[1] subsurface damage with a depth of less than 3 μm,[2] and peak-to-valley (p–v) surface shape errors less than 0.3 μm (λ/2).[3] On blanks to 100 mm in diameter, the process takes minutes per surface. Bound-diamond-abrasive ring tool generating has been adopted by many optics manufacturing companies in the U.S. as part of a modern finishing strategy when small quantities of prototype lenses are required with rapid turnaround. No specialized tooling is required, and diamond ring tools may be obtained from many suppliers.[4]

Determinism in the polishing stage of optics manufacturing continues to be elusive. As it is traditionally employed, polishing is a full-contact operation between a polishing lap, or *polisher*, and the workpiece. An aqueous abrasive slurry is introduced to the contact zone to hydrate the glass surface, and removal of the softened near-surface layer is achieved by chemomechanical effects and plastic scratching.[5] Loose-abrasive slurries are typically composed of cerium oxide (CeO_2) in water.[6] The polisher is composed of pitch or polyurethane on a cast iron backing plate.[7] Pitch is the preferred lapping surface for achieving subnanometer surface finishes on glass with high precision. Although much progress has been made in understanding slurry fluid chemistry,[8] slurry-workpiece electrostatics,[6] and the interaction among polishing abrasive, the polisher, and the part,[5] the conventional pitch polishing process continues to be heavily iterative in nature. Pitch is chemically unstable and loses organic volatiles with time.[9] Its compliance is also very sensitive to temperature.[10] As a reference template against which the part is continuously worked, a pitch lap must

be frequently checked and corrected. The polishing step is the main bottleneck to reducing finishing time in rapid prototyping. Sub-aperture processing technologies using small pitch-surfaced tools[11] or ion beams[12,13] have found utility in selected applications. A newly developed process, magnetorheological finishing, has demonstrated the ability to rapidly and automatically polish out flats, concave/convex spheres, or aspheres on a magnetic fluid lap with no specialized tooling.[14]

An optics manufacturing company invests in excess of $200K to purchase, install, and operate a CNC diamond ring tool generating machine that can produce a *nearly* finished glass part. There is strong economic incentive to devise ways that would permit the use of such a machine to complete the finishing process by polishing out the part, thereby eliminating the need for any further processing steps and machines. One possible approach is to develop a bound-abrasive ring tool polisher, resident in the on-board automatic tool changer, to act as a final surface-finishing tool. The use of a bound-abrasive polisher has several potential advantages: Confinement of the abrasive in a binder enables finishing to be performed on a CNC machine platform. Large quantities of loose abrasives would destroy the guideways of the machine. A bound-abrasive polisher is less likely to deform under load and changes in temperature. Significantly less abrasive is required in the finishing process, thereby reducing the cost of consumables. Removal rates can be high. Issues of concern are the physical integrity of the polishing tool in use at ~1000 rpm (e.g., resistance to dissolution from the aqueous coolant, or fracture/crumbling under load), the ability to efficiently smooth the glass surface without ruining the surface figure, and the polisher's performance for different glass types.

Information in the Russian literature, primarily from V. V. Rogov and colleagues, addresses the use of bound polishing abrasives in the form of pellets affixed to a cast iron plate. They investigated pellet composition, tool rotation rate, and load for a variety of glasses.[15–17] The resulting pellet media, called Aquapol®,[18] are described as dimensionally stable from 10°–80°C. By introducing a superfine diamond grinding stage

to their process, a Moscow manufacturing enterprise was able to use Aquapol pellet polishing in distilled water to finish parts with some success. They noted, however, that the Aquapol materials "are rather brittle and possess low mechanical strength, which inevitably results in debris and crumbling at the edges of elements during operation and makes the tool unusable."[19] To avoid this problem, a form of nearly full contact Aquapol lap with a central hole was conceived and tested.[20] This concept proved successful for commercial-quality (e.g., figure accuracy tolerances to ~1 μm, rms surface roughness levels less than 10 nm) flat and spherical parts up to 50 mm in diameter. It was implemented at a number of factories throughout the former Soviet Union.

No information is available in the open literature regarding the use of bound-abrasive polishers in a ring tool geometry on CNC machine platforms. In this article we describe the development and testing of bound-abrasive compositions in three geometries: pellet, ring tool, and full-contact lap. We show that for several glass types, our compositions reduce rms surface roughness of initially fine ground surfaces to less than 2 nm in ~30 min. We demonstrate that bound-abrasive ring tools are compatible with CNC machine platforms, although maintaining or reducing surface figure errors is a problem that requires more study. We find, however, that it is feasible to use bound abrasives in *prepolishing* operations to remove grinding tool marks and dramatically shorten the time required for pitch polishing.

Key Performance Criteria, Variables, and Choices

There are five principle performance criteria for the successful development of a bound-abrasive polisher: First, the polisher must maintain its physical integrity during use at moderate to high velocities, in an aqueous environment, and under light to moderate load. Second, the polisher must release particles of polishing abrasive at a rate that promotes efficient removal of glass from the workpiece surface, but not so rapidly as to cause excessive tool wear, or so slowly that the tool surface "glazes" over with a solid film of binder. Third, the polisher must be manufactured in such a way that it exhibits reproducible performance under constant operating conditions. Fourth, the polisher must be capable of removing artifacts from grinding (e.g., tool marks, shallow scratches) to achieve an rms surface microroughness of less than ~2 nm in a reasonable period of time. Fifth, required surface figure tolerances must be met with the polisher.

Experiments on bound-abrasive polishers are complex because of the large number of variables and choices available in terms of polisher composition, manufacturing method, polisher geometry, workpiece glass type/shape, and polishing machine platform. The variables involved and the choices made for this work are summarized below.

1. Composition

Based upon the Russian work,[15] a successful bound-abrasive polisher consists of (in wt%) ~60 to 90/polishing agent, 5 to 25/binder, and 5 to 15/erosion promoter. Relative concentrations of abrasive/binder/erosion promoter are investigated here. Because of its high polishing efficiency for many soft and moderately hard glasses,[8] CeO_2 is the polishing abrasive of choice. An impure CeO_2/rare earth oxide blend, known as Polirit,[21,22] is used in the Aquapol media. It has a particle size of approximately 2 μm and is nominally 50% CeO_2. Polirit is available from several sources, and the variations in its composition from batch to batch have been noted.[23] We use three CeO_2 products with similar particle-size distributions and a range of purity levels from 50%–90%[24] (see Table 73.VII). The binder can be a polyimide, a phenolic (used in the Aquapol media), or an epoxy. From our earlier work[25] we have identified and use a low-viscosity, two-part epoxy[26] that can be readily impregnated with a high percentage of solids. The final ingredient in the polisher is an additive to promote erosion. Two types are studied here, separately and in combination, and their behavior is illustrated in Fig. 73.55. Ammonium chloride (NH_4Cl)[15] dissolves in the aqueous coolant during polishing to expose fresh abrasive particles to the work zone. Hollow alumina spheres[27] crush under mechanical loading and act as a form of controlled porosity to break up the binder material.

2. Manufacturing Method/Geometry

Because commercial mixing machines are costly and require large batch sizes, hand mixing was used to prepare all compositions according to a fixed methodology and cure schedule. Hand mixing has been found reliable and repeatable. The documentation given in this article is sufficient to transfer the manufacturing method to others. Mold geometry is limited to three forms in this work: pellet arrays (individual pellets waxed into arrays, or monolithic molded pellet arrays), rings, and full-contact laps.

3. Workpiece Glass Type/Shape

We concentrate on polishing commonly used optical glasses BK7,[28] SF7,[29] SK7,[29] SK14,[29] LaFN21,[29] TaFD5,[30] and fused silica,[31] whose Knoop hardness values fall in the range of ~3.4 to 6.7 GPa (350 to 680 kgf/mm^2) @ 200 gf.[32] Part shape is fixed at 35- to 50-mm diameter by 10 mm thick. Worked surfaces are either flat or spherical (convex 70-mm

Table 73.VII: Compositions and physical properties of Aquapol and selected experimental polishers.

ID#: Composition, wt%[*]	Shore D Hardness		Young's Modulus GPa	Shear Modulus GPa	Density (g/cm³)	Form Used[***]
	air	water[**]				
Polirit CeO_2 50% pure[22]/ 2.0-μm size[42]						
#AS: Aquapol standard unknown composition	90	66	18.0	7.8	3.99	spa rt
CeRite 415K CeO_2 75% pure[43] / 2.0-μm size[44]						
#1: 94 CeO_2 6 epoxy 0 e.p.	88	11	12.1	4.8	3.99	rt
#2: 93 CeO_2 7 epoxy 0 e.p.	78	23	11.3	4.5	3.96	mpa rt
#3: 75% CeO_2 10% epoxy 15% e.p. (all h.al.s.)	88	81	14.1	5.7	3.20	rt
CeRite 4251 CeO_2 50% pure[43]/1.5-μm size[44]						
#4: 75% CeO_2 10% epoxy 15% e.p. (all h.al.s.)	73	63	na	na	2.53	mpa rt
CeRox 1663 CeO_2 90% pure[43]/1.0-μm size[44]						
#5: 63% CeO_2 25% epoxy 12% e.p. (10 h.al.s. + 2 a.cl.)	75	na	12.4	4.7	2.64	mpa rt
#6: 85% CeO_2 10% epoxy 5% e.p. (all a.cl.)	70	60	na	na	3.40	mpa rt

  * e.p.–erosion promoter (h.al.s.–hollow alumina spheres; a.cl.–NH_4Cl)
 ** 60-min soak @ 25°C in buffered pH 10 DI water with gentle agitation
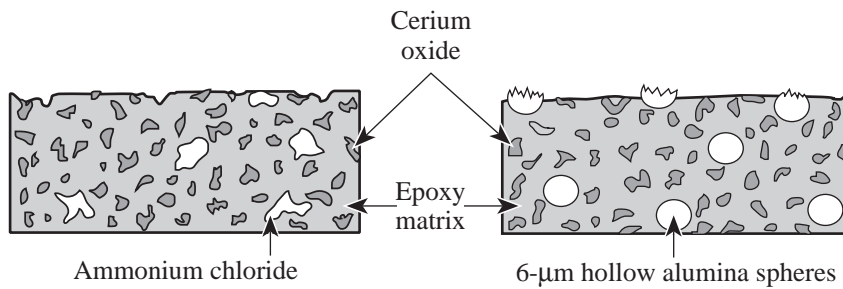*** spa–single-pellet array; mpa–molded-pellet array; rt–ring tool

Figure 73.55
Ammonium chloride and hollow alumina spheres help promote erosion of the binder to expose fresh cerium oxide grains.

COM53

radius of curvature). Initial surface finish varies, depending on the method of preparation (loose abrasive grinding or ring tool generating).

4. Polishing Platforms

We evaluate polishing efficiency on three testbeds. A single-spindle polishing machine[33] is used for pellet polisher work with flat parts. This geometry is the easiest to implement and can be done with student assistants. Ring tool polishing trials are conducted on an Opticam SX CNC generating machine.[34] A collaborating company's[35] results from trials with full-contact polishers on semi-automated equipment are also reported.

Polisher Preparation and Bound-Abrasive Properties

To prepare a polisher, the abrasive and erosion promoter are dry mixed by hand and divided in half by weight. One portion is dispersed into two parts by weight of epoxy resin A, and the other is dispersed into one part by weight of epoxy hardener B. Once loaded with solids, A and B are separately hand mixed for 5 min, combined into a single batch, and hand mixed for an additional 10 min. A typical batch varies in weight from 50 g to 250 g. To prepare individual pellets similar in shape to the Aquapol media, the batch is poured into several 15-ml-capacity, plastic centrifuge tubes.[36] These tubes are tapped and mechanically vibrated to remove any entrapped air and cured at room temperature for 24 h. After curing, tubes are sliced open, and the cylindrical plugs are cut on a diamond saw[37] into 17.5-mm-thick pellets (12-mm diameter) with parallel surfaces. The individual pellets are mounted onto an aluminum plate with pitch or wax. Figure 73.56 illustrates the individual pellet polisher configuration. An alternative method uses an RTV silicone mold[38] containing an array of holes. The mold is treated with a mold-release agent,[39] and the batch is spread into it and cured. The 12-mm-diam pellets emerge in the form of a monolithic array (see Fig. 73.57), which is waxed to an aluminum plate. Other mold geometries are used to make solid rings. Full-contact laps are made by first creating a

silicone mold master with a sample product part acting as a reference template.

For compositions containing >90-wt% solids, a small amount (10 ml per 100 g) of methanol[40] is added to resin A and hardener B to further reduce initial viscosities prior to loading in and mixing the solids. The use of methanol causes some cracking and fracture in molded rings during curing. This presents no problem since broken segments are glued together when being mounted onto a supporting ring tool chuck.

Mechanical properties testing for hardness and density verify the ability of different people to produce polishers with the same properties (±5%) when using our manufacturing method.[41] Table 73.VII gives property information for some experimental compositions. All six formulations function as bound-abrasive polishers, as will be demonstrated in the following sections. It is instructive to compare their physical properties with those of the standard hardness Aquapol media.

The Aquapol composition #AS is the hardest (Shore D) and least compliant (Young's modulus) material in Table 73.VII. It is brittle and easily fractured during routine handling and loading against a glass surface. By using an epoxy instead of a phenolic binder, we reduce hardness and increase compliance to improve handling. All experimental compositions show this feature. The CeO_2 concentration is so high in #1 and #2 that an erosion promoter is not necessary. A potential disadvantage to such a high abrasive concentration is the reduction of material resistance to disintegration in water. Measurements of hardness after soak tests in pH 10 water (a typical coolant requirement for CNC glass grinding machines[45]) show that compositions #1 and #2 are less robust.

A 1% increase in epoxy concentration (#1 to #2) improves soak test durability for a modest sacrifice in hardness. A further 3% increase to 10 wt% (#3, #4, #6) and higher (#5) greatly enhances soak test durability to that seen for Aquapol. (Soak
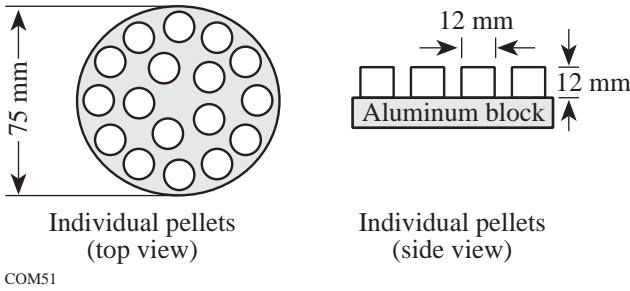
75 mm

12 mm

12 mm

Aluminum block

Individual pellets (top view)

Individual pellets (side view)

COM51

Figure 73.56
Setup for pellet array polisher manufactured from single pellets.

75 mm

12 mm

9 mm

12 mm

Aluminum block

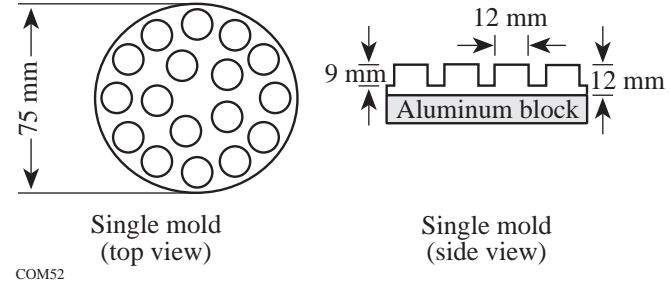Single mold (top view)

Single mold (side view)

COM52

Figure 73.57
Setup for molded pellet array polisher.

tests, however, are not necessarily the best measure of a bound-abrasive polisher's durability in use as discussed later.) In addition to acting as erosion promoters, hollow alumina spheres in #3, #4, and #5 help to maintain high hardness and stiffness at high epoxy concentrations. Table 73.VII shows that, from a fabrication perspective, viable polishers may be manufactured from any of the three commercial CeO_2 abrasives.

Experimental Results for Pellet Laps

The objective was to evaluate the ability of flat, pellet array laps to reduce rms surface roughness of loose-abrasive–ground, flat glass parts to <2 nm in a fixed 30-min polishing cycle. Work reported is for compositions #5 and #6. Freshly made pellet array laps were dressed to expose the abrasive by working against a cast iron plate with ~9 μm alumina.[46] This also trued the surface. Glass parts of differing composition and physical properties were conditioned in the same manner to establish an initial ground surface whose rms surface roughness values were between 300 and 500 nm.[47] Work was carried out on a single-spindle machine,[33] lap on bottom, with the following setups: spindle speed, 35 rpm; eccentric speed, 58 rpm; front center adjustment, 0 mm; back center adjustment, 25 mm; load, 17.2 kPa (2.5 psi). The coolant was DI water, directed onto the lap and recirculated without filtration at a rate of ~200 ml/min. Results, summarized in Table 73.VIII, show that composition #5 works well for polishing out glasses with moderate hardness values. Composition #6 (higher CeO_2 concentration, less erosion promoter) works well for harder glasses, but twice as much time is required to polish down to below 2 nm rms. Other work (not reported here) shows that these polishers do not perform as well for crystalline materials (Si, Ge, CaF_2, ZnSe) whose hardness values fall outside the test range.

Table 73.VIII: Polishing results for bound-abrasive pellet array laps after 30 min.

Composition	Glass	(Hardness[*])	Final rms[47] (nm)
#5	SF7	(3.4)	1
	SK7	(4.8)	1
	BK7	(5.1)	1
#6	fused silica	(6.5)	1.5 (60 min)
	TaFD5	(6.7)	1.5 (60 min)

[*]Knoop hardness, GPa @ 200 gf[32]

Molded Ring Tool Polishers

Several molded ring tool polishers were evaluated on the Opticam SX CNC generating machine.[34] Figure 73.58 shows the schematic of a ring tool polisher against a glass part. Major differences exist between the single-spindle machine used for flat pellet array polishing studies and the Opticam SX. The single-spindle machine utilizes a constant force approach for the lapping process. The Opticam SX uses a constant infeed rate for the cutting process with metal-bonded, diamond ring tools. The single-spindle machine operates at relatively low speeds and pressures, and experiments can be conducted with any desired coolant. Minimum tool and part speeds on the Opticam SX are 1000 rpm and 150 rpm, respectively. The coolant used for the SX polishing experiments is a filtered, high-viscosity grinding coolant, complete with corrosion inhibitors, defoamers, and fungicides.[48]

All compositions except #5 were manufactured in the form of solid and segmented ring tools for testing on the Opticam SX. Both flat and convex surfaces on either BK7 or SK14 glass (similar in hardness to SK7) were polished. All parts were prepared for polishing with the ring tool grinding strategy

summarized at the beginning of this article. Initial values of rms surface roughness were from 25 to 35 nm,[47] and the presence of residual grinding tool marks was noted (see below) on all parts. The programmed depth of cut (DOC) for each trial varied, but most trials had a 60-μm DOC and required ~15 min to complete. (It was not possible to measure the actual amount of glass material removed in a trial, due to the slightly compliant nature of the tools.) A wear path ~1 mm wide was typically observed on a tool surface after a trial. Tool wear was observed to be higher for compositions with higher CeO_2 concentrations. Table 73.IX shows that these polishers can reduce rms surface roughness to ≤1 nm. All in-house polishers maintained their mechanical integrity at speeds of 1000 rpm. There were
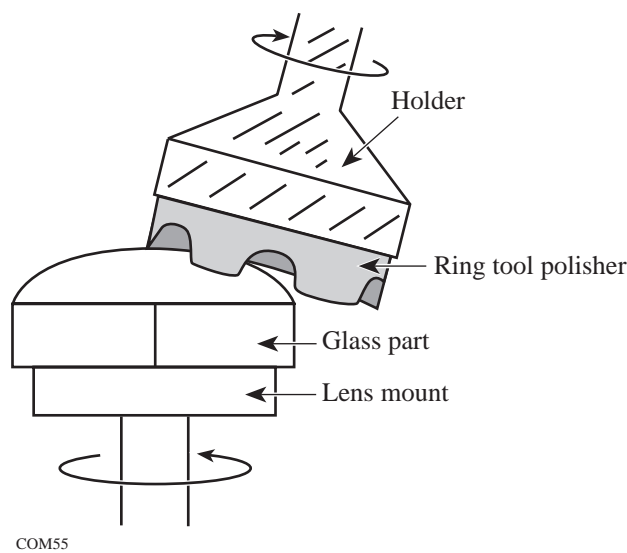

COM55

Figure 73.58
Schematic of bound-abrasive ring tool polisher.

no adverse effects noted on the guideways of the machine. In contradiction to the soak test results, compositions #1 and #2 held up well in the coolant spray, possibly because the time of exposure is reduced by 4× compared to that of the soak test. The Aquapol AS composition tool exhibited serious erosion problems in the commercial coolant, so it was therefore used for shorter, 5-min runs with a DOC of 30 μm. For these short runs, the standard Aquapol material performed well.

It is useful if, as part of the polishing process, the polisher can remove diamond ring tool grinding marks. Referred to as "cutter" marks, they are produced on the part surface as a result of relative vibrations between the machine and the part and exhibit a circumferential periodicity that varies from 2 mm near part center to 10 mm near part edge. Figure 73.59 shows a radial profile scan[49] of a BK7 surface ground with a 10- to 20-μm diamond ring tool. The cutter marks have an amplitude of ~1000 Å and an edge periodicity of ~10 mm. Pitch laps and the high-cerium-oxide-concentration compositions #1 and #2 are very effective at removing cutter marks, as shown in Fig. 73.60. Other polisher compositions are similarly effective.

Attempts to reduce surface figure errors with bound-abrasive ring tools were not successful. Initial p–v surface figure values of 0.3 μm (λ/2) were seriously degraded by the tendency of the ring to polish a 0.5- to 2.0-μm-deep hole into the part center, regardless of shape (flat or convex sphere). A bound-abrasive ring tool polisher causes degradation to the surface figure when it does not wear rapidly enough to expose fresh CeO_2. The result is constant-force polishing similar to conventional polishing, on a machine designed to remove material at a constant infeed using diamond ring tools. The constant-force polishing causes excessive dwell in the part center. This can be avoided by going to a different bound-abrasive polishing tool shape and contact configuration.

Table 73.IX: Results for bound-abrasive ring tool polishing on the Opticam SX.

Composition	Part Shape	Glass	Programmed DOC (μm)	Final rms[47] (nm)	Tool Wear	Tool Marks Removed
#AS	flat	BK7	30	0.8	higher	yes
#1	flat	BK7	60	1.8	higher	no
#2	flat	BK7	120	1.10	higher	yes
	convex	SK14	60	0.6		yes
#3	flat	BK7	90	1.0	lower	yes
#4	flat	BK7	60	1.1	lower	yes
#6	convex	SK14	60	0.9	lower	no

An alternative polishing configuration, called contour mode polishing, is illustrated in Fig. 73.61. In this geometry, the peripheral face of the tool is used to remove material by following a tool path that traverses over the surface of the rotating workpiece (see infeed path motion in Fig. 73.61). A new aspheric generating machine, the Opticam AG, was recently delivered to the COM.[50] It possesses the correct configuration for use as a testbed for future trials of bound-abrasive polishers in a new form, that of a contour tool. Our expectation is that it should be possible to significantly reduce figure degradation when polishing in this manner.

Molded Full-Contact Polishers

Several full-contact polishers were molded from composition #6 for a local optics company[35] to test on LaFN21 glass (Knoop hardness, 6.18 GPa @ 200 gf). The polishers were made to a specified 11.48-mm radius of curvature and 22-mm diameter by using a sample lens as the mold master. After release from the mold, the polishers were modified by carving

grooves in their centers to reduce center contact and help maintain the optical figure of the part during the polishing cycle. Due to constraints on the semiautomated machines at the company, the polishers were used with a cerium oxide polishing slurry instead of deionized water. Results indicate that the company can reduce overall finishing time by 50% by using full-contact molded polishers in a prepolishing stage. Due to the stiffer nature of these polishers compared to pitch, they can be used at higher pressures and spindle speeds to increase material-removal rates without degrading surface figure.

A microlens manufacturer[51] used molded bound-abrasive polishers made from the compositions and manufacturing methods described in this paper to aid in the production of $\lambda/4$ surfaces. Opticians preferred these polishers because their stiffness helped in maintaining figure.

Conclusions

We describe the development of bound-abrasive polishers using any of three commercial CeO_2 abrasives in six compositions. An epoxy is used as the binder. Useful polishing is achieved without an erosion promoter by using very high concentrations of abrasive. An erosion promoter is required to help break up the epoxy binder and expose abrasive grains at lower abrasive concentrations. Performance results are given for three polisher configurations: pellet array, ring tool, and full contact. All compositions work well, but the ones with higher CeO_2 concentration appear best for harder glasses.
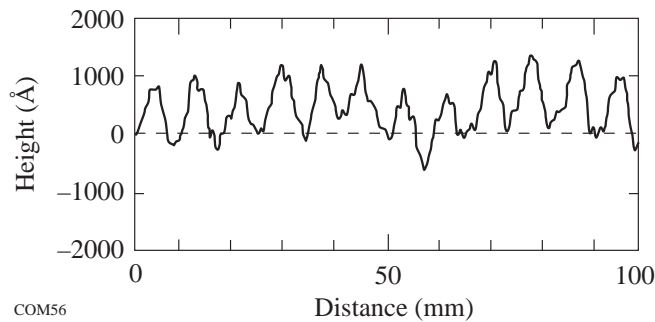

COM56

Figure 73.59
Radial profile scan showing tool marks remaining on a part surface from ring-tool-generating process.
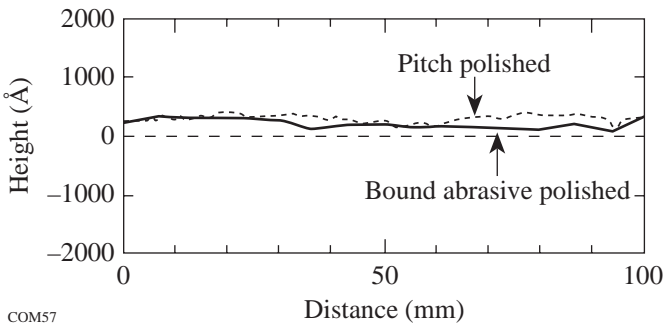

COM57

Figure 73.60
Removal of tool marks by either pitch polishing or bound-abrasive ring tool polishing.
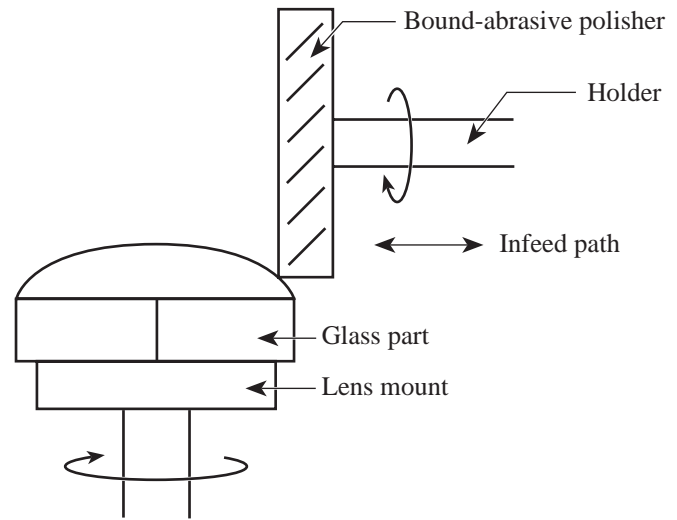

COM58

Figure 73.61
Concept for bound-abrasive contour polishing.

These polishers meet most of the performance criteria established for them. They maintain their physical integrity in aqueous coolants, under moderate loads, and at moderate to high velocities. They polish efficiently and are capable of reducing rms surface roughness of optical glasses from ~400 nm to ~1 nm in 30 min. The polishers are readily manufactured using simple process steps and have reproducible properties. They are compatible with Opticam-type CNC generating machines and can act as a fourth tool in an automatic tool changer to remove tool marks left from the last diamond ring tool grinding operation.

The issue of surface figure correction during polishing has not been successfully resolved with the bound-abrasive *ring* tool configuration, but a bound-abrasive *contour* tool mode of polishing is proposed as a solution. Finally, industry trials have demonstrated that the technology is transferable and helps to reduce overall production times when incorporated into the manufacturing process.

ACKNOWLEDGMENT

REFERENCES

1. J. C. Lambropoulos, T. Fang, P. D. Funkenbusch, S. D. Jacobs, M. J. Cumbo, and D. Golini, Appl. Opt. **35**, 4448 (1996).

2. J. C. Lambropoulos, S. D. Jacobs, B. E. Gillman, F. Yang, and J. Ruckman, "Subsurface Damage in Microgrinding Optical Glasses," to be published in the *Proceedings of the Fifth International Conference on Advances in the Fusion and Processing of Glass*, Toronto, Canada, 27–31 July 1997.

3. D. Golini and W. Czajkowski, Laser Focus World, July 1992, 146.

4. Our vendors include Scomac, Inc., Bergen, NY 14416 and H & C Tool Supply, Rochester, NY 14611, a distributor for Norton Superabrasives.

5. T. S. Izumitani, *Optical Glass*, American Institute of Physics Translation Series (American Institute of Physics, New York, 1986), Chap. 4, pp. 91–146.

6. M. J. Cumbo, D. Fairhurst, S. D. Jacobs, and B. E. Puchebner, Appl. Opt. **34**, 3743 (1995).

7. H. H. Karow, *Fabrication Methods for Precision Optics* (Wiley, New York, 1993), Chap. 5, p. 463.

8. L. M. Cook, J. Non-Cryst. Solids **120**, 152 (1990).

9. G. W. Fynn and W. J. A. Powell, in *Cutting and Polishing Optical and Electronic Materials*, The Adam Hilger Series on Optics and Optoelectronics, 2nd ed. (A. Hilger, Bristol, England, 1988), Chap. 3, p. 83.

10. N. J. Brown, Lawrence Livermore National Laboratory, Livermore, CA, UCRL-80301 (1977).

11. M. Ando *et al.*, Nanotechnology **6**, 111 (1995).

12. A. P. Bogdanov *et al.*, J. Opt. Technol. **61**, 474 (1994).

13. T. W. Drueding *et al.*, Opt. Eng. **34**, 3565 (1995).

14. D. Golini, S. Jacobs, W. Kordonski, and P. Dumas, in *Advanced Materials for Optics and Precision Structures*, edited by M. A. Ealey, R. A. Paquin, and T. B. Parsonage, Critical Reviews of Optical Science and Technology (SPIE, Bellingham, WA, 1997), Vol. CR67, pp. 251–274.

15. A. P. Denisenko *et al.*, Russian Patent No. SU 1263513 A1 (October 1986), USSR certificate No. 88333, trademark rights.

16. V. V. Rogov *et al.*, Sov. J. Opt. Technol. **56**, 33 (1989).

17. V. V. Rogov, Sov. J. Opt. Technol. **58**, 366 (1991).

18. Aquapol® product literature, Institute for Superhard Materials, Academy of Sciences of the Ukranian SSR, Kiev, Ukraine (1992).

19. V. M. Al'tshuller, S. A. Gerasimov, and V. P. Pushechnikov, J. Opt. Technol. **61**, 470 (1994).

20. S. I. Zakharov and O. V. Tapinskaya, Sov. J. Opt. Technol. **58**, 519 (1991).

21. N. L. Kudryavtseva *et al.*, Sov. J. Opt. Technol. **44**, 347 (1977).

22. N. L. Kudryavtseva, N. E. Khar'kov, and G. S. Khodakov, Sov. J. Opt. Technol. **50**, 378 (1983).

23. M. Yu. Konyukhov *et al.*, Sov. J. Opt. Technol. **58**, 798 (1991).

24. Transelco CeRite 415K, CeRite 4251, and Rhone Poulenc Cerox 1663, distributed by Universal Photonics, Inc., Hicksville, NY 11801.

25. W. Ng, B. E. Puchebner, S. D. Jacobs, J. L. Currin, B. McAvoy, D. Yungk, S. M. Gracewski, and P. D. Funkenbusch, in *Optical Fabrication and Testing Workshop*, Vol. 13, 1994 OSA Technical Digest Series (Optical Society of America, Washington, DC, 1994), pp. 114–116.

26. Epo-Tek B9131-2®, two-component "power laser adhesive," Epoxy Technology, Inc., Billerica, MA 01821.

27. Plasma alumina, low-density, microporous, hollow aluminum oxide spheres, 6-μm diameter, P.Q. Corporation, Conshohocken, PA 19428.

28. Ohara Corporation, Somerville, NJ 08876-3519.

29. Schott Glass Technologies, Inc., Duryea, PA 18642.

30. Hoya Optics, Inc., Fremont, CA 94538.

31. Fused silica, Code 7940, Corning Inc., Corning, NY 14831.

32. Schott Optical Glass Catalog (1989); Hoya Optical Glass Catalog (1989); Corning fused-silica product literature (1997).

33. R. Howard Strasbaugh (Model 6DE-DC-1), Woodbury, CT 06798.

34. Opticam® SX (renamed OptiPro 150), OptiPro Systems Inc., Ontario, NY 14519.

35. Optimax Systems, Inc., Ontario, NY 14519.

36. Catalog #21008-089, VWR Scientific Products, West Chester, PA 19380.

37. Buehler Isomet low-speed saw, Buehler Ltd., Lake Bluff, Il 60044.

38. Dow Corning RTV 3110, distributed by Wolcott-Park, Rochester, NY 14617.

39. ReleasaGen®, paintable ester mold release spray, IMS Inc., Chagrin Falls, OH 44022.

40. MX0485-7 methanol GR (anhydrous), EM Science, Gibbstown, NJ 08027.

41. B. E. Puchebner and S. D. Jacobs, in *Optical Manufacturing and Testing*, edited by V. J. Doherty and H. P. Stahl (SPIE, Bellingham, WA, 1995), Vol. 2536, pp. 256–264.

42. N. L. Kudryavtseva *et al*., Sov. J. Opt. Technol. **46**, 478 (1979).

43. Universal Photonics Product Catalog (1996), p. 14.

44. Measurements performed on a Horiba LA 900 Laser Scattering Particle Analyzer®, Horiba Instruments, Inc., Irvine, CA 92714.

45. B. E. Gillman, B. M. Reed, M. A. Atwood, J. L. Ruckman, D. J. Quesnel, T. T. Ochinero, and S. D. Jacobs, in *Optical Manufacturing and Testing II*, edited by H. P. Stahl (SPIE, Bellingham, WA, 1997), Vol. 3134, pp. 198–204.

46. Microgrit Abrasives Corporation, Westfield, MA 01086.

47. NewView 100®, white-light interferometer, 0.25 mm × 0.35 mm, areal, 20X Mirau, Zygo Corporation, Middlefield, CT 06455. Each roughness measurement reported is an average of measurements made at three sites over the part surface, avoiding center and edges.

48. LOH K-40 Coolant, LOH Optical Machinery, Inc., Germantown, WI 53022.

49. Mark IV xp phase shifting interferometer, Zygo Corporation, Middlefield, CT 06455. Using a high-pass, fast Fourier transform filter, the software options allow a line scan to be taken around the part at a fixed radius from the part center (14 mm), defined as a radial scan.

50. Moore Tool Company, Bridgeport, CT 06607.

51. Model, Inc./Integrated Endoscopy, Irvine, CA 92618.

Color Gamut of Cholesteric Liquid Crystal Films and Flakes by Standard Colorimetry

Ever since cholesteric liquid crystals (CLC's) were discovered in 1888,[1] CLC colors have been noted for their qualitative vividness and luminosity;[2] however, there have been few quantitative colorimetric studies examining CLC's as colorants. We will describe how CLC's produce color, what colorimetric studies have been done on them, and how we have extended and improved on these previous studies.

CLC molecules generally have a large aspect ratio and are often modeled as long thin rods. These rods orient along an average preferred direction in a given plane. This preferred direction, indicated by a unit vector called the director, **n**, rotates slightly from one plane to the next, forming a helix structure that may be right-handed or left-handed depending on the constituents of the molecule.[3] In a typical model (shown in Fig. 73.62) the periodicity of the helix leads to the construc-

tive interference colors of CLC's. The distance it takes the director to rotate through 360° is called the pitch P of the CLC helix. The pitch multiplied by $\bar{n}_n$, the average refractive index of the molecular layers, gives the wavelength of selective reflection, λ_0, which may range from the ultraviolet through the visible to the infrared.[4] The width of the reflected wavelength band for visible-reflecting CLC's (λ_0 ranging from 380 to 780 nm) can typically range from 10 to 100 nm.[5]

In addition to the selectivity of reflected wavelength, the CLC helix is also selective with respect to polarization. Incident light that is superimposable on the helix, i.e., of the proper wavelength *and* the proper circular polarization, will be reflected.[4] Figure 73.63 shows schematically how randomly polarized white light incident parallel to the CLC helix is selectively reflected by wavelength and polarization.

In the ideal CLC structure, there is no discontinuity in any given plane. In real CLC structures, there may be defects in molecular orientation similar to dislocations in solid crystals. The regions of perfect structure between the defects or other discontinuities are referred to as *domains*.[6] Samples that are defect-free are called *monodomain*. Samples with discontinuous domains are referred to as *polydomain*.
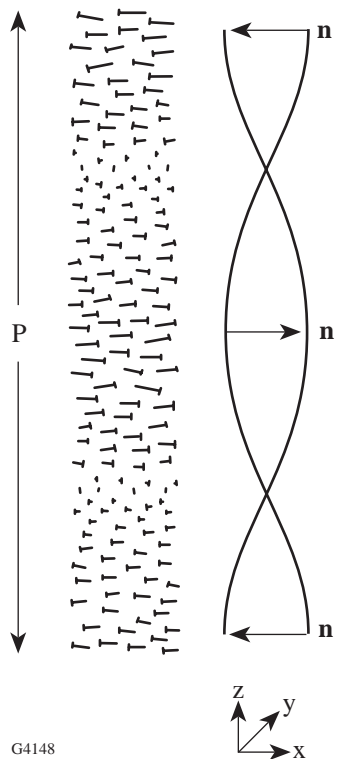

Figure 73.62
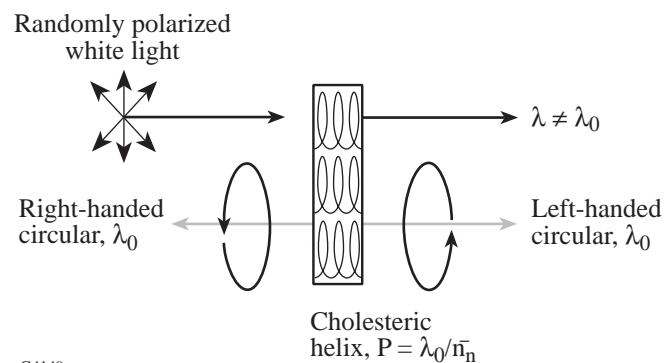Schematic model of CLC structure.

Figure 73.63
Schematic diagram of the wavelength and polarization selectivity of CLC's.

The CLC's that have been used for actively controlled color display purposes are usually polydomain: *polymer dispersed* in which the CLC molecules are found in microdroplets (~0.1 μm to ~10 μm in diameter)[7] distributed in an isotropic polymer matrix[8] and *gels* in which the CLC's form a more continuous phase with a small amount of either isotropic or anisotropic polymer to form a network that contributes to CLC molecular orientation.[9] Voltage and frequency are used to control the orientation of the CLC helices within the microdroplets or in the support polymer network; thus the ability to selectively reflect specific wavelength bands can be controlled electro-optically. Kitzerow *et al.*[10] calculated the chromaticities from the reflectivity spectra of a polymer-dispersed CLC system as a function of temperature. Although the chromaticity plot appears to indicate a color gamut covering almost the entire chromaticity diagram, many of the measurement details are unspecified, including the illuminant, the measurement angles, the actual chromaticity and luminosity values, and the voltage required for selective reflection. They indicate, however, that 2 to 3 V/μm are required to see some reflection, with intensity of the selective reflection increasing with increasing field strength to reach a plateau at 125 V/μm.

A third form of polydomain CLC that has been used for color display is called *encapsulated*. It is similar to polymer-dispersed CLC except for preparation method and has been used for decorative art[11] and for thermally controlled displays.[12] In the latter, temperature changes twist or untwist the CLC helix, shortening or lengthening the pitch and thereby controlling the reflected color. Makow and Sanders[11] used encapsulated CLC's to elucidate the qualitative color additivity of encapsulated CLC's of different colors in separate layers.

A fourth form of CLC's, *continuous film*, has been used for color filters,[13] optical notch filters,[14,15] polarization isolators,[16] and decorative art.[17] Even CLC continuous films may be polydomain unless some care is taken in the sample preparation.[18] The continuous films may be low-molecular-weight CLC's (LMCLC's) or higher-weight oligomer/polymer materials.

LMCLC's require two support substrates to promote the formation and maintenance of the helix structure across a continuous film. Makow[19] showed that, as with the encapsulated CLC's, layering different colors produces color additivity. Layering of LMCLC films, however, requires separating the layers by thin transparent sheets to prevent physico-chemical mixing that causes pitch averaging/blending.[20,21]

The oligomer/polymer type of CLC is more temperature stable than LMCLC's.[22] Oligomers/polymers can be physically manipulated at temperatures above a certain threshold called the *glass transition temperature* and retain molecular orientation below this temperature. One class of oligomers—cyclic polysiloxanes—has been particularly widely investigated.[23,24]

Cyclic polysiloxanes have been the subject of several colorimetric studies. Makow[25] demonstrated the artistic beauty of CLC polysiloxane films and showed that any spectral color could be produced by simply physico-chemically mixing a short-pitch with a long-pitch CLC. He also suggested that CLC polysiloxane films exhibit chromaticities outside the gamut of available colorants determined by Pointer,[26,27] although Makow actually compared CLC films measured in an 8/*d* geometry of an integrating sphere to Pointer's real surface colors measured by a 45/0 colorimeter. Nevertheless, he did initiate the possibility of comparing CLC's to other colorants. Makow also introduced the qualitative use of isoluminous contour lines as theoretical limits of saturation. As early as 1916, Ostwald[28] had concluded that there was some maximum attainable saturation for any given color. The reflection profile that would yield such a maximally pure or optimal color requires that the spectral reflectance have values of only zero or 100%, with no more than two discontinuous transitions between these values. The reflection profiles of most normal absorptive pigments do not meet these criteria. MacAdam[29] later used the CIE 1931 diagram to define limits of maximum attainable purity for a given luminosity Y and plotted these isoluminosity loci as contour lines within the CIE 1931 diagram. A sample with a given Y can be no purer than its associated isoluminous line.

One other chromaticity study on CLC polysiloxanes was done by Eberle *et al.*[30] They examined CLC polysiloxanes dissolved with dyes and CLC polysiloxanes on colored (paper) substrates, at many combinations of incident and reflection angles. The color additivity of a CLC and a traditional colorant (dye or paper) was quantified, but layers of CLC's of different colors were not examined. In that study, chromaticity and luminosity were shown to be simple averages of the components involved in any pair combination. Although not explicitly stated, Eberle *et al.* used the Center-of-Gravity Color-Mixing Principle.[31]

In its standard form, the Principle describes how two colors, C_1 and C_2, designated by chromaticity and luminosity coordinates $x_1 y_1 Y_1$ and $x_2 y_2 Y_2$ in the CIE 1931 chromaticity system are additively mixed. Using MacAdam's notations,[32] if

m_1 units of color C_1 are mixed with m_2 units of color C_2 (where $m_1 = Y_1/y_1$ and $m_2 = Y_2/y_2$), the chromaticity of the mixture color C_3 lies on a line connecting C_1 and C_2 on a CIE 1931 chromaticity diagram and has the following chromaticity values:

$$x_3 = \frac{m_1 x_1 + m_2 x_2}{m_1 + m_2}, \qquad (1)$$

$$y_3 = \frac{m_1 y_1 + m_2 y_2}{m_1 + m_2}, \qquad (2)$$

$$Y_3 = Y_1 + Y_2. \qquad (3)$$

The distance ratio of the line segments $\overline{C_1 C_3}$ and $\overline{C_2 C_3}$ shows the center-of-gravity relationship:

$$\frac{|C_1 C_3|}{|C_2 C_3|} = \frac{Y_2/y_2}{Y_1/y_1}. \qquad (4)$$

If each of the two colors occupies a discrete fractional area designated A_1 or A_2 respectively, Eqs. (1)–(3) may be written as

$$x_3 = \frac{A_1 m_1 x_1 + A_2 m_2 x_2}{A_1 m_1 + A_2 m_2}, \qquad (5)$$

$$y_3 = \frac{A_1 m_1 y_1 + A_2 m_2 y_2}{A_1 m_1 + A_2 m_2}, \qquad (6)$$

$$Y_3 = A_1 Y_1 + A_2 Y_2. \qquad (7)$$

Since the CLC's with dyes or the CLC's on colored substrates occupied the same area, the form of the Center-of-Gravity Color-Mixing Principle used by Eberle *et al.* invoked Eqs. (1)–(3) and showed good agreement with experiment for their systems. They concluded that the CLC contributed to the measured color significantly near specular geometries (illumination angle ≈ reflection angle), but otherwise the substrate color dominated. This contribution of a colored substrate to the measured color of a CLC confirmed quantitatively what earlier artistic[17] work with CLC's had found: a black backing, contributing no color to the CLC appearance, produces truer CLC color effects.

To date, no *standard* colorimetry has been conducted on continuous CLC films or on discrete CLC domains, that is, at 45/0 and such that all conditions of measurement are explicitly known. No colorimetric experiment has quantified the color additivity of layering CLC's. No deterministic method has been developed for the color additivity of discrete CLC domains. No comparison has been made of CLC's as colorants and traditional absorptive colorants under similar conditions of measurement.

In this article, we address each of these issues. The CLC's used are cyclic polysiloxanes in two forms: continuous film and a new form called *flakes*. These two forms allow us to compare the color of CLC films to other colorants and to compare the large domains of a continuous film to the small domains of flakes. Further, flakes dispersed in a host will serve as a model for polymer-dispersed, gel, and encapsulated CLC forms. Principally, this article will show how the color gamut of CLC's can be affected by the form of the CLC, the size of the domains, and the method of mixing CLC's. Other aspects of CLC colorimetry including CLC flake production, polarization issues, the shape of the selective reflection profile, mixing CLC's with traditional absorptive dyes, and CLC's modeled as optimal colors are addressed elsewhere.[33]

Sample Preparation and Measurement Methods

The liquid crystal phase of the CLC cyclic polysiloxanes used in this study exists between 50°C and 200°C. At temperatures below this range, the molecular orientation is "frozen." At temperatures higher than this range, these materials are isotropic, noncolored liquids that decompose in the presence of oxygen. Three polysiloxanes were used: CLC670 (red reflecting), CLC535 (green reflecting), and CLC450 (violet reflecting). The number refers to λ_0, the wavelength in nanometers that is the center of the reflected wavelength band.

Continuous films are prepared by a process referred to as "knife-coating." A sample of CLC on a microscope slide or silicon wafer is heated to ~130°C. Another microscope slide is used on edge as a "knife" to spread the CLC into a thin film ~30 μm thick. This process produces the proper molecular orientation that results in brilliant reflective color.

A second form of CLC is produced by knife-coating continuous films on silicon wafers[34] and submerging them into liquid nitrogen. The films fracture into smaller pieces called *flakes*.[35] Flakes are collected by rinsing into a methanol slurry. The slurry is washed with methanol through a stack of sieves[36] into four size-groups: 90 to 180 μm, 45 to 90 μm, 20 to 45 μm, and <20 μm. The average refractive indices of the unfractured films are measured on an Abbe refractometer.[37] The flakes made from the films are mixed into a slurry (12%±3% by

weight) with an enamel, filtered[38] from a commercially available paint,[39] providing a very closely index-matched, transparent colorless host. This enamel-and-flake slurry is painted into a 1-cm × 2-cm color patch on black toner paper from a laser printer.[40] A schematic diagram of the typical orientation of CLC flakes brushed onto paper is shown in Fig. 73.64.
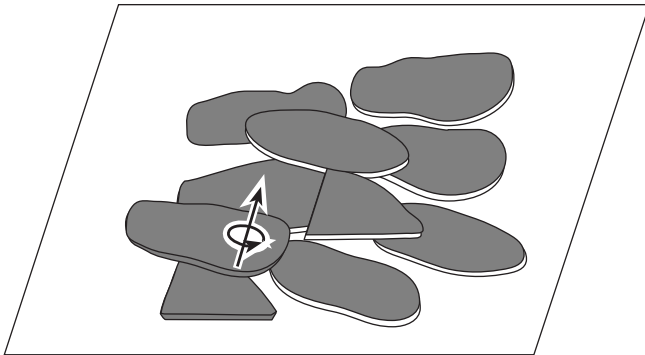
G4150

Figure 73.64
Schematic diagram of CLC flakes painted onto paper.

The chromaticity and luminosity (x, y, Y) of CLC samples were measured with two colorimeters, each using the CIE 1931 basis with D_{65} illuminant. CLC flake samples in enamel painted directly onto black toner paper were measured using the Gretag SPM 100-II colorimeter.[41] Due to the motor action of the Gretag detection head, the measurement of slides was unstable so CLC films on microscope slides with black toner paper backing were measured using the ColorTron II colorimeter.[42] Each sample was measured in five evenly spaced spots along the length of the color patch. These values were averaged, and a standard deviation due to variation across the sample was determined. Inter-instrument agreement was within this standard deviation.

The color of CLC's is angle dependent, following a Bragg-like law;[43] however, since most commonly available colorimeters use the 45/0 geometry, this article will address color effects for this fixed geometry only.

Experiments and Results

Since this article deals primarily with the nature of the color gamut of CLC's, we will discuss the six main features we have elucidated regarding techniques to access regions of CIE 1931 x, y, Y color space with CLC's as the colorants:

1. The Color Gamut of the Three Original CLC Films

Table 73.X lists the x, y, Y values and Fig. 73.65 illustrates the chromaticity positions of the original three CLC films. Geometric color additivity on the CIE 1931 chromaticity diagram ensures that an additive mixture of any two points yields a third chromaticity point *on* the line connecting the two components.[31] Using only the original three CLC's as continuous films, the chromaticities we can access are limited to those *on* the triangle of Fig. 73.65.

Table 73.X: The measured chromaticities and luminosities, x, y, Y, of the three original CLC polysiloxane films.

CLC ID	x	y	Y
CLC670	0.5153	0.3459	8.83
CLC535	0.2306	0.4803	26.26
CLC450	0.1777	0.0777	4.33
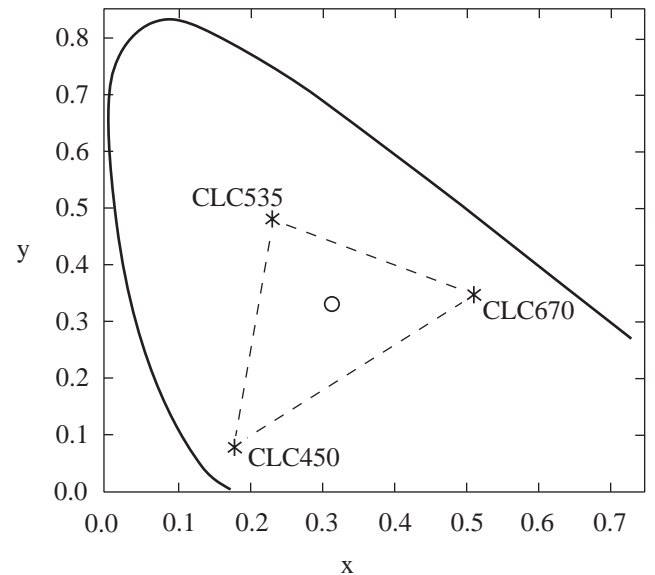
G4151

Figure 73.65
Chromaticities of the three original CLC polysiloxanes as knife-coated films on microscope slides with black toner paper backing.

2. Color Additivity by Layering

Unlike traditional inks in which absorption produces subtractive color combination of layers, CLC's are reflective.

Provided that each layer allows reflection from other layers (i.e., each reflecting layer is transparent to the others), the color mixing of CLC layers is *additive*. The knife-coated slides of CLC670, CLC535, and CLC450 were stacked in pairs with black toner paper at the bottom. Chromaticity and luminosity were recorded using the ColorTron II. Table 73.XI lists the results and Fig. 73.66 illustrates that the additive combination does fall on the line connecting the two components. The CIE color gamut is still limited to the triangle formed by CLC670, CLC535, and CLC450.

The color additivity was not a simple 1:1 averaging of the two layers as Eberle *et al.*[30] had found for CLC's layered with colored substrates. In fact, we found a clear difference in chromaticity of layered CLC's based on stacking order. For example, "670 over 450" (meaning the slide with CLC670 was on top and the slide with CLC450 was underneath) is closer to pure CLC670 than "450 over 670," which is closer to pure CLC450. These layers were made by placing the microscope slides together, both face up. This resulted in a layer-to-layer separation of one microscope-slide thickness. The presence of the microscope slide reduced the intensity of the light reaching the detector. The 45/0 geometry of the ColorTron II is designed to illuminate the sample *at* the measurement aperture. The 1-mm-thick microscope slide, displaced one layer from the ideal position, reducing incident intensity and therefore reflected intensity. An alternate way of stacking was to place the CLC layers in contact but separating both layers from the colorimeter by the thickness of a slide. There was virtually no difference in chromaticities from those of Table 73.XI using this alternate method of stacking. The combination chromatic-

ity point fell closer to whichever sample was closest to the colorimeter, even when both films were subjected to the same displacement error from the measurement aperture. This indicated that the upper layer prevented the full reflection of the lower layer due to an imperfect helical structure and some overlap of the reflection bands.
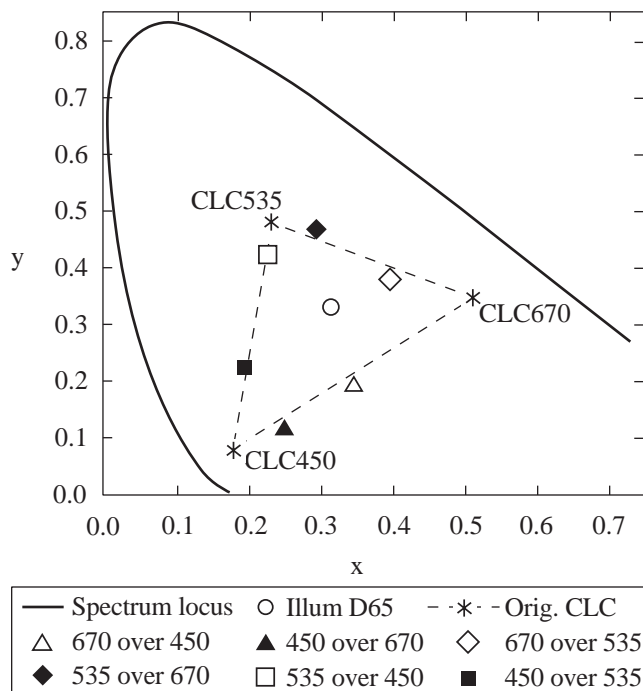
Figure 73.66
Chromaticity plot of layered CLC polysiloxane films.

Table 73.XI: *x, y, Y* of layered CLC polysiloxane films.

Sample		x	y	Y
Upper	Lower			
---	CLC670	0.5153	0.3459	8.83
---	CLC535	0.2306	0.4803	26.26
---	CLC450	0.1777	0.0777	4.33
CLC670	CLC535	0.3972	0.3839	16.81
CLC535	CLC670	0.2958	0.4659	30.84
CLC670	CLC450	0.3446	0.1984	9.69
CLC450	CLC670	0.2491	0.1264	8.67
CLC535	CLC450	0.2257	0.4240	27.77
CLC450	CLC535	0.1953	0.2320	18.21

3. New Hues by Mixing the Original CLC Polysiloxanes

In this section, we extend Makow's earlier qualitative work[25] by quantifying the chromaticities and luminosities of hues produced by physico-chemically mixing the original CLC polysiloxanes.

Two techniques were used to mix the polysiloxanes. The first technique was simply to place two CLC polysiloxanes in proximity, elevate the temperature to ~130°C, and stir them together with a microspatula. A second technique, which ensured more complete, homogeneous mixing, was mutual dissolution of the two components in dichloromethane, stirring, and evaporation. The resulting mixtures from this second technique were then prepared as knife-coated slides. The chromaticities and luminosities are listed for various weight ratios in Table 73.XII and illustrated in Fig. 73.67. Each mixture has produced a new chromaticity outside the original triangular color gamut, effectively increasing the region of color space that can be accessed by the CLC polysiloxane films.

4. Color Gamut of CLC Flakes Made from the Three Original CLC Polysiloxanes

In addition to using the continuous-film form of CLC's, we have also prepared samples of CLC flakes from each of the four different size-groups.

The *x,y,Y* measurements for the CLC flake colorant samples are listed in Table 73.XIII and illustrated in Fig. 73.68. For each of the original materials, decreasing flake size leads to more desaturation of the hue, finally allowing access to the chromaticities *within* the original triangular color gamut. As flake size decreases, the orientation of the periodic molecular planes, responsible for the color, becomes more and more disordered. As a result, the reflection spectrum of CLC flake

samples becomes wider and more shallow. This is consistent with the desaturation seen for encapsulated CLC's[20] whose helices are disordered due to the presence of the confining wall.

5. Mixing CLC Flakes of Different Colors

Layering CLC films produced an additive color by simultaneous reflection. The use of CLC flakes makes it possible to invoke another kind of color additivity: spatial averaging. By mixing two different colors of flakes and painting the mixture,

G4153
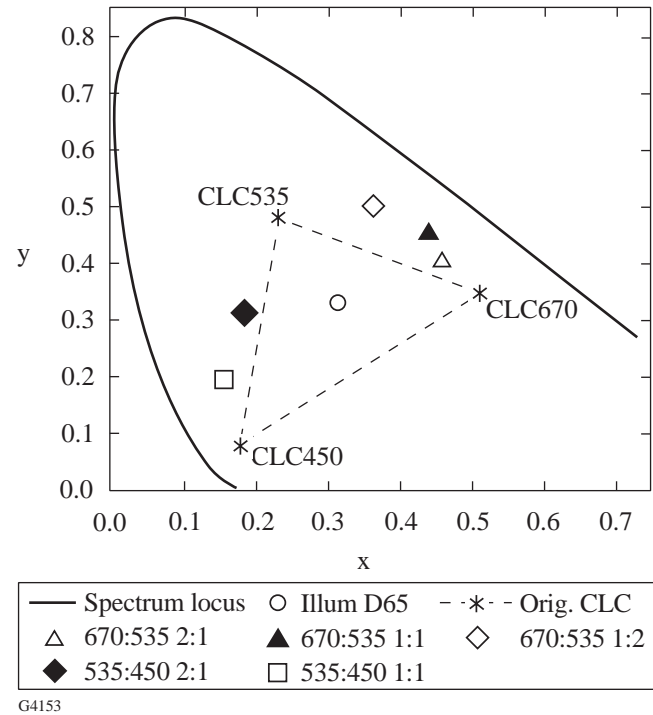
Figure 73.67
Chromaticity plot of CLC polysiloxane mixtures.

Table 73.XII: *x,y,Y* of CLC polysiloxane mixtures. Mixtures of pairs are listed with their mass ratios.

Sample	*x*	*y*	*Y*
CLC670	0.5168	0.3541	11.83
CLC535	0.2270	0.4738	24.69
CLC450	0.1775	0.0777	4.19
CLC670:CLC535::2:1	0.4582	0.4088	10.26
CLC670:CLC535::1:1	0.4409	0.4580	35.99
CLC670:CLC535::1:2	0.3607	0.5057	31.19
CLC535:CLC450::2:1	0.1822	0.3086	18.58
CLC535:CLC450::1:1	0.1562	0.1920	10.55

a color mosaic is produced. The resultant chromaticity of such a color mosaic can be determined by the fractional-area-weighted version of the Center-of-Gravity Color-Mixing Principle. For CLC flakes, instead of using the fractional areas, which are difficult to determine, we used the fractional masses of each type of flake in the mixture as the A_1 and A_2 factors in Eqs. (5)–(7). Provided the mixture is made with flakes from the same size-group so that the flakes behave similarly, the surface coverage by each color corresponds to the fractional masses and in turn follows the Center-of-Gravity Color-Mixing Principle very well.

Mixtures were made of CLC670, CLC535, and CLC450, in pairs, in weight ratios of 1:0, 3:1, 1:1, 1:3, and 0:1, for each of the flake size-groups separately. Weighting the chromaticities of the unmixed flake samples by these fractional masses, the x,y,Y of the mixtures were predicted and compared to the measured values. The comparison was made by converting the x,y,Y measurement to CIEL*a*b* coordinates through ColorTron II software. The color-difference function[44] ΔE^*_{ab} was also calculated for each predicted/measured pair, with a difference of 1 ΔE^*_{ab} unit corresponding approximately to a just-discernible color difference. The ΔE^*_{ab} values for each size-group were then averaged. The averages and ranges are shown in Fig. 73.69.
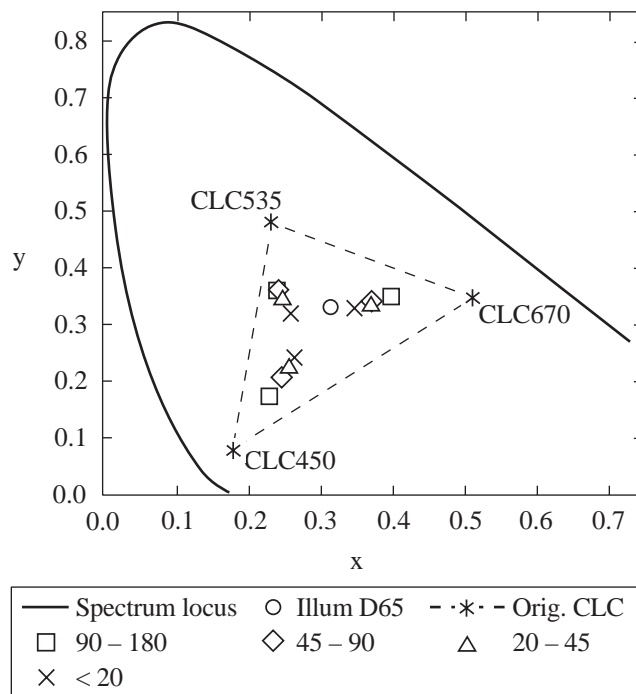
G4154

Figure 73.68
Chromaticity of CLC flakes of various size-groups (indicated in microns).

Table 73.XIII: x,y,Y of CLC flakes as a function of size. The film samples are knife-coated microscope slides measured with the ColorTron II. The flake samples are in enamel on black toner paper measured with the Gretag SPM 100-II.

CLC ID	Size	x	y	Y
CLC670	Film	0.5153	0.3459	8.83
	90 to 180 μm	0.3961	0.3504	5.73
	45 to 90 μm	0.3770	0.3468	5.86
	20 to 45 μm	0.3710	0.3443	6.85
	<20 μm	0.3510	0.3345	6.67
CLC535	Film	0.2306	0.4803	26.26
	90 to 180 μm	0.2402	0.3603	7.43
	45 to 90 μm	0.2419	0.3615	9.16
	20 to 45 μm	0.2472	0.3507	8.25
	<20 μm	0.2580	0.3241	7.27
CLC450	Film	0.1777	0.0777	4.33
	90 to 180 μm	0.2306	0.1823	3.73
	45 to 90 μm	0.2460	0.2111	3.86
	20 to 45 μm	0.2563	0.2315	4.51
	<20 μm	0.2629	0.2473	4.86

The 20- to 45-μm size-group had the lowest ΔE^*_{ab} values, i.e., the best agreement with the center-of-gravity predictions. This is attributed to an optimization of the two factors required for the center-of-gravity principle to hold:

(a) The flakes must be oriented with the normal to the periodic molecular planes normal to the paper. This ensures that all the flakes contribute their full reflection profiles to the combination color. Brushing accomplished this readily except for the <20-μm flakes. Under a microscope the latter appeared essentially cube-like with no preferred orientation.

(b) The flakes must completely hide the paper support. Samples of the two largest size-groups did not completely cover the measured area, whereas the two smaller size-groups covered it readily. Since the chromaticity of the exposed paper support was not included in the center-of-gravity calculations based on fractional masses, surface hiding was essential.

Figure 73.70 shows the measured x,y,Y values listed in Table 73.XIV for the 20- to 45-μm size-group. The Y values were very close in magnitude so the distribution of chromaticity points gives approximately the right spacing for 1:0, 3:1, 1:1, 1:3, and 0:1 mass-ratio mixtures for each color pair.

CLC flake mixtures behave like pixels or pointillist painting. The flakes may be mixed in any proportion, unlike films that can only be layered. Even the layering does not produce a 1:1 weighting of chromaticities as we showed earlier. So use of CLC flakes as colorants allows a range of hues, a range of saturation, and a deterministic method for predicting the resulting chromaticity of a quantifiable mixture. Further, CLC flakes in mixtures of red with violet can be used to predictably produce the nonspectral, that is, purple to magenta, region of x,y,Y color space. Finally, CLC flakes do not require elevated temperature or high voltages for painting since the reflecting molecular orientation is already present and "frozen in" at room temperature.

6. CLC Films Compared to Traditional Colorants

In this section, we compare CLC colors to some representative dyes, paints, and inks, i.e., traditional absorptive colorants. We compare these traditional colorants to the most saturated form of CLC, the continuous film, noting that CLC flakes are more versatile, if less saturated, than films.

The CLC film samples included in this comparison are knife-coated samples of CLC670, CLC535, CLC450, and the mixtures CLC670:CLC535::2:1, CLC670:CLC535::1:1, CLC670:CLC535::1:2, CLC535:CLC450::2:1, and CLC535:CLC450::1:1.

G4155
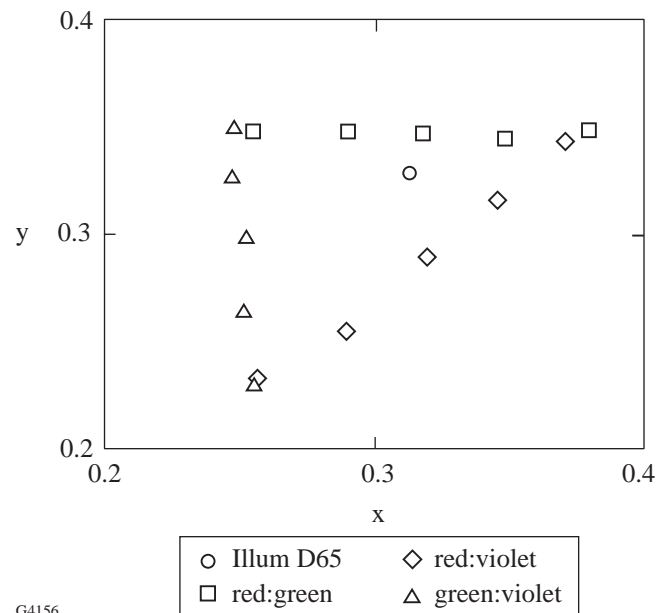
Figure 73.69
ΔE^*_{ab} averages and ranges for measured versus predicted chromaticity of CLC flakes mixtures.

G4156

Figure 73.70
CIE diagram illustrating the Center-of-Gravity Color-Mixing Principle for 20- to 45-μm CLC flakes.

The colorants selected for comparison to these CLC films are (a) commercially available enamel-based paints[45] selected for their subjective vividness, (b) color samples from the Optical Society of America[46] selected for their subjective hue similarity to CLC film samples, and (c) three dyes: sudan III[47] (appears red), malachite green oxalate[48] (appears green), and crystal violet[49] (appears violet). Each dye was mixed with a nonchromatic polysiloxane, CLC850 ($\lambda_0 = 850\pm100$ nm), in a 2% by weight mixture. After mutual dissolving in dichloromethane, each dye/CLC850 mix was knife-coated onto a slide. Since CLC850 reflects only near-infrared at normal incidence and is only pale pink, very weakly saturated at 45/0, it is essentially invisible to standard colorimeters (Gretag range = 380 to 730 nm; ColorTron II range = 390 to 700 nm). CLC850 offers the advantage of providing a host for each dye without any significant chromatic contribution.

The CLC films were measured on the ColorTron II under the CIE 1931 D_{65} basis, using black toner paper backing. The dye samples were measured with the same instrument and instrumental settings but with white paper backing. The OSA samples are ink on cardboard, uniquely identified by a sequence of numbers[50,51] no longer in general use (approximately correspondent with brightness, yellowness-blueness, magenta-green-ness). The paint samples were prepared by brushing onto microscope slides until the coating was opaque to the naked eye under ambient room light. They were measured with the same instrument and instrumental settings as the other samples and used a white paper backing behind the slide.

The chromaticities, luminosities, and purities are listed in Table XV. Since CLC's have a definite bandwidth, they can never be as pure as the monochromatic points comprising the spectrum locus. A more practical measurement of purity P is to take the following ratio: the distance from the white point (the D_{65} chromaticity) to the chromaticity of the sample and the distance from the white point along the same line to the isoluminous (same Y value) contour line.

Table 73.XIV: Measured versus calculated x, y, Y of flake mixtures of size-group 20 to 45 μm. The abbreviations listed under "color" are R ≡ CLC670, G ≡ CLC535, and V ≡ CLC450 with the approximate mass ratios. The actual masses are listed and were used as the A_1 and A_2 values in Eqs. (5), (6), and (7) of the Center-of-Gravity Color-Mixing Principle.

Color	Mass (g) Color 1	Mass (g) Color 2	Meas x	Meas y	Meas Y	Calc x	Calc y	Calc Y	ΔE^*_{ab}
R			0.3710	0.3443	6.85				
V			0.2563	0.2315	4.51				
R:V 1:1	0.0051	0.0050	0.3197	0.2895	5.27	0.3148	0.2891	5.69	1.43
R:V 1:3	0.0042	0.0126	0.2892	0.2556	4.68	0.2854	0.2601	5.10	2.12
R:V 3:1	0.0046	0.0015	0.3454	0.3169	6.19	0.3432	0.3170	6.27	0.49
G			0.2472	0.3507	8.25				
V			0.2556	0.2300	4.52				
G:V 1:1	0.0049	0.0049	0.2517	0.2990	6.48	0.2510	0.2958	6.39	0.80
G:V 1:3	0.0027	0.0081	0.2512	0.2638	5.80	0.2532	0.2644	5.45	1.11
G:V 3:1	0.0100	0.0033	0.2469	0.3270	8.18	0.2490	0.3246	7.32	2.48
R			0.3794	0.3493	7.75				
G			0.2546	0.3488	6.79				
R:G 1:1	0.00862	0.00859	0.3179	0.3478	7.62	0.3212	0.3491	7.27	1.00
R:G 1:3	0.00514	0.01504	0.2896	0.3483	6.95	0.2896	0.3489	7.03	0.26
R:G 3:1	0.03152	0.01066	0.3484	0.3452	6.84	0.3508	0.3492	7.51	1.86

All the x, y, Y values are plotted for comparison in Fig. 73.71 with a dotted line representing the color gamut provided by CLC polysiloxane films.

Several observations from Table 73.XV and Fig. 73.71 are worth noting. First, we note that there are existing pigments more saturated and less saturated than CLC films. Overall, then, CLC films are not limiting cases in either direction of color purity. For commercial graphic arts applications, this means that CLC films as colorants are as capable of color depth as any other intermediate-saturation colorant.

Secondly, CLC films are more luminous than comparably hued pigments in the blue-violet region of the color gamut. In the lower left "corner" of the CIE diagram in Fig. 73.71, the purities are very similar (86%–96%). The chromaticity points are also very close for the CLC450 film, crystal violet dye, and

dark blue paint. The CLC film, however, has a Y value four times greater than the dye and 24 times greater than the paint. Recall that the units for tristimulus values such as Y are lumens/m^2/sr = candelas/m^2—in other words, units of luminous flux. The blue-violet CLC film has more light reflecting from it than do pigments of comparable hue. CLC films reflecting in the red-to-green spectral range may show luminosity values comparable to similarly hued pigments; however, the purity values are not as similar. For comparable luminosities, red-to-green pigments are, in general, more saturated than red-to-green CLC films.

Summary

We have shown that CLC films and flakes can be measured by standard colorimetry. The color gamut of CLC's as colorants, measured by standard techniques, may be accessed by four techniques: layering of continuous films, physico-chemical

Table 73.XV: Chromaticities and purities of CLC films compared to other colorants. The purities are calculated with respect to the isoluminous curve corresponding to each sample's Y value.

Sample Form	Sample ID	Visual color	x	y	Y	P (%)
CLC	670	red	0.5043	0.3462	9.39	59
	670:535::2:1	gold	0.4582	0.4089	8.83	63
	670:535::1:1	butterscotch	0.4409	0.4580	35.99	73
	670:535::1:2	yellow-green	0.3607	0.5057	31.19	64
	535	green	0.2257	0.4732	24.31	37
	535:450::2:1	turquoise	0.1822	0.3086	18.58	56
	535:450::1:1	light blue	0.1562	0.1920	10.55	76
	450	violet	0.1793	0.0778	4.07	88
Dyes	sudan III	red	0.6836	0.3130	4.13	99
	malachite	green	0.1643	0.3902	3.68	52
	crystal violet	violet	0.1748	0.0341	0.94	96
Testor's gloss paints	1103	red	0.6445	0.3170	8.01	89
	1114	yellow	0.4961	0.4646	56.14	90
	1124	green	0.2335	0.6501	9.51	73
	1111	dark blue	0.1696	0.0688	0.17	86
OSA color samples	(-1,1,-1)	pink	0.4362	0.3113	24.86	48
	(-1,5,-5)	orange	0.4753	0.3833	26.64	59
	(-1,5,5)	green	0.2991	0.4917	28.72	43
	(-1,-5,3)	blue	0.2150	0.2387	22.88	54
	(-1,-5,-1)	violet	0.2698	0.2381	22.03	47
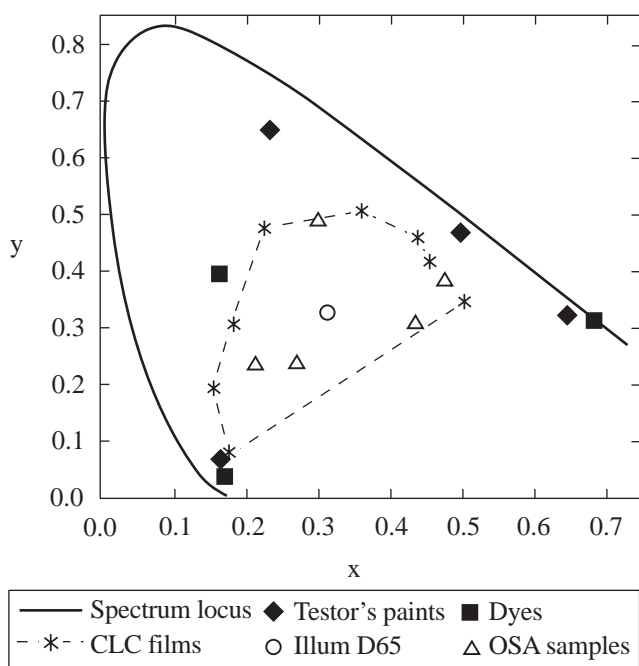
G4157

Figure 73.71
Chromaticity plot of CLC films, dyes, paints, and OSA ink samples.

mixing of CLC's, varying the size of the CLC domains, and spatial averaging of mixed domains. Layering and physico-chemical mixing produce new hues, but these new hues can be determined only empirically. The Center-of-Gravity Color-Mixing Principle allows the deterministic prediction of hues of mixed flakes based on their fractional masses in the mixture. Despite their angle dependence and selective polarization behavior, the color gamut of CLC's can be successfully examined with standard colorimetry.

ACKNOWLEDGMENT

REFERENCES

1. F. Reinitzer, Monatsch. Chem. **9**, 421 (1888).
2. Y. Charnay, Leonardo **15**, 219 (1982).
3. C. W. Oseen, Trans. Faraday Soc. **29**, 883 (1933).
4. Hl. De Vries, Acta Cryst. **4**, 219 (1951).
5. L. B. Leder and D. Olechna, Opt. Commun. **3**, 295 (1971).
6. C. Viney and C. M. Dannels, Mol. Cryst. Liq. Cryst. **196**, 133 (1991).
7. P. S. Drzaic, *Liquid Crystal Dispersions*, Series on Liquid Crystals, Vol. 1 (World Scientific, Singapore, 1995), p. 12.
8. H.-S. Kitzerow, J. Rand, and P. P. Crooker, J. Phys. II France **2**, 227 (1992).
9. R. A. M. Hikmet and B. H. Zwerver, Liq. Cryst. **12**, 319 (1992).
10. H.-S. Kitzerow, P. P. Crooker, and G. Heppke, Liq. Cryst. **12**, 49 (1992).
11. D. M. Makow and C. L. Sanders, Nature **276**, 48 (1978).
12. R. M. Christie and D. Bryant, J. Oil and Colour Chemists' Assoc. **78**, 332 (1995).
13. N. Häberle *et al.*, in *1991 International Display Research Conference* (IEEE, Piscataway, NJ, 1991), pp. 57–59.
14. S. Ishihara *et al.*, Polymer **29**, 2141 (1988).
15. M. L. Tsai, S. H. Chen, and S. D. Jacobs, Appl. Phys. Lett. **54**, 2395 (1989).
16. S. D. Jacobs, K. A. Cerqua, K. L. Marshall, A. Schmid, M. J. Guardalben, and K. J. Skerrett, J. Opt. Soc. Am. B. **5**, 1962 (1988).
17. R. Lemberg, Leonardo **2**, 45 (1968).
18. J. Adams, W. Haas, and J. Wysocki, Mol. Cryst. Liq. Cryst. **8**, 9 (1969).
19. D. M. Makow, Appl. Opt. **19**, 1274 (1980).
20. D. Makow, Leonardo **15**, 257 (1982).
21. S. Nakano, U.S. Patent No. 5,508,068 (16 April 1996).
22. S.-H. Chen, H. Shi, J. C. Mastrangelo, and J. J. Ou, Prog. Polym. Sci. **21**, 1211 (1996).
23. H. Finkelmann *et al.*, Makromol. Chem. **179**, 829 (1978).
24. F.-H. Kreuzer *et al.*, Mol. Cryst. Liq. Cryst. **199**, 345 (1991).
25. D. Makow, Color Res. Appl. **11**, 205 (1986).
26. D. Makow, Mol. Cryst. Liq. Cryst. **123**, 347 (1985).

27. M. R. Pointer, Color Res. Appl. **5**, 145 (1980).

28. W. Ostwald, Physik. Zeits. **17**, 328 (1916) cited in D. L. MacAdam, J.O.S.A. **25**, 249 (1935).

29. D. L. MacAdam, J.O.S.A. **25**, 249 (1935).

30. H.-J. Eberle, A. Miller, and F.-H. Kreuzer, Liq. Cryst. **5**, 907 (1989).

31. R. W. G. Hunt, *Measuring Colour*, 2nd ed. (Ellis Horwood, London, 1995), pp. 66–68.

32. D. L. MacAdam, *Color Measurement: Theme and Variations*, 2nd rev. ed., Springer Series in Optical Sciences, Vol. 27 (Springer-Verlag, Berlin, 1985), p. 49.

33. E. M. Korenic, "Colorimetry of Cholesteric Liquid Crystals," Ph.D. thesis, University of Rochester, 1997.

34. Silicon epiprime, 100-mm-diam wafers, Wacker Siltronic Corporation, Portland, OR.

35. S. M. Faris, U.S. Patent No. 5,364,557 (15 November 1994).

36. Newark Wire Cloth Company, Newark, NJ 07104.

37. Bellingham and Stanley Model 60/HR refractometer, Bellingham and Stanley Ltd., North Farm Industrial Estate, Tunbridge Wells, Kent TN2 3EY, England.

38. Millex®-FG$_{13}$ filter unit, 0.2 μm, Millipore Corporation, Bedford, MA 01730.

39. Testor's gloss enamel gold (#1144), The Testor's Corporation, Rockford, IL 61104.

40. Hewlett Packard LaserJet 4m, Hewlett Packard. The printing options used were the default settings: resolution = 300 dpi, halftone frequency = 60.0, and halftone angle = 45.0.

41. Gretag Imaging, Chicopee, MA 01022.

42. LightSource, Larkskpur, CA 94939 through Lucid Technologies, Inc., Henrietta, NY 14467.

43. J. L. Fergason, Mol. Cryst. **1**, 293 (1966).

44. G. Wyszecki and W. S. Stiles, *Color Science: Concepts and Methods, Quantitative Data and Formulae*, 2nd ed. (Wiley, New York, 1982), p. 829.

45. Testor's gloss enamel, red (#1103), yellow (#1114), green (#1124), and dark blue (#1111), The Testor's Corporation, Rockford, IL 61104.

46. Provided by Dr. D. L. MacAdam, The Institute of Optics, University of Rochester, Rochester, NY 14623.

47. Sudan III, CAS #85-86-9, certified, dye content 88%, C.I. 26100, Solvent Red 23, Aldrich Catalog #19,811-0, Aldrich Chemical Company, Milwaukee, WI 53223.

48. Malachite green oxalate, CAS #2437-29-8, certified, dye content 98%, Basic Green 4, Aldrich Catalog #86,121-9, Aldrich Chemical Company, Milwaukee, WI 53223.

49. Crystal violet, CAS #548-62-9, C.I. 42555, Basic Violet 3, No. C-3886, Sigma Chemical Company, St. Louis, MO 63178.

50. G. Wyszecki and W. S. Stiles, *Color Science: Concepts and Methods, Quantitative Data and Formulae*, 2nd ed. (Wiley, New York, 1982), Chap. 6.

51. D. L. MacAdam, *Color Measurement: Themes and Variations*, 2nd rev. ed., Springer Series in Optical Sciences, Vol. 27 (Springer-Verlag, New York, 1985), pp. 165–174. Optical Society of America color subcommittee uniform color scales (L, j, g) introduced in 1974.

Publications and Conference Presentations

Publications

W. R. Donaldson, E. M. R. Michaels, K. Akowuah, and R. A. Falk, "Integrated Circuit Tester Using Interferometric Imaging," in *Electrochemical Society Proceedings Volume 97–12*, edited by P. Rai-Choudhury, J. Benton, D. Schroder, and T. J. Shaffner (The Electrochemical Society, Pennington, NJ, 1997), pp. 171–176.

B. E. Gillman, B. M. Reed, M. A. Atwood, J. L. Ruckman, D. J. Quesnel, T. T. Ochinero, and S. D. Jacobs, "Application of Coolants in Deterministic Microgrinding of Glass," in *Optical Manufacturing and Testing II*, edited by H. P. Stahl (SPIE, Bellingham, WA, 1997), Vol. 3134, pp. 198–204.

D. Golini, S. Jacobs, W. Kordonski, and P. Dumas, "Precision Optics Fabrication Using Magnetorheological Finishing," in *Advanced Materials for Optics and Precision Structures,* edited by M. A. Ealey, R. A. Paquin, and T. B. Parsonage, Critical Reviews of Optical Science and Technology (SPIE, Bellingham, WA, 1997), Vol. CR67, pp. 251–274.

S. D. Jacobs, F. Yang, E. M. Fess, J. B. Feingold, B. E. Gillman, W. I. Kordonski, H. Edwards, and D. Golini, "Magneto-rheological Finishing of IR Materials," in *Optical Manufacturing and Testing II*, edited by H. P. Stahl (SPIE, Bellingham, WA, 1997), Vol. 3134, pp. 258–269.

J. C. Lambropoulos, B. E. Gillman, Y. Zhou, S. D. Jacobs, and H. J. Stevens, "Glass-Ceramics: Deterministic Micro-grinding, Lapping, and Polishing," in *Optical Manufacturing and Testing II*, edited by H. P. Stahl (SPIE, Bellingham, WA, 1997), Vol. 3134, pp. 178–189.

C. J. McKinstrie, J. S. Li, and A. V. Kanaev, "Near-Forward Stimulated Brillouin Scattering," Phys. Plasmas **4**, 4227 (1997).

D. D. Meyerhofer, "High-Intensity-Laser-Electron Scattering," IEEE J. Quantum Electron. **33**, 1935 (1997).

B. Nodland and C. J. McKinstrie, "Propagation of a Short Laser Pulse in a Plasma," Phys. Rev. E **56**, 7174 (1997).

S. Papernov and A. W. Schmid, "Localized Absorption Effects During 351-nm, Pulsed Laser Irradiation of Dielectric Multi-layer Thin Films," J. Appl. Phys. **82**, 5422 (1997).

B. Yaakobi, F. J. Marshall, D. K. Bradley, J. A. Delettrez, R. S. Craxton, and R. E. Epstein, "Novel Methods for Diagnosing Mixing and Laser-Fusion Target Performance Using X-Ray Spectroscopy of an Embedded Titanium Layer," Opt. Photonics News, 42 (December 1997).

Forthcoming Publications

S. Alexandrou, C.-C. Wang, M. Currie, R. Sobolewski, and T. Y. Hsiang, "Characterization of Coplanar Transmission Lines at Subterahertz Frequencies," to be published in IEEE Transactions on Microwave Theory and Techniques.

E. L. Alfonso, S.-H. Chen, R. Q. Gram, and D. R. Harding, "Properties of Polyimide Shells Made Using Vapor Phase Deposition," to be published in the Journal of Materials Research.

A. Babushkin, W. Seka, S. A. Letzring, W. Bittle, M. Labuzeta, M. Miller, and R. G. Roides, "Multicolor Fiducial Laser for Streak Cameras and Optical Diagnostics for the OMEGA Laser System," to be published in the Proceedings of the 22nd International Congress on High-Speed Photography and Photonics, Santa Fe, NM, 27 October–1 November 1996.

R. Betti, "Beta Limits for the $N = 1$ Mode in Rotating-Toroidal-Resistive Plasmas Surrounded by a Resistive Wall," to be published in Physics of Plasmas.

R. Betti, V. N. Goncharov, R. L. McCrory, and C. P. Verdon, "Feedthrough and Dynamic Stabilization in Convergent Geometry," to be published in the Proceedings of the Thirteenth International Conference on Laser Interactions and Related Plasma Phenomena (LIRPP), Monterey, CA, 13–18 April 1997.

R. Betti, V. N. Goncharov, R. L. McCrory, and C. P. Verdon, "Growth Rates of the Ablative Rayleigh–Taylor Instability in Inertial Confinement Fusion," to be published in Physics of Plasmas.

R. Betti, V. N. Goncharov, R. L. McCrory, and C. P. Verdon, "Linear Theory of the Ablative Rayleigh–Taylor Instability," to be published in the Proceedings of the 24th ECLIM, Madrid, Spain, 3–7 June 1996.

T. R. Boehly, R. L. McCrory, S. J. Loucks, J. M. Soures, C. P. Verdon, A. Babushkin, R. E. Bahr, R. Boni, D. K. Bradley, D. L. Brown, R. S. Craxton, J. A. Delettrez, W. R. Donaldson, R. Epstein, P. A. Jaanimagi, S. D. Jacobs, K. Kearney, R. L. Keck, J. H. Kelly, T. J. Kessler, R. L. Kremens, J. P. Knauer, S. A. Kumpan, S. A. Letzring, D. J. Lonobile, L. D. Lund, F. J. Marshall, P. W. McKenty, D. D. Meyerhofer, S. F. B. Morse,

A. Okishev, S. Papernov, G. Pien, W. Seka, R. Short, M. J. Shoup, III, M. Skeldon, S. Skupsky, A. W. Schmid, D. J. Smith, S. Swales, M. Wittman, and B. Yaakobi, "The First Year of ICF Experiments on OMEGA—a 60-Beam, 60-TW Laser System," to be published in the Proceedings of the 16th IAEA Fusion Energy Conference, Montreal, Canada, 7–11 October 1996.

T. R. Boehly, R. L. McCrory, C. P. Verdon, W. Seka, S. J. Loucks, A. Babushkin, R. E. Bahr, R. Boni, D. K. Bradley, R. S. Craxton, J. A. Delettrez, W. R. Donaldson, R. Epstein, D. Harding, P. A. Jaanimagi, S. D. Jacobs, K. Kearney, R. L. Keck, J. H. Kelly, T. J. Kessler, R. L. Kremens, J. P. Knauer, D. J. Lonobile, L. D. Lund, F. J. Marshall, P. W. McKenty, D. D. Meyerhofer, S. F. B. Morse, A. Okishev, S. Papernov, G. Pien, T. Safford, J. D. Schnittman, R. Short, M. J. Shoup III, M. Skeldon, S. Skupsky, A. W. Schmid, V. A. Smalyuk, D. J. Smith, J. M. Soures, M. Wittman, and B. Yaakobi, "Inertial Confinement Fusion Experiments with OMEGA—a 30-kJ, 60-Beam UV Laser," to be published in the Proceedings of the 1997 IAEA Conference, Osaka, Japan, 10–14 March 1997.

T. R. Boehly, V. A. Smalyuk, D. D. Meyerhofer, J. P. Knauer, D. K. Bradley, C. P. Verdon, and D. Kalantar, "The Effect of Increased Irradiation Uniformity on Imprinting by 351-nm Laser Light," to be published in the Proceedings of the Thirteenth International Conference on Laser Interactions and Related Plasma Phenomena (LIRPP), Monterey, CA, 13–18 April 1997.

D. K. Bradley and P. M. Bell, "Implementation of 30-ps Temporal Resolution Imaging on the OMEGA Laser System," to be published in the Proceedings of the 22nd International Congress on High-Speed Photography and Photonics, Santa Fe, NM, 27 October–1 November 1996.

B. Buerke, J. P. Knauer, S. J. McNaught, and D. D. Meyerhofer, "Precision Tests of Laser-Tunneling Ionization Models," to be published in the Applications of High Field and Short Wavelength Sources VII, 1997 OSA Technical Digest Series.

J. L. Chaloupka, T. J. Kessler, and D. D. Meyerhofer, "A Three-Dimensional Ponderomotive Trap for High-Energy Electrons," to be published in the Applications of High Field and Short Wavelength Sources VII, 1997 OSA Technical Digest Series.

A. V. Chirokikh, W. Seka, A. Simon, and R. S. Craxton, "Brillouin Scattering in Long-Scale-Length Laser Plasmas," to be published in Physics of Plasmas.

T. J. B. Collins, H. L. Helfer, and H. M. Van Horn, "Accretion Disk and Boundary Layer Models Incorporating OPAL Opacities," to be published in Astrophysical Journal.

S. Cremer, C. P. Verdon, and R. D. Petrasso, "Tertiary Proton Diagnostics in Future ICF Experiments," to be published in Physics of Plasmas.

M. Currie, C.-C. Wang, R. Sobolewski, and T. Y. Hsiang, "Picosecond Nodal Testing of Centimeter-Size Superconducting Microstrip Interconnects," to be published in Applied Superconductivity.

F. Dahmani, J. C. Lambropoulos, A. W. Schmid, S. Papernov, and S. J. Burns, "Fracture of Fused Silica with 351-nm-Laser-Generated Surface Cracks," to be published in the Journal of Applied Physics.

B. DeMarco, C. W. Barnes, K. Kearney, and R. L. Kremens, "Neutron Yield Measurement on the OMEGA Laser System," to be published in the Review of Scientific Instruments.

P. M. Fauchet, "Porous Silicon: Photoluminescence and Electroluminescent Devices," to be published in the Light Emission in Silicon, Semiconductors, and Semimetals Series.

D. Fried, R. E. Glena, J. D. B. Featherstone, and W. Seka, "Permanent and Transient Changes in the Reflectance of CO_2 Laser-Irradiated Dental Hard Tissues at $\lambda = 9.3$, 9.6, 10.3, and 10.6 μm and at Fluences between $1-20$ J/cm^2," to be published in Lasers in Surgery and Medicine.

R. E. Giacone, C. J. McKinstrie, and R. Betti, "Response to Comment on 'Angular Dependence of Stimulated Brillouin Scattering in Homogeneous Plasma' [Phys. Plasmas **2**, 4596 (1995]," to be published in Physics of Plasmas.

B. E. Gillman and S. D. Jacobs, "Bound Abrasive Polishers for Optical Glass," to be published in the Journal of Applied Optics.

W. Göb, W. Lang, and R. Sobolewski, "Magnetoresistance of a YBa$_2$Cu$_3$O$_7$ Corbino Disk: Probing Geometrical Contributions to the Unconventional Normal-State Magne-

toresistance of High-Temperature Superconductors," to be published in Physical Review B: Rapid Communications.

K. Green, M. Lindgren, C.-C. Wang, L. Fuller, T. Y. Hsiang, W. Seka, and R. Sobolewski, "Picosecond Photoresponse in Polycrystalline Silicon," to be published in the Proceedings of Ultrafast Electronics and Optoelectronics, Incline Village, NV, 17–21 March 1997.

M. J. Guardalben, "Conoscopic Alignment Methods for Birefringent Optical Elements in Fusion Lasers," to be published in Optics & Photonics News.

O. E. Hanuch, V. B. Agrawal, S. Papernov, M. delCerro, and J. V. Aquavella, "Posterior Capsular Polishing with the Nd:YLF Picosecond Laser: Model Eye Study," to be published in Investigative Ophthalmology.

S. D. Jacobs, W. I. Kordonski, and H. M. Pollicove, "Precision Control of Aqueous Magnetorheological Fluids for Finishing of Optics" to be published in the Proceedings of ERMR 1997, 6th International Conference on Electrorheological Fluids, Magnetorheological Suspensions, and Their Applications, Yonezawa, Japan, 22–25 July 1997.

D. Jacobs-Perkins, M. Currie, K. T. Tang, C.-C. Wang, C. Williams, W. R. Donaldson, R. Sobolewski, and T. Y. Hsiang, "Subpicosecond Electro-Optic Imaging Using Interferometric and Polarization-Based Apparatus," to be published in the Proceedings of Ultrafast Electronics and Optoelectronics, Incline Village, NV, 17–21 March 1997.

R. L. Keck, A. V. Okishev, M. D. Skeldon, A. Babushkin, and W. Seka, "Pulse Shaping on the OMEGA Laser System," to be published in the Proceedings of the Thirteenth International Conference on Laser Interactions and Related Plasma Phenomena (LIRPP), Monterey, CA, 13-18 April 1997.

T. J. Kessler, Y. Lin, L. S. Iwan, W. P. Castle, C. Kellogg, J. Barone, E. Kowaluk, A. W. Schmid, K. L. Marshall, D. J. Smith, A. L. Rigatti, J. Warner, and A. R. Staley, "Laser Phase Conversion Using Continuous Distributed Phase Plates," to be published in the Proceedings of the Second Annual International Conference on Solid-State Lasers for Application to Inertial Confinement Fusion (ICF), Paris, France, 22–25 October 1996.

J. P. Knauer, D. D. Meyerhofer, T. R. Boehly, D. Ofer, C. P. Verdon, D. K. Bradley, P. W. McKenty, V. A. Smalyuk, S. G. Glendinning, and R. G. Watt, "Single-Mode Rayleigh–Taylor Growth-Rate Measurements with the OMEGA Laser System," to be published in the Proceedings of the Thirteenth International Conference on Laser Interactions and Related Plasma Phenomena (LIRPP), Monterey, CA, 13–18 April 1997.

J. P. Knauer, C. P. Verdon, R. Betti, D. D. Meyerhofer, T. R. Boehly, D. K. Bradley, V. A. Smalyuk, P. W. McKenty, S. G. Glendinning, D. H. Kalantar, R. G. Watt, P. L. Gobby, O. Willi, and R. J. Taylor, "Single-Mode Rayleigh–Taylor Growth-Rate Measurements with the OMEGA Laser System," to be published in Physical Review E.

E. M. Korenic, S. D. Jacobs, S. M. Faris, and L. Li, "Cholesteric Liquid Crystal Flakes—a New Form of Domain," to be published in Molecular Crystals and Liquid Crystals.

E. M. Korenic, S. D. Jacobs, S. M. Faris, and L. Li, "Cholesteric Liquid Crystal Transmission Profile Asymmetry," to be published in Molecular Crystals and Liquid Crystals.

E. M. Korenic, S. D. Jacobs, S. M. Faris, and L. Li, "Color Gamut of Cholesteric Liquid Crystal Films and Flakes by Standard Colorimetry," to be published in COLOR Research and Application.

K. S. Lebedev, E. A. Magulariya, S. G. Lukishova, S. V. Belyaev, N. V. Malimonenko, and A. W. Schmid, "Reflective Nonlinearities of Nonabsorbing Chiral Liquid Crystals: Frustration of Selective Reflection by Powerful Laser Radiation," to be published in the Bulletin of the American Physical Society.

M. Lindgren, M. Currie, C. Williams, T. Y. Hsiang, P. M. Fauchet, S. H. Moffat, R. A. Hughes, J. S. Preston, and F. A. Hegmann, "Ultrafast Photoresponse and Pulse Propagation in High-T_c Superconducting Y-Ba-Cu-O Thin Film Devices," to be published in the IEEE Journal on Selected Topics in Quantum Electronics.

M. Lindgren, M. Currie, C. Williams, T. Y. Hsiang, P. M. Fauchet, R. Sobolewski, S. H. Moffat, R. A. Hughes, J. S. Preston, and F. A. Hegmann, "Intrinsic Photoresponse of a Y-Ba-Cu-O Superconductor," to be published in Physical Review B.

M. Lindgren, W.-S. Zeng, M. Currie, C. Williams, T. Y. Hsiang, P. M. Fauchet, R. Sobolewski, S. H. Moffat, R. A. Hughes, J. S. Preston, and F. A. Hegmann, "An Ultrafast High-T_c Superconducting Y-Ba-Cu-O Photodetector," to be published in the Proceedings of Ultrafast Electronics and Optoelectronics, Incline Village, NV, 17–21 March 1997.

M. Lindgren, W.-S. Zeng, M. Currie, R. Sobolewski, S. Cherednichenko, B. Voronov, and G. N. Gol'tsman, "Picosecond Response of a Superconducting Hot-Electron NbN Photodetector," to be published in Applied Superconductivity.

S. G. Lukishova, S. V. Belyaev, K. S. Lebedev, E. A. Magulariya, A. W. Schmid, and N. V. Malimonenko, "cw and High-Repetition-Rate Lasing in Nd:YAG Resonators with Chiral-Nematic Liquid-Crystal Mirrors: A Study of Nonlinear Responses," to be published in Quantum Electronics.

S. G. Lukishova, S. V. Belyaev, K. S. Lebedev, E. A. Magulariya, A. W. Schmid, and N. V. Malimonenko, "Nonlinear Bleaching in the Selective Reflection of Nonabsorbing Chiral-Nematic Liquid-Crystal Thin Films," to be published in JETP Letters and in Molecular Crystals and Liquid Crystals.

F. J. Marshall, M. M. Allen, J. P. Knauer, J. A. Oertel, and T. Archuleta, "A High-Resolution X-Ray Microscope for Laser-Driven Planar-Foil Experiments," to be published in Physics of Plasmas.

K. L. Marshall, J. Haddock, N. Bickel, D. Singel, and S. D. Jacobs, "Angular-Scattering Characteristics of Ferroelectric Liquid Crystal Electro-Optical Devices Operating in the TSM and ESM Modes," to be published in the Journal of Applied Optics.

S. M. McCormack, D. Fried, J. D. B. Featherstone, R. E. Glena, and W. Seka, "Scanning Electron Microscope Observations of CO_2 Laser Effects on Dental Enamel," to be published in the Journal of Dental Research.

R. L. McCrory, "The LLE Direct-Drive Target Physics Experimental Program: First Year of ICF Experiments on OMEGA," to be published in the Proceedings of the 24th ECLIM, Madrid, Spain, 3–7 June 1996 (invited).

C. J. McKinstrie, A. V. Kanaev, V. T. Tikhonchuk, R. E. Giacone, and H. X Vu, "Three-Dimensional Analysis of the Power Transfer Between Crossed Laser Beams," to be published in Physics of Plasmas.

C. J. McKinstrie and E. J. Turano, "Non-relativistic Motions of a Charged Particle in an Electromagnetic Field," to be published in the Journal of Plasma Physics.

J. J. Ou and S.-H. Chen, "Molecular Dynamics Simulation of Organic Glass-Formers. I. *ortho-* Terphenyl and 1.3.5-Tri-α-Naphthyl Benzene," to be published in the Journal of Computational Chemistry.

S. Papernov, A. W. Schmid, and D. Zaksas, "Characterization of Freestanding Polymer Films for Application in 351-nm, High-Peak-Power Laser Systems," to be published in Optical Engineering.

S. Papernov, A. W. Schmid, and F. Dahmani, "Laser Damage in Polymer Waveguides Driven Purely by a Nonlinear, Transverse-Scattering Process," to be published in Optics Letters.

S. Papernov, A. W. Schmid, J. F. Anzellotti, D. J. Smith, D. R. Collier, and F. A. Carbone, "One Step Closer to the Intrinsic Laser Damage Threshold of HfO_2 and SiO_2 Monolayer Thin Films," to be published in the Proceedings of the 30th Annual Boulder Damage Symposium, Boulder, CO, 6–8 October 1997.

R. D. Petrasso, C. K. Li, M. D. Cable, S. M. Pollaine, S. W. Haan, T. P. Bernat, J. D. Kilkenny, S. Cremer, J. P. Knauer, C. P. Verdon, and R. L. Kremens, "Implosion Symmetry and ρR Measurements of the National Ignition Facility from Nascent 31-MeV Tertiary Protons," to be published in Physical Review Letters.

A. L. Rigatti and D. J. Smith, "Status of Optics on the OMEGA Laser System after 18 Months of Operation," to be published in the Proceedings of the XXVIII Annual Symposium on Optical Materials for High Power Lasers, Boulder, CO, 7–9 October 1996.

J. Z. Roach, A. Ninkov, S. W. Swales, and T. Morris, "Design and Evaluation of a Screen CCD Imaging System," to be published in Optical Engineering.

W. Seka, A. Babushkin, T. R. Boehly, D. K. Bradley, M. D. Cable, R. S. Craxton, J. A. Delettrez, W. R. Donaldson, D. R. Harding, P. A. Jaanimagi, R. L. Keck, J. H. Kelly, T. J. Kessler, J. P. Knauer, R. L. Kremens, F. J. Marshall, R. L. McCrory, P. W. McKenty, D. D. Meyerhofer, S. F. B. Morse, A. V. Okishev, G. Pien, M. D. Skeldon, J. M. Soures, C. P.

Verdon, B. Yaakobi, and J. D. Zuegel, "OMEGA Experimental Program and Recent Results," to be published in the Proceedings of the Thirteenth International Conference on Laser Interactions and Related Plasma Phenomena (LIRPP), Monterey, CA, 13–18 April 1997.

H. Shi, B. M. Conger, D. Katsis, and S.-H. Chen, "Circularly Polarized Fluorescence from Chiral Nematic Liquid Crystalline Films: Theory and Experiment," to be published in Liquid Crystals.

A. Simon, "Comparison Between SBS Theories and Experiment," to be published in the Proceedings of the LaJolla Summer School '95, Plasma Physics and Technology (AIP).

M. D. Skeldon, A. Babushkin, J. D. Zuegel, R. L. Keck, A. Okishev, and W. Seka, "Modeling of an Actively Stabilized Regenerative Amplifier for OMEGA Pulse-Shaping Applications," to be published in the Proceedings of the Second Annual International Conference on Solid-State Lasers for Application to ICF, Paris, France, 22–25 October 1996.

M. D. Skeldon, A. Babushkin, W. Bittle, A. V. Okishev, and W. Seka, "Modeling the Temporal-Pulse-Shape Dynamics of an Actively Stabilized Regenerative Amplifier for OMEGA Pulse-Shaping Applications," to be published in IEEE Journal of Quantum Electronics.

M. D. Skeldon, R. Saager, and W. Seka, "Quantitative Pump-Induced Wavefront Distortions in Laser-Diode- and Flash-Lamp-Pumped Nd:YLF Laser Rods," to be published in IEEE Journal of Quantum Electronics.

D. J. Smith, J. F. Anzellotti, S. Papernov, and Z. R. Chrzan, "High Laser-Induced-Damage Threshold Polarizer Coatings for 1054 nm," to be published in the Proceedings of the XXVIII Annual Symposium on Optical Materials for High Power Lasers, Boulder, CO, 7–9 October 1996.

C. Stockinger, W. Markowitsch, W. Lang, W. Kula, and R. Sobolewski, "Mechanisms of Photodoping in Oxygen-Deficient $YBa_2Cu_3O_x$ Films Studied by *In-Situ* Transport," to be published in Physical Review B.

B. Yaakobi and F. J. Marshall, "Imaging the Cold, Compressed Shell in Laser Implosions Using the $K\alpha$ Fluorescence of a Titanium Dopant," to be published in Physical Review E.

F. Yang, D. Golini, D. H. Raguin, and S. D. Jacobs, "Planarization of Gratings Using Magnetorheological Finishing," to be published in the Proceedings: Session P–Semiconductor Surface Preparation, MRS Spring Meeting, San Francisco, CA, 2 April 1997.

M. Yu, C. J. McKinstrie, and G. P. Agrawal, "Temporal Modulational Instabilities of Counterpropagating Light Waves in a Finite Dispersive Kerr Medium, Part I: Theoretical Model and Analysis," to be published in the Journal of the Optical Society of America B.

M. Yu, C. J. McKinstrie, and G. P. Agrawal, "Temporal Modulational Instabilities of Counterpropagating Light Waves in a Finite Dispersive Kerr Medium, Part II: Application to Fabry-Perot Cavities," to be published in the Journal of the Optical Society of America B.

J. D. Zuegel and W. Seka, "Direct Measurements of Lower-Level Lifetime in Nd:YLF," to be published in the Bulletin of the American Physical Society.

J. D. Zuegel and W. Seka, "Upconversion and Reduced $^4F_{3/2}$ Upper-State Lifetime in Intensely Pumped Nd:YLF," to be published in Optics Letters.

Conference Presentations

The following presentations were made at the XXIX Annual Symposium on Optical Materials for High Power Lasers, Boulder, CO, 6–8 October 1997:

S. Papernov, D. Zaksas, and A. W. Schmid, "A Nonlinear UV-Damage Mechanism in Polymer Thin Films Observed from Below to Above Damage Threshold."

S. Papernov, D. Zaksas, and A. W. Schmid, "Perfluorinated Polymer Films with Extraordinary UV-Laser-Damage Resistance."

S.-H. Chen, J. C. Mastrangelo, B. M. Conger, and D. Katsis, "Design, Synthesis, and Potential Application of Glass-Forming Functional Organic Materials," 6th International Polymer Conference, Kusatsu, Japan, 20–24 October 1997 (invited).

The following presentations were made at the 39th Annual Meeting, APS Division of Plasma Physics, Pittsburgh, PA, 17–21 November 1997:

R. Betti and E. Fedutenko, "Beta Limits in Rotating-Toroidal Plasmas."

T. R. Boehly, V. A. Smalyuk, D. D. Meyerhofer, J. P. Knauer, D. K. Bradley, C. P. Verdon, and D. Kalanter, "The Reduction of Laser Imprinting Produced by Distributed Polarization Rotators—A New Beam-Smoothing Technique."

D. K. Bradley, "Measurements of Fuel–Pusher Mixing in Spherical Imploding Targets on the OMEGA Laser System" (invited).

J. J. Carroll III, R. P. Drake, T. B. Smith, N. A. Maslov, W. Seka, D. D. Meyerhofer, and R. S. Craxton, "Optical Spectroscopy System for Use on OMEGA Long-Scale-Length Plasma Experiments."

A. V. Chirokikh, R. S. Craxton, D. D. Meyerhofer, A. Simon, W. Seka, and R. P. Drake, "Stimulated Brillouin Scattering in Plasmas with Long-Density-Scale Lengths on OMEGA."

R. S. Craxton, D. K. Bradley, A. V. Chirokikh, D. D. Meyerhofer, W. Seka, B. Yaakobi, and R. P. Drake, "Design of Long-Scale-Length Plasma Experiments on OMEGA."

J. A. Delettrez, D. K. Bradley, R. Epstein, and C. P. Verdon, "Two-Dimensional Modeling of Imprint and Feedthrough in OMEGA Mix Spherical Experiments."

R. Epstein, J. A. Delettrez, D. K. Bradley, and C. P. Verdon, "Simulations in One Dimension of Unstable Mix in Laser-Driven Implosion Experiments."

E. Fedutenko and R. Betti, "Second Stability Region for Low-*n* External Kinks."

V. N. Goncharov, R. Betti, R. L. McCrory, and C. P. Verdon, "Linear Evolution of the Outer and Inner Surfaces of Imploding Spherical Shells."

A. V. Kanaev, C. J. McKinstrie, V. T. Tikhonchuk, R. E. Giacone, and H. X. Vu, "Three-Dimensional Analysis of the Power Transfer Between Crossed Laser Beams."

J. P. Knauer, C. P. Verdon, R. Betti, D. D. Meyerhofer, T. R. Boehly, D. K. Bradley, and V. A. Smalyuk, "Comparison of Experimentally Measured Rayleigh–Taylor Growth to Hydrodynamic Simulations."

V. Lobatchev, R. Betti, V. N. Goncharov, R. L. McCrory, and C. P. Verdon, "Dynamic Stabilization of Imploding Cryogenic Capsules."

F. J. Marshall, D. K. Bradley, J. A. Delettrez, P. A. Jaanimagi, R. L. Kremens, C. P. Verdon, B. Yaakobi, and M. D. Cable, "Further Surrogate Cryogenic Target Experiments on OMEGA."

P. W. McKenty, R. L. Keck, R. L. Kremens, K. J. Kearney, C. P. Verdon, J. D. Zuegel, M. D. Cable, T. J. Ognibene, R. A. Lerche, and R. L. Griffith, "Initial Neutron Burn Truncation Experiments on OMEGA."

D. D. Meyerhofer, D. K. Bradley, A. V. Chirokikh, R. S. Craxton, W. Seka, R. P. J. Town, B. Yaakobi, and R. P. Drake, "Characterization of Long-Scale-Length Plasmas Created Using the OMEGA Laser System."

T. J. Murphy, J. Wallace, K. A. Klare, J. A. Oertel, C. W. Barnes, N. D. Delamater, P. Gobby, A. A. Hauer, E. Lindman, G. Magelssen, O. L. Landen, S. Pollaine, P. Amendt, C. Decker, L. Suter, B. Hammel, R. Turner, R. Wallace, R. S. Craxton, F. J. Marshall, D. Bradley, D. Harding, K. Kearney, R. Keck, J. Knauer, R. Kremens, W. Seka, M. Cable, and J. Schnittman, "Experiments Utilizing Spherical Hohlraums with Tetrahedral Illumination on OMEGA."

W. Seka, D. D. Meyerhofer, A. V. Chirokikh, D. K. Bradley, R. S. Craxton, and A. Simon, "Laser–Plasma-Interaction Physics on OMEGA Implosion Experiments."

R. W. Short and A. Simon, "Collisionless Damping of Localized Plasma Waves and Stimulated Raman Scattering in Laser-Produced Plasmas."

A. Simon and R. W. Short, "Transit-Time Damping, Landau Damping, and Perturbed Orbits."

V. A. Smalyuk, T. R. Boehly, D. D. Meyerhofer, J. P. Knauer, D. Bradley, W. Seka, and C. P. Verdon, "Studies of the 3-D Evolution of Imprinting in Planar Targets Accelerated by UV Light."

R. P. J. Town, R. W. Short, C. P. Verdon, B. B. Afeyan, S. H. Glenzer, and L. J. Suter, "The Role of Nonlocal Heat Flow in Hohlraums."

E. J. Turano, C. J. McKinstrie, and A. V. Kanaev, "Oblique Stimulated Raman Scattering of a Short Laser Pulse in a Plasma Channel."

J. M. Wallace, K. A. Klare, T. J. Murphy, N. D. Delamater, E. L. Lindman, G. R. Magelssen, A. A. Hauer, S. M. Pollaine, R. E. Turner, R. S. Craxton, and J. D. Schnittman, "Analysis of Indirect-Drive, Tetrahedral-Hohlraum Experiments at OMEGA."

J. D. Zuegel, R. L. Kremens, K. J. Kearney, P. W. McKenty, C. P. Verdon, and M. D. Cable, "Wide-Dynamic-Range, Neutron Bang Time Detector on OMEGA."

S. D. Jacobs, H. M. Pollicove, W. I. Kordonski, and D. Golini, "Magnetorheological Finishing (MRF) in Deterministic Optics Manufacturing," ICPE '97, Taipei, Taiwan, 20–22 November 1997.

D. Katsis, S.-H. Chen, H. Shi, and A. W. Schmid, "Circular Dichroism Induced in Chiral-Nematic Films," Materials Research Society 1997 Fall Meeting, Boston, MA, 1–5 December 1997.